Planar Terahertz Metamaterial Based Efficient Polarization Devices and Sensors

by

Rakesh Sarkar

A thesis submitted
in Partial Fulfillment of the Requirements
for the Degree of
DOCTOR OF PHILOSOPHY.

Department of Physics
Indian Institute of Technology Guwahati
Guwahati 781039, India.

March 2022

Planar Terahertz Metamaterial Based Efficient Polarization Devices and Sensors

by

Rakesh Sarkar
Roll No. 166121103

A thesis submitted
in Partial Fulfillment of the Requirements
for the Degree of

DOCTOR OF PHILOSOPHY.

Supervisor
Dr. Gagan Kumar

Department of Physics
Indian Institute of Technology Guwahati
Guwahati 781039, India.

March 2022

Declaration

The work in this thesis entitled “*Planar Terahertz Metamterial Based Efficient Polarization Devices and Sensors*” has been carried out by me under the supervision of Dr. Gagan Kumar, Department of Physics, Indian Institute of Technology Guwahati. No part of this thesis has been submitted elsewhere for award of any other degree or qualification. The research works have been carried out in the period from January, 2016 to December, 2021.

In keeping with general practice of reporting scientific observations, due acknowledgments have been made wherever the work described is based on the findings of other investigations.

Rakesh Sarkar
Rakesh Sarkar,
Roll no. 166121103,
Department of Physics, IIT Guwahati,
Guwahati-781039, Assam, India.
DATE: 01/06/2022

CERTIFICATE

It is certified that the work contained in the thesis entitled "*Planar Terahertz Metamaterial Based Efficient Polarization Devices and Sensors* " by Mr. Rakesh Sarkar, a student of the Department of Physics, IIT Guwahati was carried out under my supervision and has not been submitted elsewhere for award of any degree.

Dr. Gagan Kumar,
Department of Physics, IIT Guwahati,
Guwahati-781039, Assam, India.
DATE: ......1/6/2022......

Dedicated to my beloved parents

Late Rohitosh Sarkar

and

Late Lipika Sarkar

ACKNOWLEDGMENTS

First and foremost, I would like to express my sincere gratitude towards my PhD advisor, Dr. Gagan Kumar for plenty of guidance on research topics, consistent support, patience and for giving me the freedom to explore my ideas. His enthusiasm and approach to research and life have always pushed me to look at every challenge as a chance to learn and progress as a researcher. I would like to thank him from the bottom of my heart for his unwavering support during my father's cancer treatment period.

My sincere gratitude also goes to my collaborator Prof. S S Prabhu, Dipa Ghindani and Ajinkya Punjal for their help on some measurements and preparation of some samples. My sincere gratitude also goes to my another collaborator Prof. Amir Ahmad for his help and support in some projects.

I would like to express my gratitude towards my doctoral committee members Dr. Uday Narayan Maiti, Dr. Kanhaiya Pandey and Prof. Amarendra Kumar Sarma for their encouragement and insightful comments which helped me to improve my presentation skills and also my understanding of my work.

My sincere gratitude goes to the current and former Heads of the Department of Physics, Prof. A. Perumal, Prof. P. Poulose and Prof. Subhradip Ghosh for providing me with all the facilities for my research and also to all the faculty members of the department and the non-teaching staff.

I would like to thank my senior and current PhD group-mates Dr. Monika, Dr. Jagan, Dr. Maidual, Dhriti, Angana, Bhairav, Bhagwat, Anshul and Chandan for all the fruitful discussions we have had. Special thanks to Bhairav and Bhagwat for assisting me a lot during the experimental setup in our lab. They were always helpful to me whenever needed. I would like to thank Kankiska, Prerona, Amir, Abdul and Rajan for helping me a lot to learn the fabrication procedure.

I would also like to thank my PhD batchmates Rajesh, Dipti, Sayan and Manvendra for all the moments of enjoyment, fun and intermittent serious discussions that we have had. And special mention must be made of my friend Rajesh, for a great and memorable time during the PhD coursework months and the rest of other periods.

I would like to thank my other most special friends Surojit, Swarup, Arghya, Samit, Pronoy, Riajul, Soumen, Amit, Abhishek for spending memorable time with me during my PhD life. Having a long walk on the campus after dinner with lots of discussions and enjoyment was very special for me. I would also thank my other closest friend Suresh for spending most of the memorable time with me in the hostel. Life would not be enjoyable without these friends. I would like to thank my old friends Rajat, Viktor, Rana, Indra, Probir, Prasenjit for always being in touch with me. I would also like to thank my teachers, who have inspired me in any direct and indirect ways throughout my life, which has led me towards pursuing science as a carrier.

Last, but not least, I would like to express my heartfelt gratitude to my family for their role in my life. My parents were always a source of inspiration to me. Their unconditional love, support and faith in me are the most precious gift for me. Their blessings will always be there with me. I would like to thank my brother Rajesh and his wife Rupa for always being there for me. My love goes to my nephew Nilkamal. I would also like to express my gratitude towards my father and mother-in-laws Krishna Das Guha and Manu Guha for their love and support in my life. I would also like to thank Sadhan Kumar Basu and Dolly Basu for their love, support and blessings for me. I want to express my gratitude towards my dearest wife Ankita Guha for her support, unconditional love and immense mental support during this journey.

ABSTRACT

The advent of metamaterials has made it possible to control and manipulate light at will through strong light-matter interactions at the subwavelength scale. In the last two decades, research in this area has grown rapidly owing to its immense potential in developing next-generation devices and components. In view of the increasing demand for high-speed communication and bandwidth, the development of photonic components at terahertz frequencies is crucial. In this thesis work, we have examined metamaterial structures of various shapes and sizes in different planar configurations to demonstrate the polarization conversion, modulation, thin-film sensing, and slow light phenomenon at terahertz frequencies.

For polarization conversion, we have proposed a coupled planar metamaterial geometry comprising two identical circular split-ring resonators (SRRs). The geometry is capable of providing a gradual change in polarization of incident terahertz with respect to change in near-field coupling between the resonators. When one resonator is rotated with respect to the other, the cross-polarization signal changes from minimum to maximum for orthogonal rotation and again back to a minimum on complete rotation through 180^0 angle. Further, we have explored the possibility of ultra-wideband terahertz polarization conversion in a planar metamaterial geometry. In a carefully designed metamaterial C-shaped resonator, we have investigated the co-and cross-polarization transmission by rotating the structure with respect to the incident terahertz at different angles. The cross-polarization conversion of nearly 40% is experimentally demonstrated which is highest in the frequency range of 1.22 THz to 2.75 THz, to the best of our knowledge. Further, we have shown that the transmission window can be shifted to the higher frequency range by changing the dimensions of the resonators, which gives the possibility to design polarization conversion devices in the desired frequency window.

Metamaterial structures exhibit strong localization of electromagnetic fields and therefore, provide an excellent platform for sensing analytes with greater sensitivity.

Researchers have shown that metamaterials can exhibit electromagnetically induced transparency effect (EIT), a classical analogue of a quantum phenomenon that has potential in sensing. It has been a challenging task to develop polarization-insensitive sensors in EIT metamaterials. We have addressed this challenge in this thesis. We have shown that a planar-coupled metamaterial geometry comprising of four carefully designed C-shaped resonators placed symmetrically on both sides of a cross-wire can exhibit polarization-independent response of the dual-band EIT effect for two orthogonal polarizations of incident light. We have investigated the potential of the metamaterial configuration in thin-film sensing at terahertz.

Several applications require independent control of EIT windows for constructing frequency-selective devices and filters. In this context, we have experimentally demonstrated independent modulation of individual transparency windows through a novel planar-coupled metamaterial configuration comprising a cut-wire (CW) and a pair of double C-resonators (DCRs). By displacing one resonator with respect to the CW, while keeping the other fixed at its position the independent modulation of each transparency window is achieved. In EIT, the dispersion properties undergo a sudden change within the transparency window. This is accompanied by a sharp decline in group velocity of the incident terahertz. This property is significant to the slow light phenomenon. We have shown how steep dispersion change results in the slowing down of transmitted terahertz. This study is significant to the construction of buffers, slow light devices, modulators, etc.

LIST OF PUBLICATIONS

Journal Publications

1. S Jagan Mohan Rao, **Rakesh Sarkar**, Gagan Kumar and Dibakar Roy Chowdhury, "Gradual cross polarization conversion of transmitted waves in near field coupled planar terahertz metamaterials", OSA Continuum 2(3), 603-614, 2019.

2. **Rakesh Sarkar**, Dipa Ghindani, K Monika Devi, S S Prabhu, Amir Ahmad and Gagan Kumar, "Independently tunable electromagnetically induced transparency effect and dispersion in a multiband terahertz metamaterial", Scientific Reports 9(1), 1-10, 2019.

3. **Rakesh Sarkar**, K Monika Devi, Dipa Ghindani, S S Prabhu, Dibakar Roy Chowdhury and Gagan Kumar, "Polarization independent double-band electromagnetically induced transparency effect in terahertz metamaterials", Journal of Optics 22(3), 035105, 2020.

4. **Rakesh Sarkar**, Ajinkya Punjal, S S Prabhu and Gagan Kumar , "Ultra wideband efficient linear polarization conversion of terahertz wave in a planar metamaterial", (Accepted in Journal of Physics D: Applied Physics).

5. Maidul Islam, KM Dhriti, **Rakesh Sarkar** and Gagan Kumar , "Tunable control of electromagnetically induced transparency effect in a double slot terahertz waveguide ", Optics Communications, 2021. 483: p. 126632.

6. Angana Bhattacharya **Rakesh Sarkar** and Gagan Kumar, "Excitation of near field coupled dual toroidal resonances in a bilayer terahertz metamaterial configuration", Journal of Physics D: Applied Physics, 2021.

7. Angana Bhattacharya, **Rakesh Sarkar**, Naval K Sharma, Bhairov K Bhowmik, Amir Ahmad and Gagan Kumar, "Multiband transparency effect induced by

toroidal excitation in a strongly coupled planar terahertz metamaterial", Scientific Reports, 11(1), pp.1-9.

8. Angana Bhattacharya, **Rakesh Sarkar** and Gagan Kumar, "Toroidal electromagnetically induced transparency based meta-surfaces and its applications in terahertz sensing ", iScience 25 (1): 103708.
9. **Rakesh Sarkar**, Angana Bhattacharya, Ajinkya Punjal, S S Prabhu and Gagan Kumar, "Broadband terahertz polarization conversion using a planar toroidal metamaterial", (Under review).
10. S Jagan Mohan Rao, Ajinkya Punjal, **Rakesh Sarkar**, Dipa Ghindani, S S Prabhu and Gagan Kumar, "Broadband linear polarization conversion in a planar coupled terahertz metamaterial", (in preparation).

LIST OF PUBLICATIONS

Conference Proceedings

1. **Rakesh Sarkar**, K Monika Devi, Dipa Ghindani, Ravi K Jain, A Pattanayak, S S Prabhu and Gagan Kumar, "Dual band electromagnetically induced transparency effect in asymmetrically coupled terahertz metamaterials ", 44th International Conference on Infrared , Millimeter and Terahertz (IRMMW) 1-2,(2019).

2. K Monika Devi, **Rakesh Sarkar**, Amarendra K Sarma and Gagan Kumar, "Exploring polarization independent plasmon induced transparency in a planar terahertz metamaterial", IEEE Workshop on Recent Advances in Photonics (WRAP), 1-3,(2019).

3. **Rakesh Sarkar**, Dipa Ghindani, K Monika Devi, S Jagan Mohan Rao, SS Prabhu and Gagan Kumar,"Modulating double-band electromagnetically induced transparency effect via near field coupling in planar terahertz metamaterials", IEEE Workshop on Recent Advances in Photonics (WRAP), 1-3,(2019).

4. S Jagan Mohan Rao, **Rakesh Sarkar**, Gagan Kumar and Dibakar Roy Chowdhury,"Studying the near field capacitive coupling in planar terahertz metamaterial ", IEEE Workshop on Recent Advances in Photonics (WRAP), 1-3,(2017).

5. **Rakesh Sarkar**, Ajinkya Punjal, S S Prabhu and Gagan Kumar," Broad-band terahertz polarization conversion in a planar metasurface", IEEE Workshop on Recent Advances in Photonics (WRAP), 1-2,(2022).

6. Angana Bhattacharya, **Rakesh Sarkar**, Anshul Bharrdwaj and Gagan Kumar,"Sensing in a toroidal coupled dual-band EIT terahertz metadevice", IEEE Workshop on Recent Advances in Photonics (WRAP), 1-2,(2022).

7. Angana Bhattacharya, **Rakesh Sarkar**, Ajinkya Punjal, S S Prabhu and Gagan Kumar,"Planar terahertz toroidal meta-device for efficient polarization conversion ", (accepted in Cleo 2022).
8. S Jagan Mohan Rao, **Rakesh Sarkar**, Ajinkya Punjal, Dipa Ghindani, S S Prabhu, and Gagan Kumar,"Linear cross-polarization conversion in a planar near field coupled terahertz metamaterials", (accepted in IRMMW-THz 2022.)

CONFERENCES/SCHOOLS ATTENDED

1. Workshop on Recent Advances in Photonics (WRAP) at MEC, 20-22 December, 2017, Hyderabad, India. Topic: Studying the near field capacitive coupling in planar terahertz metamaterial (**Poster Presentation**).
2. International Conference on Fiber Optics and Photonics, Dec 12-15, 2018. IIT Delhi, India. Topic:Asymmetric splkit gap ring resonator based near field capapcitive coupling in terahertz metamaterials (**Poster Presentation**).
3. Workshop on Recent Advances in Photonics (WRAP) at IIT Guwahti,13-14 December,2019, Guwahati, India. Topic:Modulating double-band electromagnetically induced transparency effect via near field coupling in planar terahertz metamaterials (**Poster Presentation**).
4. Workshop on Recent Advances in Photonics (WRAP) at IIT Bombay,4-6 March,2022, Mumbai, India. Topic:Broad-band terahertz polarization conversion in a planar metasurface (**Poster Presentation**).

LIST OF FIGURES

Schematic of s-SRR, r-SRR and x-SRR for polariztaion control through symmetry breaking.

- **Figure 1.9:** (a) A planar metamaterial sensor composed of an array of symmetric SRRs along with the transmission spectra. (b) A MM sensor based on SRRs with asymmetric double split gaps along with the frequency shift vs refractive index plot for quadrupole and fano resonances.

- **Figure 1.10:** (a) A metamaterial-based biosensor along with the transmission under different concentrations of oral cancer cells. (b) A dual-band EIT like metamaterial sensor. The frequency shift of two EIT peaks with differing refractive indexes of an analyte is also depicted here.

- **Figure 1.11:** (a) Schematic illustration of a planar MM configuration comprised of a CW and two SRRs which exhibits an EIT like effect and active control of the group delay in the proposed structure under different excitation of the pump beam. (b) Planar MM geometry is comprised of a CW and two different SRRs which exhibits dual-band EIT effect and slow light phenomenon in the terahertz frequency range.

- **Figure 2.1:** Initial template of CST Microwave Studio.

- **Figure 2.2:** (a) Boundary conditions used to simulate metamaterial geometry using CST Microwave Studio. (b) Transmission along with the schematic of the MM geometry. In the schematic diagram, gold resonators are shown by the yellow color and the quartz substrate is depicted by the grey color. The green arrow depicts the direction of the electric field of incident terahertz.

- **Figure 2.3:** Procedure of fabrication of terahertz metamaterial samples in step by step using electron beam lithography.

- **Figure 2.4:** Schematic of the THz Time-domain setup. BS-Beam splitter, PM-Parabolic Mirror, PCA-Photo Conductive Antenna, QW-Quarter Waveplate, WP-Wollaston Prism.

- **Figure 2.5:** Schematic of terahertz generation using a photoconductive antenna. The PCA is comprised of two metal electrodes and is fabricated on an LT-GaAs substrate.

variation of 2^{nd} transparency window with distance between CW and left DCR respectively.

- **Figure 6.5:** (a) Numerically calculated group refractive index versus frequency. (b) and (c) depicts variation of group velocity versus frequency in the normally dispersive regimes of the 1^{st} and 2^{nd} transparency windows, respectively.

- **Figure 6.6:** Simulated and theoretically fitted transmission spectra (a), (b), (c) for various distance (d_1) between the CW and right DCR for the modulation of 1^{st} transparency window and (d), (e), (f) for various distance (d_2) between CW and left DCR for the modulation of the 2^{nd} transparency window of the proposed multi-band EIT metamaterial.

- **Figure 6.7:** The variations of the fitting parameters γ_1, γ_2, γ_3, Ω_1 and Ω_2 as the function of (a) (d_1) for the modulation of 1^{st} transparency window and (b) (d_2) for the modulation of the 2^{nd} transparency window of the multi-band EIT spectrum.

TABLE OF CONTENTS

CHAPTER 1

INTRODUCTION

In the last few decades, terahertz science and technology has achieved much rapid advancement in terms of devices and components. Terahertz radiations cover a very narrow frequency range (i.e. 0.1-10 THz) [1, 2]. In the electromagnetic spectrum, THz radiation is positioned between the microwave and infrared frequency regimes. The position of terahertz radiation is depicted in Figure 1.1. The radiation has a period of 1ps, a wavelength of 300 μm, a wavenumber of $33cm^{-1}$, and a photon energy of 4.1 meV at 1 THz. Although there are various sources for THz radiations surrounding us most of the sources are incoherent and hardly be used. Due to the unavailability of efficient sources, which can emit controlled signals and detectors, this portion of the electromagnetic spectrum did not see much more advancement as compared to the microwave and electronics. THz waves are also called T-rays and exhibit properties just like other electromagnetic waves and their propagation is governed by Maxwell

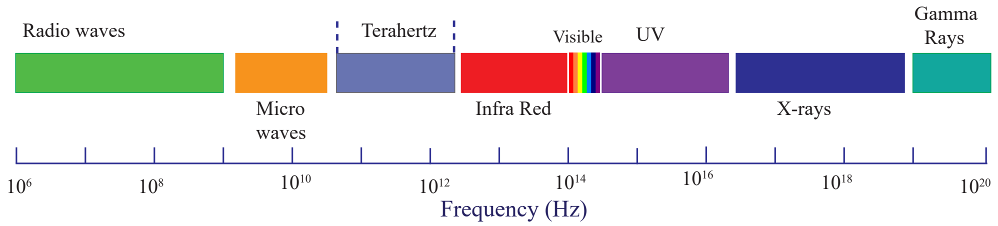

Figure 1.1: The position of Terahertz radiation along with other radiations in the electromagnetic spectrum.

equations. It is very difficult to handle THz waves as compared to the adjacent waves. Various approximations used for optical and electromagnetic waves may not be valid for THz radiations. Hence, to realize and utilize THz waves it is very crucial to explore new tools and technologies.

1.1 Applications of terahertz radiations

With the recent development of technologies, THz radiations have found applications in medicines, security, wireless communications, and in many industrial fields [3, 4]. Owing to the very low photon energies, THz waves do not cause any harm to the biological tissues [5]. Due to the strong polarity, water molecules strongly absorb THz radiations. On the other hand, metals reflect THz waves strongly. As THz waves have a longer wavelength, they are affected less by Mie scattering. Most dry dielectric materials, such as cloth, paper, wood, and plastic, may easily transmit THz vibrations. The spectral response of organic and biological molecules are unique due to their absorptions and dispersions at THz frequencies. Individual compounds' spectrum responses are determined via THz spectroscopy. The THz imaging approach can retrieve both the target's profile and composition information. THz technology can provide a valuable contribution in the field of dispersion control for polymers [6]. In addition, using THz technology it is possible to inspect plastic weld joints [7]. In the food industry, terahertz technology is widely used for quality control of food products [8]. In this case, THz technology alloys secure distinction between ingredients and unwanted inclusions. THz waves can penetrate through clothes and hence any hidden objects like weapons or explosives beneath the cloths can be detected [9]. Figure 1.2(a) shows the detection of a hidden knife and toy gun behind cloth using terahertz radiation [10]. While there are no reliable techniques for the detection of liquid explosives, THz technology can easily be applied in this field with higher accuracy. Nowadays, THz radiations are used at airports for the scanning of passengers as this radiation do not cause any health risk [11]. The THz system can be employed to investigate the plant's hydrology due to high absorption coefficients and the strong normal dispersion of water at THz frequencies. Many polar molecules absorb THz radiations and hence these molecules in the gas phase are detected by THz radiations. THz radiations are also used in the semiconductor industries to determine the carrier concentration and mobility of semiconductors. Also in the superconductor research, THz radiations are employed to determine the parameters of superconducting

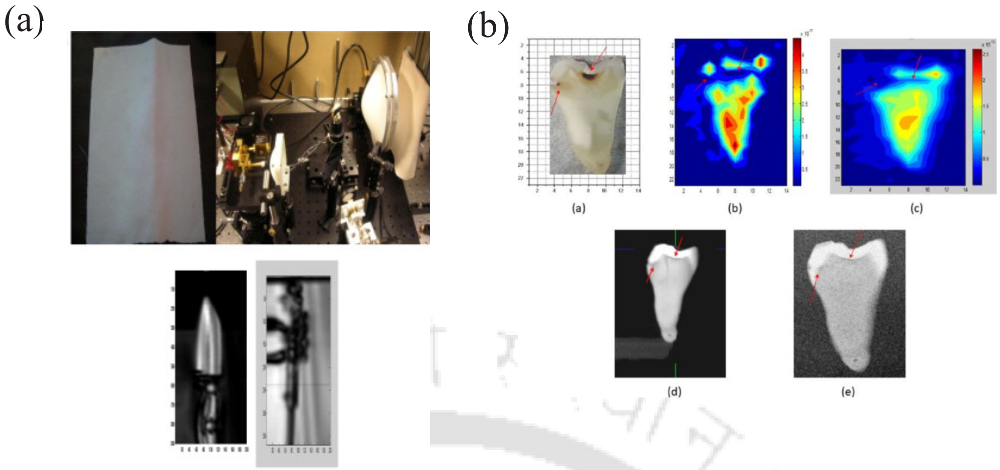

Figure 1.2: (a) Identification of knife and toy gun behind cloth using terahertz imaging technique. Reprinted from [10], © 2009, with permission from Elsevier. (b) Depicts identification of tooth caries using terahertz and other imaging techniques [13].

materials. THz radiation can also be used in the study of historical and archaeological work. This radiation is non-invasive to historical work, neither to the paintings nor to any kind of stone or metal. In the area of biomedical diagnostics, we can make use of THz tomography. THz radiations can be used to examine tissue near the surface, in particular skin and teeth. Figure 1.2(b) illustrates the medical diagnosis of the tooth caries using terahertz and other imaging techniques [13]. On the other hand, the sensitivity to water enables the investigation of tissue hydration. This opens a range of applications including detection of skin cancer and caries. Nowadays detection of skin cancer using THz radiation works very well [12]. Breast cancer detection could be an application as well, because of the lower water content of the tissue here [14]. THz waves can also be used to directly monitor the binding state of genetic materials (DNA and RNA) [15].

1.2 Metamaterials

1.2.1 Brief history of metamtaterials

“Meta” is a Greek word, which means something beyond. Metamaterials (MMs) are a new class of 3D artificial engineered structures composed of an array of metals and or/dielectric. Research in the field of MMs was initiated by the theoretical prediction of Russian theorist Victor Veselago in the year of 1968 [16]. Pendry et al. confirmed his theoretical prediction of the existence of a negative index medium in the year 1996 [17]. In their work, they proposed negative permittivity in artificially wired structures to realize artificial electric plasma followed by the realization of magnetic plasma with negative permeability with an array of split-ring resonators (SRRs) in 1999 [18]. These theoretical predictions were confirmed experimentally for the 1st time by Shelby et al. using a MM with repeated unit cells of SRR and copper wire in the microwave frequency regime [19].

Negative index MMs can be characterized by using Maxwell equations of the following form

$$\vec{\nabla} \times \vec{E} = -\mu \frac{\partial \vec{H}}{\partial t} \tag{1.1a}$$

$$\vec{\nabla} \times \vec{H} = \vec{J} + \epsilon \frac{\partial \vec{E}}{\partial t} \tag{1.1b}$$

$$\vec{\nabla} \cdot \vec{E} = \frac{\rho}{\epsilon} \tag{1.1c}$$

$$\vec{\nabla} \cdot \vec{B} = 0 \tag{1.1d}$$

For plane waves, one can solve equations (1.1a) and (1.1b) by inserting $\vec{E} = E_0 e^{(i\omega t - \vec{k}\cdot\vec{r})}$ and $\vec{H} = H_0 e^{(i\omega t - \vec{k}\cdot\vec{r})}$. This gives

$$\vec{k} \times \vec{E} = \omega\mu\vec{H}; \vec{k} \times \vec{H} = -\omega\epsilon\vec{E} \tag{1.2}$$

When ϵ and μ are positive, $\vec{E}$,$\vec{H}$ and $\vec{k}$ forms a right-handed system in which energy flows in the direction of propagation of light. On the other hand when ϵ and μ are negative equation (1.2) becomes

$$\vec{k} \times \vec{E} = -\omega\mu\vec{H}; \vec{k} \times \vec{H} = \omega\epsilon\vec{E} \tag{1.3}$$

In this case a left-handed system will be formed in which energy will flow in the opposite direction of the propagation of light.

Sir John Pendry demonstrated the first artificial material in the microwave frequency range in an array of split-ring resonators (SRRs) as shown in Figure 1.3(b). In this study, the magnetic field was excited in the perpendicular orientation to the plane of the rings. This results in the induced resonating currents in the loop and generated an equivalent magnetic dipole moment. The frequency-dependent effective permeability of the SRR

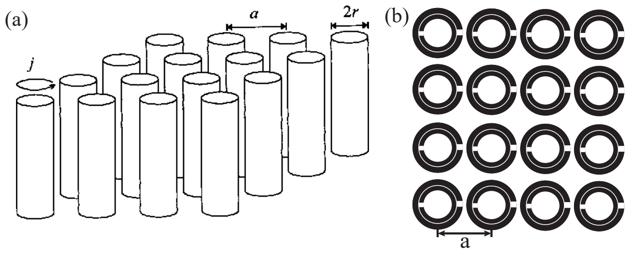

Figure 1.3: (a) Square array of metallic wires having negative permittivity and (b) planar view of magnetic double SRR which exhibits negative permeability. © 1999, IEEE. Reprinted with permission from [18].

[18] is expressed as

$$\mu_{eff}(\omega) = 1 - \frac{S\omega^2}{\omega^2 - \omega_{0m}^2 + j\omega\xi} \tag{1.4}$$

$$\omega_{0m} = c\sqrt{\frac{3a}{\pi \ln \frac{2wr^3}{d}}} \tag{1.5}$$

Here S and ξ represent the filling fraction and the damping factor respectively. The artificial magnetic dipoles excited in the rings can be larger than the applied field within a certain frequency range. This results in the negative real part of the permeability. In the lossless case ($\xi = 0$) the range around the resonant frequency providing negative permeability was found to be $\omega_{0m} < \omega < \omega_p = \frac{\omega_p}{\sqrt{1-F}}$, ω_p is the plasma frequency of the SRR particle.

Further in this work, Pendry introduced the plasmonic type negative permittivity for a metal thin wire structure which we have shown in Figure 1.3(a). The permittivity of this kind of metallic structure varies with the frequency according to the Drude's law as

$$\epsilon(\omega) = \epsilon_0 \left[1 - \frac{\omega_p^2}{\omega(\omega + i\gamma)}\right] \tag{1.6}$$

where $\omega_p^2 = \frac{Ne^2}{m\epsilon_0}$ is the plasma frequency, N =electron density, e=electron charge,m=mass of electron, γ is the rate at which the plasma oscillation's amplitude drops. When $\gamma = 0$ and $\omega < \omega_p$, the permittivity $\epsilon(\omega)$ becomes negative, as seen in this equation. The plasma frequency which depends on the density and mass of the collective electron motion is very low in that thin wire structure. Pendry's theoretical work was experimentally established by Shelby et al. in 2001 in the microwave frequency regime [19]. Their experiments directly confirmed that refractive index (n) is given by the negative square root of μ and ϵ for the frequencies where both the parameters are negative.

Various other types of metamaterials, such as chiral, plasmonic, resonant/non-resonant, and photonic MMs, have been widely explored since the discovery of negative-index metamaterials. We have investigated planar sub-wavelength MMs in this thesis work. These MMs are significantly smaller in size than the wavelength of the incoming radiation. Here, incident electromagnetic radiation is manipulated by carefully controlling structural parameters. MMs have several intriguing electromagnetic features that are uncommon in naturally occurring materials.

1.2.2 Planar metamaterials and their applications

Planar metamaterials (PMMs) are two-dimensional counterparts of metamaterials (MMs) that have subwavelength structures. Planar MMs are lightweight, small, and simple to manufacture using traditional lithography techniques. These MMs allow for plane wave modulation in both normal and oblique incidence in space. PMMs have been proposed for use in a variety of domains, including absorber, superlens, cloaking, modulators, polarization rotators, and sensors. The first experimental demonstration of the MM absorber in the microwave frequency regime was reported by Landy et al. [20]. Two metallic cut-wires and two joint SRRs with symmetric split gaps in each arm separated by a dielectric spacer made up the proposed structure. The proposed geometry is depicted schematically in Figure 1.4(a). Higher absorption rates of 99% and 88% were reported numerically and experimentally with this structure within a particular range of incidence angles.

Modulators and polarization rotators have also been designed using planar MMs. Chen et al. demonstrated an active phase modulator based on a planar MM geometry comprised of SRR on GaAs substrate [21]. Figure 1.4(b) depicts a schematic of their proposed geometry. Polarization rotators are modulators that give fixed phase shifts and allow the polarization of incident light to be changed. In various frequency regimes, polarization converters based on birefringent crystals [22], gratings, and chiral structures [23, 24] have been reported. Cloaking is another promising application of the planar MM structure. The path of light is traversed around the object to be cloaked without being impacted by the object itself in cloaking devices. In this regard, Landy et al. presented a planar microwave frequency MM cloak made up of E-shaped SRR [25]. The proposed configuration's unit cell is depicted in Figure 1.4(c).

Planar MMs can also be used to make superlenses that go beyond the diffraction limit.

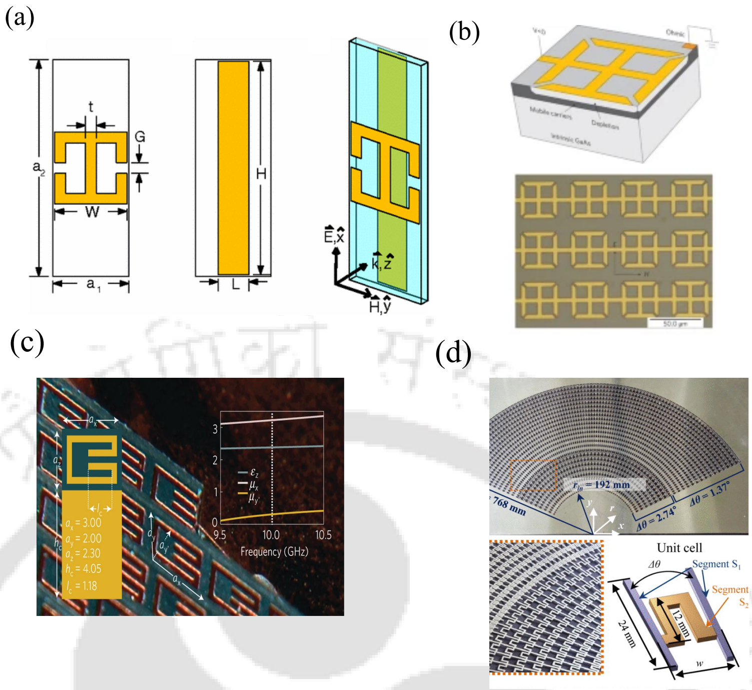

Figure 1.4: (a) 1st perfect metamaterial absorber. Reprinted (figure) with permission from [20] © 2008, the American Physical Society. (b) Active metamaterial modulator based on SRR. Reprinted by permission from Springer Nature Customer Service Centre GmbH (Springer Nature, Nature Photonics) [21] (2009). (c) Unit cell of the metamaterial cloak. Reprinted by permission from Springer Nature Customer Service Centre GmbH (Springer Nature, Nature Materials) [25] (2013). (d) Hyperbolic metasurface lens. Reprinted from [28], with permission of AIP Publishing.

Abbey diffraction limit affects traditional optical devices like lenses and microscopes [26]. This limits the resolvable feature size, which is defined as $d = \frac{\lambda}{2NA}$ where d is the resolvable feature size, NA denotes the numerical aperture and λ denotes the wavelength of the light. Both propagating and evanescent waves are involved in an object's scattered or emitted light. These evanescent waves carry the object's subwavelength information. The evanescent waves, on the other hand, decay exponentially in a material with a positive refractive index. As a result, traditional optical components are unable to capture those waves at the image plane. Pendry had previously theoretically proved that in a negative index medium (NIM) slab, evanescent waves can be enhanced rather than decaying [27]. Various perfect lenses based on negative index MM have been demonstrated experimentally based on Pendry's prediction. Figure 1.4(d) [28] illustrates a hyperbolic metasurface lens. Planar MM are also widely employed in sensing applications, such as refractive index detection and biomolecular sensing, with greatly improved sensitivities and resolutions [29, 30].

Planar MMs are used in building numerous devices in the terahertz frequency regime because naturally occurring materials don't respond to terahertz radiations. Because the constituents of Terahertz MMs are larger, they can be easily produced using traditional lithography processes. We will discuss terahertz metamaterials and their applications in various fields in the next section.

1.2.3 Terahertz Metamaterials

Over the last few decades, research interests in the THz frequency regime have grown very rapidly. It has become essential to design various devices such as polarizers, modulators, sensors, switches etc. in the THz frequency regime. In this context artificially designed structures i.e MMs are very useful. Terahertz MMs consists of sub-wavelength structures that are designed to operate in the terahertz frequency range.

1.2.4 Significance of terahertz metamaterials

THz MMs could be used in a variety of applications, from sensors to slow light systems in network communications and the development of next-generation photonic devices. By displaying several MM geometries, we have highlighted potential uses of THz MMs. The SEM image of a perfect MM absorber made up of two metallic resonators separated by two dielectric spacers is shown in Figure 1.5(a) [31]. The electrical SRR layer is on top, and the metallic ground plane is on the bottom. At 1.6 THz, the structure has an absorptivity of 0.97. In this frequency range, Cheng et al reported an ultra-broadband bandpass filter with a 0.5 THz wider bandwidth [32]. The schematic of the proposed structure is illustrated in Figure 1.5(b). A planar MM geometry comprised of a closed outer ring and an inner SRR is shown in Figure 1.5(c) [33]. The MM equivalent of the electromagnetically induced transparency effect (EIT) and the slow light phenomenon in this geometry were investigated by Chiam et al. Figure 1.5(d) illustrates wavelength multiplexing imaging by a designed meta-hologram [34]. Along with these applications, THz MMs are also used to construct active devices such as switches, modulators, polarization rotators etc. Seo et al. proposed an active MM switch in this context [35]. Gold nano-slots and a thin VO_2 sheet make up the suggested structure. The transmittance of the suggested structure was actively controlled from unity to zero by shifting the phase transition of the VO_2 layer from insulating to metallic by adjusting the temperature from 305 K to 340 K. Chen et al. also actively controlled the resonant transmission dip of a

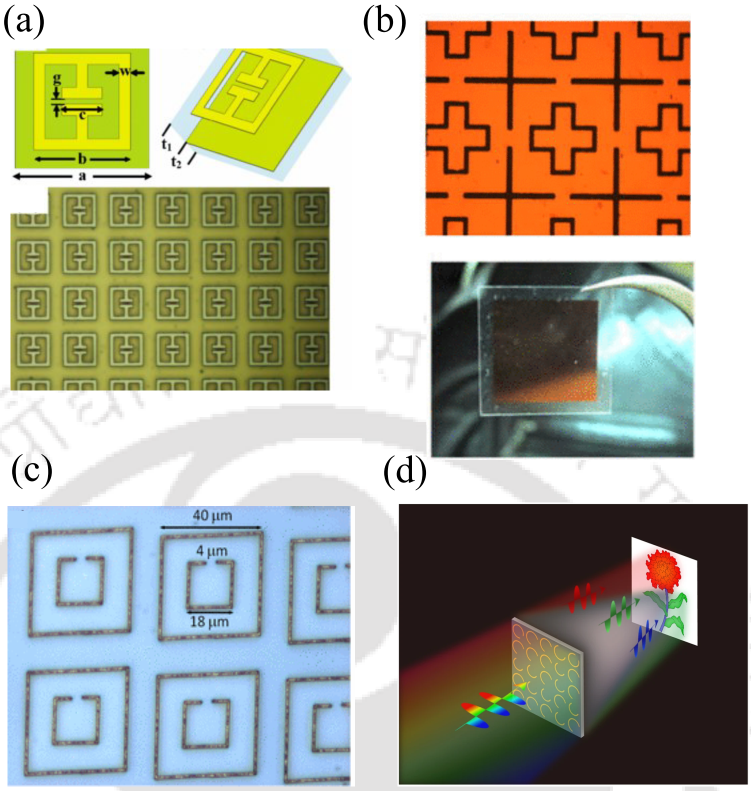

Figure 1.5: (a) Schematic of a perfect terahertz metamaterial absorber. Reprinted (figure) with permission from [31] © 2008, the American Physical Society. (b) Terahertz bandpass filter. Reprinted from [32] with permission of AIP Publishing. (c) Planar metamaterial geometry comprising of a closed ring and an SRR to exhibit electromagnetically induced transparency effect. Reprinted (figure) with permission from [33] © 2009, the American Physical Society. (d) Wavelength multiplexing imaging by a designed meta-hologram. Reproduced from [34]. CC BY 4.0 .

planar MM structure made up of an array of SRR built of a superconducting Yttrium of Barium Copper Oxide (YBCO) film [36]. By altering the temperature, the active tuning was achieved by shifting the normal state of the film to the superconducting state. Researchers have also demonstrated active THz MM devices based on graphene in this direction. EIT-like effect [37] and polarization conversion [38] have been controlled dynamically by altering the Fermi energy of the graphene monolayer with external bias voltage. Furthermore, semiconducting materials like Si or GaAs have been used to modify the frequency response of the THz MM structure. Typically, a-Si pad is put into the gap of metal resonators in these investigations, and the conductivity of Si is tuned by an infrared pump beam [39].

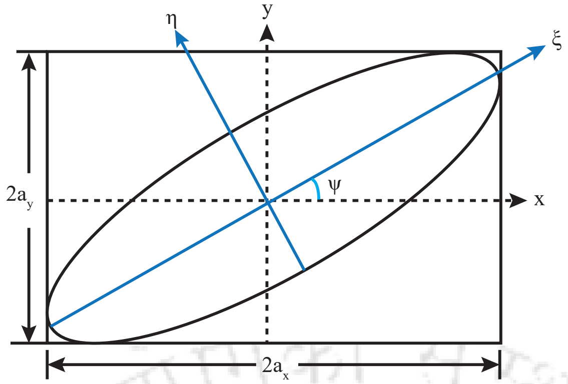

Figure 1.6: The polarization ellipse.

1.3 Polarization devices

1.3.1 Polarization state of an electromagnetic wave

The temporal variation of the electric field vector E (r,t) determines the polarization state of an electromagnetic wave at a certain location in space. The two orthogonal components of the electric field vector for a monochromatic electromagnetic wave are represented as follows:

$$E_x = a_x \cos(\omega t - kz + \delta_x) \tag{1.7}$$

$$E_y = a_y \cos(\omega t - kz + \delta_y) \tag{1.8}$$

Here a_x and a_y are amplitudes, δ_x and δ_y are the phases of the two orthogonal components and ω is the angular frequency. Equations (1.7) and (1.8) can be simplified to get,

$$\frac{E_y}{a_y} = \cos(\omega t - kz + \delta_x + \delta_y - \delta_x) \tag{1.9a}$$

$$\frac{E_y}{a_y} = \cos(\omega t - kz + \delta_x)\cos\delta - \sin(\omega t - kz + \delta_x)\sin\delta \tag{1.9b}$$

$$\frac{E_y}{a_y} = \frac{E_x}{a_x}\cos\delta \mp \sqrt{1 - \left(\frac{E_x}{A_x}\right)^2}\sin\delta \tag{1.9c}$$

$$\left[\frac{E_y}{a_y} - \frac{E_x}{a_x}\cos\delta\right]^2 = 1 - \left(\frac{E_x}{a_x}\right)^2 \sin^2\delta \tag{1.9d}$$

The trajectory of equation (1.9d) is an ellipse and is known as polarization ellipse and is shown in Figure 1.6. The polarization ellipse may be identified by its form and direction, which are defined by two angles: polarization rotation azimuth angle (ϕ) and ellipticity (η)

$$\phi = \frac{1}{2}\arctan\left(\frac{2R\cos\delta}{1-R^2}\right), \tag{1.10}$$

$$\eta = \frac{1}{2}\arcsin\left(\frac{2R\sin\delta}{1+R^2}\right), \tag{1.11}$$

where $R = \frac{a_x}{a_y}$. Depending on the magnitude ratio (R) and phase difference $\phi = \phi_y - \phi_x$, the polarization state of an electromagnetic wave is defined as follows:

1. The electromagnetic waves are said to be linearly polarized (LP) when a_x (or a_y) equals zero or the phase difference $\phi = 0$ (or $\phi = \pi$).

2. The electromagnetic waves are said to be circularly polarized when the magnitude ratio is R=1 and the phase difference is $\phi = \pm\pi/2$. $\phi = \pi/2$ corresponds to the right-handed circularly polarized (electric field spins clockwise when observed from the direction in which the wave is propagating) (RCP) and $\phi = -\pi/2$ corresponds to counterclockwise rotation and circularly polarised left-handedness (LCP).

3. The polarization state of electromagnetic waves is considered to be elliptically polarized in other circumstances.

1.3.2 Polarization manipulation by metamaterials

Manipulation of polarization of an electromagnetic wave is a challenging task however, it has several applications in various optical devices. One of the most common approaches for polarization conversion is the use of birefringence crystals in which the phenomenon of double refraction occurs. Dichroic crystals are also widely used components for polarization conversion. Optical activity is also used for the polarization rotation of an electromagnetic wave. This is the measure of chirality of the materials and it determines the amount of rotation of the plane of polarization through the optically active substances. Most of the optically active materials are in the liquid or gaseous form such as protein, sugar and liquid crystals. The Faraday effect, which uses a static magnetic field to rotate the plane of polarization of light travelling through a medium, may also be used to manipulate polarization. Hence, this effect is a magneto-optical phenomenon. However, all the phenomena discussed above are weak in naturally occurring materials and also the amount of rotation achieved is so small that it is a very challenging task to

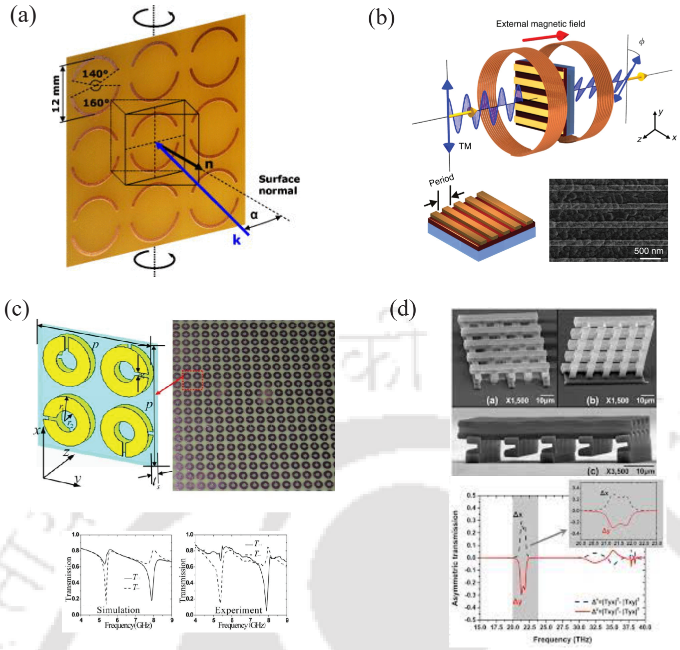

Figure 1.7: (a) Optical activity in extrinsic chiral metamolecule. Reprinted from [40] with permission of AIP Publishing. (b) Faraday rotation effect enhancement by integrating with plasmonic metamolecule. Reproduced from [41] CC BY-NC-ND 3.0. (c) Giant circular dichroism based on chiral metamaterial. [42], reproduced courtesy of The Electromagnetic Academy. (d) Three-dimensional asymmetric infrared metamaterial. Reprinted (adapted) with permission from [43]. Copyright © 2015, American Chemical Society.

measure it experimentally. In addition, these approaches require a longer propagation wavelength in a bulky volume to achieve sufficient phase retardation between the orthogonal components of an electromagnetic wave. Hence designing compact lightweight polarization control devices using these approaches is not possible. In addition, various fabrication complexities and high losses make these approaches unsuitable. Recently MM structures owing to their exceptional properties have shown great potential in this field and here we discussed various MM structures resulting in polarization conversion. The weak optical rotation observed in natural materials can be enhanced significantly with MM structures. In this context, Plum et al. demonstrated strongly enhanced optical activity in a planar MM by tilting the MM plane around its symmetry axis as shown in Figure 1.7(a) [40]. Planar MM structures are also used to enhance the polarization conversion based on the Faraday Effect. Figure 1.7(b) shows a plasmonic metamolecule integrated with magnetic materials which shows an enhanced polarization rotation using the Faraday effect [41]. Further, to enhance the circular dichroism with MM structures, Chen et al. reported double-layer SRR structures with chirality separated by a dielectric spacer in the microwave frequency regime [42]. Each layer was composed of four SRRs arranged in C4 symmetry and is shown in Figure 1.7(c). A maximum of 0.58 CD (circular dichroism) was achieved in their study. Various anisotropic MMs have also been reported for the polarization conversion of incident electromagnetic waves in reflection mode or transmission mode. These MMs act as the birefringence crystals and possess different refractive indices for the two orthogonal components of a linearly polarized wave. By controlling the phase shift of the electromagnetic wave through the careful control of their design, polarization manipulation has been achieved [43-46]. Figure 1.7(d) shows a schematic of a three-dimensional infrared asymmetric metamaterial. To convert a linearly polarized wave into the circularly polarized light or a left circular light to a right circular one or vice versa, chiral MM structures have been studied [47-51]. These structures possess different refractive indices for right and left-handed circular polarization in the two orthogonal directions. However, these structures have complex structures usually implemented in a multilayer form, which limits their applications. Polarization conversion of the linear and circularly polarized wave is also reported by the asymmetric transmission (AT) effect. In this effect when a linear or circularly polarized wave is sent from the front and back surfaces of the MM structure, different transmissions and phase retardations are achieved [52-54]. The AT effect of a linearly polarized wave is studied by introducing symmetry breaking in the unit cell of 3D or multilayer structures along the direction of propagation of light [55]. Further polarization conversion of the circularly polarized wave is reported in planar bilayer MM structures with extrinsic chirality [56, 57].

1.3.3 Status of polarization devices at terahertz frequencies

The control and manipulation of polarization have drawn a lot of research interest in many frequency regimes especially in the field of THz. MM structures based on split-ring resonators have been reported to provide polarization conversion in this frequency regime [58, 59]. However, in these structures polarization conversion occurs in a narrow frequency band. Grady et al. reported a broadband reflective cross polarization converter in a multilayer MM geometry composed of gold cut-wire array and a metallic ground plane separated by a polyimide spacer [60]. Further Cheng et al. reported another broadband reflective cross polarization converter which showed reasonably sustained bandwidth at a wide range of incident angles [61]. The microscopic image of a portion

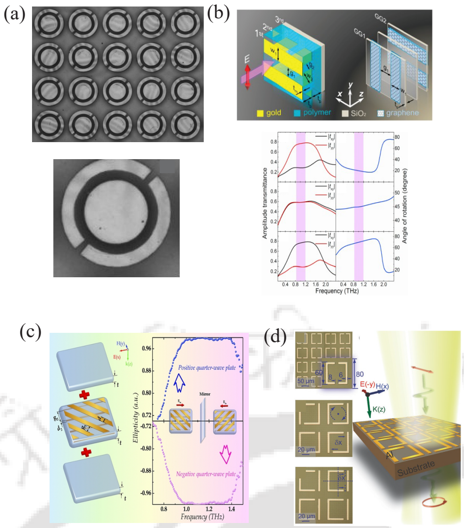

Figure 1.8: (a) Micrographic image of the unit cell of a broadband reflective polarization converter. Reprinted from [61] with permission of AIP Publishing. (b) Broadband polarization converter with tunable bandwidth based on graphene metamaterial. Reprinted from [62], © 2009, with permission from Elsevier. (c) A broadband terahertz quarter-wave plate. Adapted with permission from [64], John Wiley and Sons. (d) Schematic of s-SRR, r-SRR and x-SRR for polariztaion control through symmetry breaking. Adapted with permission from [63], John Wiley and Sons.

and unit cell of the fabricated sample is shown in Figure 1.8(a). The graphene-based metallic structure was also studied to achieve broadband cross-polarization conversion [62]. Figure 1.8(b) illustrates a multilayer graphene-based hybrid metallic structure that acts as a broadband tunable polarization rotator. Here the amplitude of co-and cross-polarization transmission is tuned by changing the bias voltages of individual graphene grating layers. Another different approach of achieving broadband polarization conversion was reported based on the lowest order rotational symmetry of a metasurface. In this context, Cong et al. investigated a metasurface as shown by Figure 1.8(d) [63]. In this study, polarization control has been achieved in a planar MM structure comprised of dual SRR by changing the split gap position. The structure shows a maximum of 47% polarization conversion. In another study, Cong et al. demonstrated a broadband quarter-wave plate based on a multilayer structure that converts a linearly polarized wave into the circular one [64]. Their proposed geometry is depicted in Figure 1.8(c). Apart from these works numerous works have been reported in this frequency regime where broadband cross-polarization conversion has been achieved in reflection mode as well as in transmission mode [65-68]. Near field coupling between the resonators of a unit cell has recently been used to achieve polarization conversion of linearly polarized light. In this context, Li et al. investigated cross-polarization conversion in an edge near field coupled MM structure composed of orthogonally twisted SRRs [69].

1.3.4 Challenges in developing polarization conversion devices

The development of polarization conversion devices is a difficult task. The conversion bandwidth and effectiveness of polarization conversion are influenced by several parameters, including the angle of incidence and polarization of the incident beam. We've gone over each of these elements in depth here.

1.3.4.1 Angle of incidence of the incident beam

The polarization conversion efficiency and the conversion bandwidth of a MM geometry depend upon the angle of incidence of the incoming light. Direction of the magnetic/electric field, as well as the direction of propagation, varies as the angle of incidence of incoming radiation changes, accordingly the incident beam is TE/TM wave. This certainly affects the resonance of the MM geometry and also the polarization conversion efficiency and the bandwidth. Hence the stability of conversion efficiency and the bandwidth in a larger range of angles of incidence is desirable. In various studies, it was shown that the polarization conversion of the proposed structures is limited within a certain range of angles of incidence [68, 70]. For the larger angle of incidence, the working band becomes narrower and also the conversion efficiency reduces significantly.

1.3.4.2 Polarization angle of the incident beam

Polarization of incident light plays a crucial role in the excitation of a MM geometry. If one changes the polarization of incident light, then the resonance of the MM structure suppresses and the transmission/absorption reduces significantly. In previous research, the polarization conversion in an MM structure was investigated for a certain incident light polarization. The dependence of polarization conversion efficiency and the bandwidth upon the polarization of incident light was overlooked. In our thesis work, we have tried to address this important aspect.

1.3.5 Important concept in the context of thesis

1.3.5.1 Near field coupled terahertz metamaterials

The electric/magnetic field allows for short-range near field coupling between the unit cell's nearest neighboring resonators. The electric coupling occurs through the split gap of the SRR and magnetic coupling occurs via the circulating current flow through the circumference. Numerous near field coupled MM geometries have been studied to understand different coupling mechanisms owing to their significance in the construction of various photonic devices. In this context, Singh et al. demonstrated a blue shift of resonance in the transmission spectrum of a near field inductively coupled planar MM geometry comprised of a single SRR array by varying the periodicities [71]. Near field inductive coupling is studied in another type of MM geometry which is composed of two orthogonal SRRs placed nearby [72]. Here one SRR has split gap oriented along the incident electric field and gets excited strongly. Because of the perpendicular orientation of the split gap w.r.t. the incident electric field, the other SRR can't be excited directly and behaves as the dark mode. In the combined MM geometry, the splitting of resonances occurs in the transmission spectrum due to the strong coupling. The exciting eigenmodes deviate from the spectral position of the eigenmode for the isolated uncoupled SRR. The coupling between the resonators leads to the mode hybridization effect which leads to the formation of symmetric and anti-symmetric modes. The strength of the resonance splitting can be reduced by reducing the coupling via increasing the separation between the resonators. The near field coupling in these kinds of structures can lead to the realization of various phenomena such as electromagnetically induced transparency (EIT) effect, polarization conversion, modulation etc [33, 69, 73]. Further near field capacitive coupling plays the dominant role when the split gap of two neighbouring resonators are placed face to face. In this context, Rao et al. studied a strongly near field coupled MM geometry comprised of two SRRs placed with their split gaps facing each other [74]. The split gap of the top resonator is varied keeping the split gap of the bottom resonator fixed. It is observed that the 1st order resonance almost remains constant but the 2nd resonance gets blue-shifted with an increase in the gap of the top resonator. Further, the near field coupling is varied between the resonators by changing the separation in their study.

1.3.5.2 Electromagnetically induced transparency effect in metamaterials

Electromagnetically induced transparency (EIT) is a quantum interference effect that enables the absorption of a specific beam of light to be cancelled while also forming a narrow transparency window with a steep linear dispersion. It has potential applications in the fields of slow light and enhanced nonlinear effects [75]. In 2008 Zhang et al. first demonstrated classical analogue of EIT in a metamaterial comprised of cut-wire structures made up of sliver on a dielectric substrate [76]. The classical analogue of EIT in various MMs has been actively studied in recent years by the scientific community since it can be obtained even at ambient temperature. In MMs, the EIT effect is caused by the near field coupling between a bright and a dark mode. Due to the greater confinement with the applied electric field, the bright mode is usually linked with a broader resonance spectrum. The dark mode, on the other hand, has a narrower resonance spectrum due to its lower coupling with the incident electric field. For EIT to occur both the bright and dark modes should have similar resonance frequencies with a very little deviation. The EIT effect can also arise when a super-radiant and a sub-radiant mode are coupled together, with both modes having a greater coupling with the incident electric field. Using different MM structures such as strip, single-gap SRRs, and others, the EIT effect has been demonstrated in the gigahertz, near-infrared, visible, and terahertz frequency regimes [77-86].

1.3.5.3 Polarization insensitive metamaterials

The polarization direction of the incident light has a significant impact on the transmission/absorption of an MM geometry. If one switches the polarization, the excitation of the MM geometry gets suppressed or even disappears. Due to this strong polarization dependency, these MMs have limited practical applications. Efforts have been made to design polarization-independent single or multi-band absorbers [87, 88] and filters in the THz frequency regime. The polarization independence of these MM geometries originates from the symmetry of the structures. The polarization direction affects the electromagnetically induced transparency (EIT) effect in MMs, as discussed earlier. The EIT effect has promising applications in sensing and slow light. Polarization insensitive single band EIT effects have been reported in earlier studies [89, 90]. However, it is difficult to design MM geometries that exhibit a polarization-insensitive multiband EIT effect. In this thesis work, we have focussed to explore the polarization-insensitive sensing capability of a MM geometry that exhibits a dual-band EIT effect. This will be discussed in detail in chapter 5.

1.4 Planar Terahertz Metamaterials for sensing

1.4.1 Sensing at terahertz frequencies

Recently, it has been found that THz MMs have potential application in the field of sensing. MMs interact with the incident electromagnetic wave which causes stronger localization and enhancement of the field. Hence MMs can provide an excellent platform for sensing with higher sensitivity and resolutions. The sensing capability of terahertz MMs with numerous geometries such as SRR, cut-wire, asymmetric resonators has been investigated so far to explore their potential in thin-film based sensing. In this context, Driscoll et al. first experimentally demonstrated a THz MM sensor based on an array of SRRs patterned on a silicon substrate coated with a thin layer of benzocyclobutane (BCB) which is shown in Figure 1.9(a) [91]. With the addition of silicon nanospheres on top of the SRR array, a gradual redshift in the resonance frequency was observed. Later Ohara et al. examined thin-film sensing in a MM geometry comprised of square double SRRs patterned on a silicon substrate [92]. The structure exhibits multiple resonances. It was shown that the resonances get red-shifted when the thickness of the photoresist coated on top of the MM geometry was varied. Tao et al. proposed a biosensor composed of SRRs coated on silicon nitride substrate (SINx) [93]. In this study, they have made a comparison between the sensing capability of the MM geometry coated on SINx and silicon substrates. It was shown that SINx has greater sensitivity as compared to silicon owing to its lower refractive index. Hu et al. studied lactose concentration detection in an MM configuration consisting of an array of square SRRs placed on top of the quartz substrate in 2019 [94]. However, these SRR based MM sensors have limited detection sensitivity. As compared to the LC and dipolar resonances, Fano resonance has a sharper profile and higher Q factor. For very sensitive refractive index detection, a number of Fano resonance MM sensors based on asymmetric SRRs have been suggested. Debus and Boliver reported a double-opening asymmetric SRR structure which exhibits a narrow resonance peak with a Q factor of 40 [95]. It was shown that when a dielectric substance of permittivity of 3.2 and thickness of 10 nm was coated on top of the SRR, the resonance peak gets shifted by 5 GHz. Singh et al. studied the sensing capabilities of the

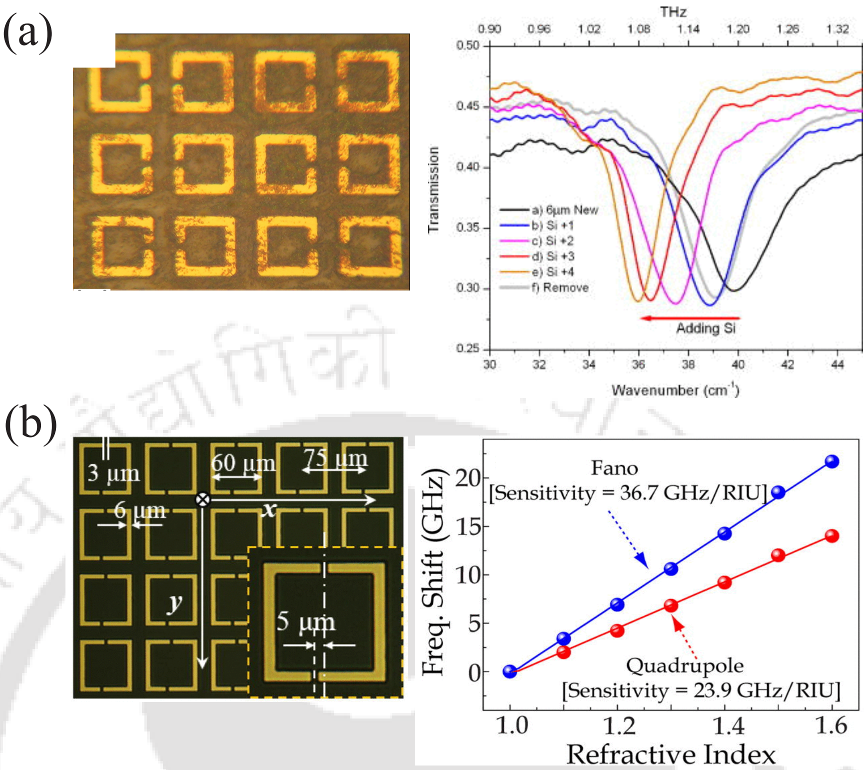

Figure 1.9: (a) A planar metamaterial sensor composed of an array of symmetric SRRs along with the transmission spectra. Reprinted from [91] with permission of AIP Publishing. (b) A MM sensor based on SRRs with asymmetric double split gaps along with the frequency shift vs refractive index plot for quadrupole and fano resonances. Reprinted from [96] with permission of AIP Publishing.

fano resonance and quadrupole resonance in an asymmetric double opening ring-type geometry as shown in Figure 1.9(b) [96]. Srivastava et al. have demonstrated a highly sensitive dual surface Fano resonator made of asymmetric SRR coated on a low refractive index polyimide substrate [97]. Multiband Fano resonance-based MM geometries were also examined to decrease the sensing error induced by environmental variables such as a change in temperature, humidity, and so on [98,99]. Recently MM absorbers are also investigated for their excellent sensing capability. In this context, Saddelin et al. proposed a perfect MM absorber that exhibits an absorption peak of amplitude 0.99 and a Q factor of 22 [100]. Sensitivity of 300 GHz/RIU and FOM of 2.94 was reported in this study. He et al. demonstrated a novel ultrasensitive sensor comprised of complementary CW and an SRR both made up of graphene [101]. The structure provides the advantage of dynamical control of the sensing range. Recently toroidal MMs are also used in the field of sensing. Toroidal resonance exhibits lower radiation loss and a higher Q factor. Gupta et al. demonstrated thin-film sensing in a MM geometry consisting of a double split gap square-shaped metallic ring which shows high Q factor via sharp toroidal resonance [102]. This study gives an excellent platform for more innovative sensing approaches.

1.4.2 Sensing with Electromagnetically induced transparency effect

In EIT, the transparency peak possesses a high Q factor owing to the low loss. Hence EIT MMs have potential in ultrasensitive refractive index and biological sensing. In this context, Li et al. presented a liquid sensor with a coupled MM geometry that consisted of two identical SRRs symmetrically arranged on opposite sides of the central vertical strip [103]. It was shown that the EIT peak gets red-shifted with a maximum of 54 GHz with the change of water concentration in the water-dioxin mixture. Wei et al. reported an EIT based sensor with a sensitivity of 294 nm/RIU and FOM of 42 in an all-dielectric metasurface comprised of two mutually perpendicular silicon nanoscale bars [104]. Further Pan et al. demonstrated another MM sensor with a higher refractive index sensitivity in a planar geometry [105]. Yan et al. demonstrated biosensing application of EIT effect in a MM comprised of asymmetric double split-ring resonators (DSRRs) deposited on polyimide dielectric layer [106] as shown in Figure 1.10(a). The structure exhibits an EIT peak at 1.67 THz which possesses a sensitivity of 455.7 GHz/RIU. Cai proposed a graphene-based MM which exhibits the EIT effect due to the couplings between two graphene rings [107]. This sensor has a sensitivity of 2.26 THz/RIU and FOM of 6.21. Recently, the focus has been given to exploring the potential of the multi-band EIT effect in MMs in the field of sensing. In this context, Zhu et al. investigated thin-film sensing in a planar MM geometry that exhibits dual-band EIT with transparency peaks at 0.89 and 1.56 THz respectively [108]. We have shown the unit cell of the dual-band metamaterial sensor in Figure 1.10(b). The 1st transparency peak has a Q factor of 14.3, a sensitivity of 280.8 GHz/RIU, FOM of 4. On the other hand, the 2nd transparency peak has better sensing capability with a Q factor of 56.9, S=201.6 GHz/RIU and FOM of 11.5. Shen et al. demonstrated a dual-band EIT sensor based on toroidal dipolar couplings in an $E-\epsilon$ shaped metasurface [109]. In this work, the sensitivities of the two peaks were calculated as 1.57 GHz/RIU and 2.10 GHz/RIU respectively. However, the polarization of the incident light strongly influences the sensing capabilities of these MM structures, limiting their practical applicability. As

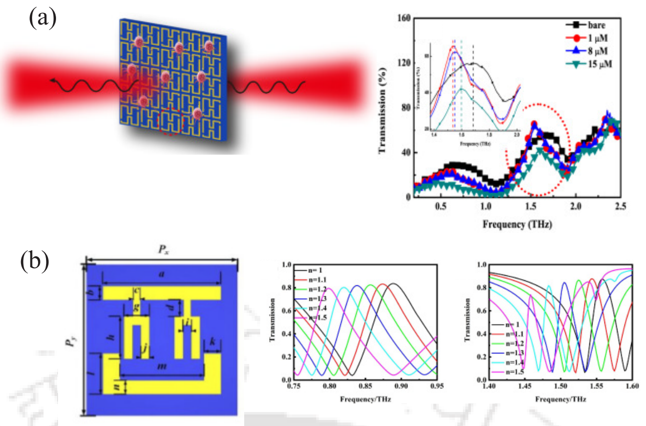

Figure 1.10: (a) A metamaterial-based biosensor along with the transmission under different concentrations of oral cancer cells. Reprinted from [106], © 2019, with permission from Elsevier. (b) A dual-band EIT like metamaterial sensor. The frequency shift of two EIT peaks with differing refractive indexes of an analyte is also depicted here. Reprinted with permission from [108] © The Optical Society.

a result, MM designs with polarization-insensitive sensing capacity in the multiband frequency range are preferred. In this thesis, we have focussed on this aspect which will be discussed in chapter 5 in detail.

1.4.3 Quality factor, sensitivity and figure of merits

The sensing capability of a traditional sensor is evaluated by three well-known parameters viz. quality factor, sensitivity and figure of merit. The quality factor (Q) is defined as $Q = \frac{f_0}{FWHM}$, f_0 is is the resonance frequency which is determined by the structural parameter and the external environment, FWHM is the full width at half the maximum of the resonance peak. Q factor determines the sensitivity and resolution of the sensor. Higher the value of the Q factor higher will be the sensitivity and resolution. The sensitivity of a refractive index sensor is defined as $S = \frac{\Delta f}{\Delta n}$, where Δf represents the frequency shift and Δn represents the change in the substance's refractive index that has to be measured. The characteristics of sensors working in different frequency bands can be compared by another important parameter namely the figure of merits (FOM). The FOM is defined as $FOM = Q \times S = \frac{S}{FWHM}$. As a result, sensors with a high sensitivity and Q factor will have more sensing capacity.

1.5 Slow light effect

The phenomenon of slow light occurs when the group velocity of light (v_g) becomes less than the velocity of light in free space, i.e. ($v_g < c$). EIT effect in MMs has the potential to slow down the light. The EIT effect is caused by a fast shift in the medium's refractive index, resulting in a sharp linear dispersion in the transparency area. The slow light effect is caused by the steep linear dispersion inside the narrow transparency window, which slows the group velocity of light. The EIT effect is associated with a stronger phase dispersion in the medium which results in a larger group delay of the pulse as compared to its propagation time in free space. The group delay can be calculated from the transmission phase shift (ϕ) by the following equation

$$\tau_g = \frac{-d\phi}{d\omega}, \tag{1.12}$$

and the group refractive index is

$$n_g = \frac{c}{v_g} = \frac{c}{h}\tau_g = -\frac{c}{h}\frac{d\phi}{d\omega}, \tag{1.13}$$

where h is the MM sample's effective thickness. Within the transparency window, the group refractive index derived using this formula is extremely high.

Wang et al. exhibited the EIT effect and slow light in a plasmonic metasurface made up of nanoring and nanorod-based compound structures [110]. In another study, Zhu et al. reported a multiband slow light effect in the GHz frequency range [111]. Their proposed MM geometry is comprised of three asymmetric parallel cut wires (CWs). It was shown that a Gaussian pulse centred at 8.9 GHz is delayed by 1.925 ns within the 1st transparency window and another Gaussian pulse centred at 10.6 GHz is delayed by 0.858 ns within the 2nd transparency window as it propagates through the MM. In the THz frequency regime, Gu et al. reported active control of the EIT effect in a planar MM comprised of a CW and two SRRs [112]. The schematic of the planar MM geometry is shown in Figure 1.11(a). The EIT window was actively tuned by exciting the Si island filled in the split gap of the dark SRR with an infrared beam of power ranging from 0 mW to 1350 mW. Further, it was observed that a wave packet gets delayed while passing through the MM. The group delay was also actively tuned by the different excitation power of the beam. Zhang et al. showed the dual-band EIT effect and slow light in a planar MM design that included a CW and two distinct SRRs, as shown in Figure 1.11(b) [114]. The calculated group refractive index at the 1st and 2nd

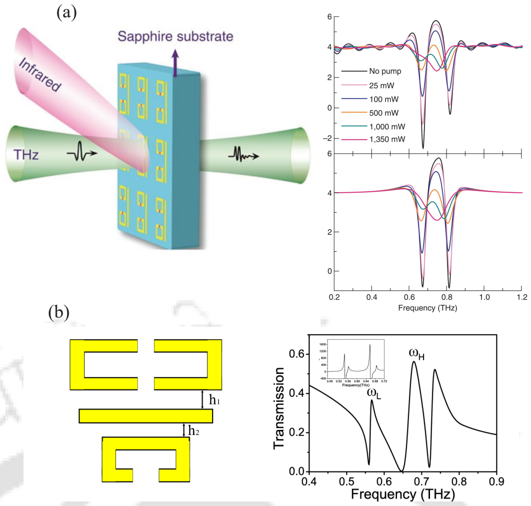

Figure 1.11: (a) Schematic illustration of a planar MM configuration comprised of a CW and two SRRs which exhibits an EIT like effect and active control of the group delay in the proposed structure under different excitation of the pump beam. Reprinted by permission from Springer Nature Customer Service Centre GmbH (Springer Nature, Nature Communications) [112] (2012). (b) Planar MM geometry is comprised of a CW and two different SRRs which exhibits dual-band EIT effect and slow light phenomenon in the terahertz frequency range. Reprinted with permission from [114] © The Optical Society.

transparency peaks were 246.9 and 377 respectively. Further Xu et al. reported a MM geometry comprised of monolayer graphene with rectangular defects [115]. The slow light effect was investigated and a high group refractive index of 545 was reported in this study. The investigations so far have reported simultaneous modulation of the slow light effect and transparency windows in the multiband frequency regime. Independent control of the transparency windows and the dispersion properties could be significant in the construction of frequency selective photonic components. In this thesis work, we have tried to address this aspect.

1.6 Plan of thesis

In thesis work, we have investigated polarization conversion of incident terahertz and sensing in planar metamaterial structures. In a near-field coupled planar MM geometry, we have investigated gradual cross-polarization conversion of terahertz waves in transmission mode. Further, we have demonstrated broadband efficient terahertz polarization conversion in a planar MM configuration by rotating the structures at various angles w.r.t the incident terahertz. We have also investigated the sensing capability of polarization-insensitive dual-band electromagnetically induced transparency effect. Independent modulation of electromagnetically induced transparency effect and dispersion in the multiband frequency spectrum is also studied in another planar coupled MM geometry. The planned work has been organized into seven chapters in this thesis. The following is a chapter-by-chapter summary of the thesis:

Chapter 1 provides an overview of the terahertz field and its applications. We have also discussed planar terahertz metamaterials and their applications in different areas. The status of polarization devices, their significance and challenges in developing them are discussed in this chapter. Further, we have given a brief overview of sensing and the potential of electromagnetically induced transparency effect in the context of thin-film sensing. The slow light phenomenon in the context of the EIT effect is also discussed in this chapter.

Chapter 2 discusses the design of planar metamaterial structures using commercially available numerical software CST Microwave Studio. The fabrication process of the samples using the electron beam lithography technique is also discussed step by step. Further, the procedure to measure the transmission spectra through fabricated samples using terahertz time-domain spectroscopy (THz-TDS) is illustrated.

Chapter 3 examines gradual cross-polarization conversion of terahertz wave. The unit cell of the proposed geometry is comprised of two circular split ring resonators having a single split gap. We have rotated one resonator concerning to the other from 0° to 180° in the steps of 15° and investigated co- and cross-polarization components of the transmitted terahertz through our proposed geometry. Based upon the angle of rotation between the resonators, we have tuned the cross-polarization amplitude from minimum to maximum and then back to the minimum. In order to understand the polarization conversion in our MM geometry, we have employed a semi-analytical model. The ability to control linear polarization conversions can be significant in the development of THz polarimetric devices.

Chapter 4 investigates numerically and experimentally an ultra-wideband efficient polarization conversion of linearly polarized terahertz wave in a planar metamaterial geometry comprised of C shaped resonator. Both the co- and cross-polarization transmission spectra of the proposed MM configuration have been studied for numerous polarizations of incident terahertz starting from 0° to 90° in steps of 15°. Our design promises cross-polarization conversion of 40% from 1.22 THz to 2.75 THz with a maximum of 45% when the MM design is rotated by 45° with respect to the incident terahertz. The change in polarization excites an electric dipole in the C resonator, which radiates electric field in the co-and cross-polarization. The polarization conversion has been explained with induced electric field profiles as well as surface current profiles for different polarizations. It is shown that the change in dimension of the C resonator causes a shift of the transmission spectrum. Numerically simulated results are in good agreement with the experimental results. Our design eliminates the complexity of the fabrication of multilayer structures and opens avenues to design ultra-wideband and efficient polarization rotation devices in the terahertz frequency regime.

Chapter 5 demonstrates experimentally and numerically a metamaterial (MM) geometry capable of showing polarization insensitive dual-band electromagnetic induced transparency (EIT) effect. The suggested MM configuration's meta-molecule unit is made up of a strip and two asymmetric split ring resonators (SRRs). The existing meta-molecule unit is changed into a cross-like structure studded with four SRRs for polarization insensitive dual-band EIT effect. The transmission profile of the structure is same for two orthogonal polarization orientations of the incident light, indicating that it has a polarization independent response. We used a four-level tripod (FLT) atomic system based analytical model in order to better comprehend and explain our numerical findings. We investigated the impact of transmission with a change in the refractive index of analyte of 10 μm coated on the top of the MM resonators to illustrate the practical application of our study. Our research might potentially aid the development of slow light devices, modulators, and filters.

Chapter 6 investigates a planar terahertz metamaterial (MM) geometry capable of demonstrating a multi-band electromagnetically induced transparency phenomenon that is independently controllable. Due to the near field coupling between the bright mode of the cut-wire (CW) and the dark modes of a pair of asymmetric double C resonators (DCRs), the MM structure shows a multi-band EIT effect. The independent modulation is done by shifting one asymmetric DCR relative to the CW while leaving the other asymmetric DCR unchanged. We also look at the steep dispersive behaviour of the transmission spectra within the transparency windows, as well as the features of slow light. The study might be extremely useful in the development of multiband slow light devices, buffers, and modulators.

In Chapter 7 we have summarized the important findings of our research work and also discussed the future scope of research in terahertz metamaterials in the context of our study.

CHAPTER 2

METHODOLOGY

In this chapter, we will discuss the methodology i.e. the techniques/procedures that we have used to execute our research projects. The different steps are as follows:

- Simulation tools
- Sample fabrication
- Characterization
- Theoretical study

2.1 Simulation tools

Before moving further with the difficult and expensive fabrication process, it is important to get an idea about the critical parameters of terahertz metamaterials so as to achieve the required outcomes. We utilised CST Microwave Studio, a commercially available numerical simulation programme, for the simulation. It's a numerical electromagnetic 3D simulation tool that works using the finite integration algorithm [116].

The initial template of CST Microwave Studio is illustrated in Figure 2.1. Time-domain solver, frequency-domain solver, eigenmode solver, and multilayer solver are the possible tools available in CST Microwave Studio for simulations with the options of

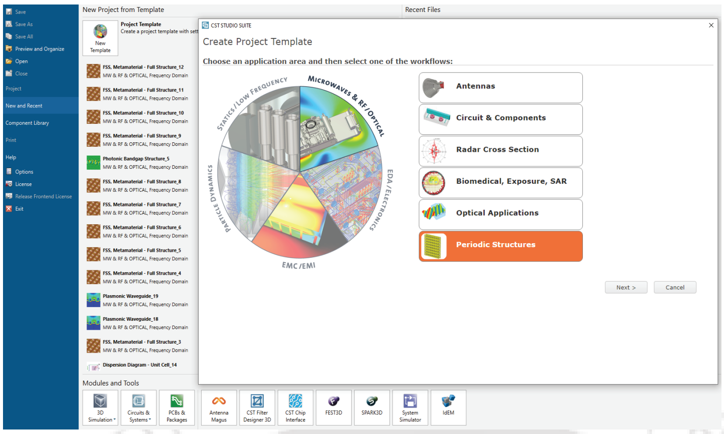

Figure 2.1: Initial template of CST Microwave Studio.

including tetrahedral and hexahedral shaped meshing for the geometries. The whole simulation area is split into tiny uniform cubes of varying sizes in hexahedral meshing, while the objects are partitioned into small tetrahedrons and the remainder of the simulation space is left unmeshed in tetrahedral meshing. The mesh size of the solver determines the simulation's accuracy. The smaller the mesh size, the more exact the findings will be. However, this will increase the computation time and memory requirements. The most versatile technique is the time domain solver with hexahedral mesh, which can yield the whole broadband frequency behaviour of the simulated device from only one calculation run. Most high-frequency applications, such as transmission lines, antennas, filters, and connectors, benefit greatly from this solution. For structures that are electrically considerably smaller than the shortest wavelength, the time domain solver is less efficient. In this scenario, utilising a frequency domain solution to solve the issue is useful. For narrowband issues, such as filters, or when the usage of a tetrahedral grid is desirable, the frequency domain solver may be the method of choice. S-parameters for strongly resonant structures may be calculated quickly using a frequency-domain solver. Multilayer solvers are utilised for structures like microstrip filters on printed circuit boards. In the case of filters, direct computation of the operating modes is frequently necessary rather than S-parameter simulation. The eigenmode solver is appropriate for these applications since it efficiently calculates a finite number of modes in closed electromagnetic devices.

We simulated metamaterial structures in this thesis work, and we employed a frequency-domain solver using a tetrahedral mesh to do so. We used a tetrahedral mesh

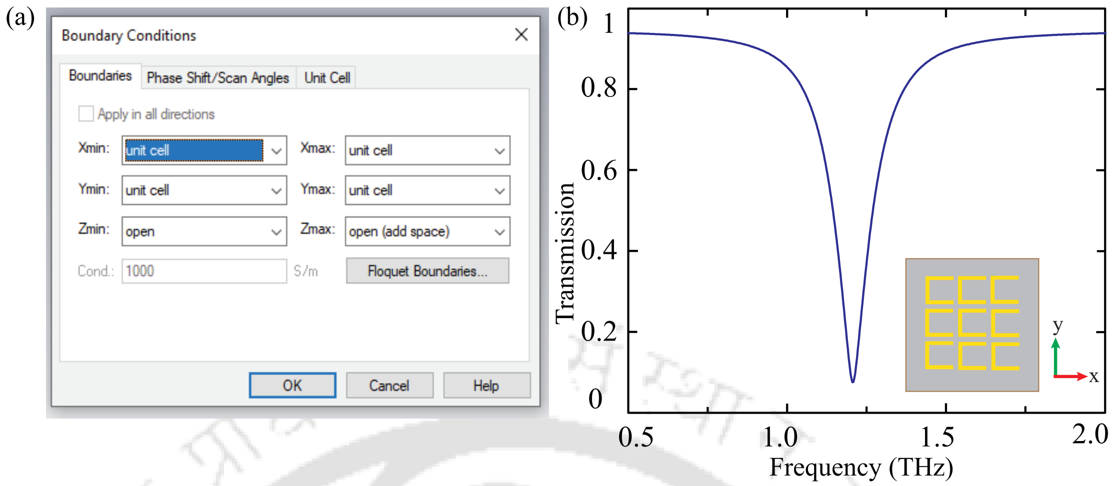
Boundary Conditions

Apply in all directions ☐

Xmin: unit cell

Xmax: unit cell

Ymin: unit cell

Ymax: unit cell

Zmin: open

Zmax: open (add space)

Cond.: 1000 S/m

Figure 2.2: (a) Boundary conditions used to simulate metamaterial geometry using CST Microwave Studio. (b) Transmission along with the schematic of the MM geometry. In the schematic diagram, gold resonators are shown by the yellow color and the quartz substrate is depicted by the grey color. The green arrow depicts the direction of the electric field of incident terahertz.

with a size of $\lambda/10$ in this solver, where λ is the wavelength of the incident radiation. In the x-y plane, we employed unit cell boundary conditions, and ports with 18 modes were set for the best accuracy. The MM structures are simulated using linearly polarized incident light and open boundary conditions along the path of light. We have shown boundary conditions used and the transmission spectrum of a MM geometry in Figures 2.2(a) and 2.2(b) respectively. The schematic of a MM geometry comprised of a SRR is shown in the inset of Figure 2.2(b). The S parameters are used to store transmissions and reflections. The magnitude of the S-parameter, i.e. |S21|, has been displayed in the transmission versus frequency spectrum. In our research, gold metals were employed to create metamaterial structures. Gold has an electrical conductivity of $\sigma = 4.56 \times 10^7 Sm^{-1}$ [117]. Depending on the availability of the substrate for the experiment, we employed loss-free silicon with a dielectric permittivity of $\epsilon_r = 11.9$ or quartz with a dielectric permittivity of $\epsilon_r = 4.68$.

2.2 Fabrication of metamaterial samples

We have fabricated metamaterial samples using conventional electron beam lithography techniques in the cleanroom environment. The procedure of preparing samples is shown in Figure 2.3. For the fabrication purpose, we have used a milky quartz wafer as the

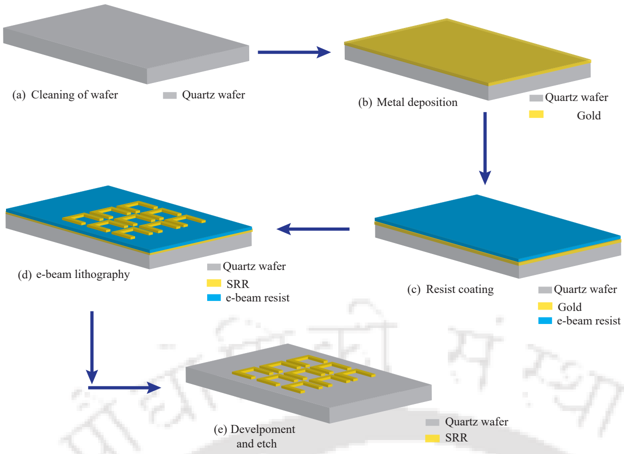

Figure 2.3: Procedure of fabrication of terahertz metamaterial samples in step by step using electron beam lithography.

substrate having a refractive index of n=2.12 and thickness of 500 μm. The MM samples are made up of gold of conductivity $\sigma = 4.56 \times 10^7 Sm^{-1}$. The basic steps of preparing samples are as follows:

1. Cleaning the substrate: It is very crucial to clean the substrate to remove any dust particles, moisture or any other residues for good resist adhesion. We have cleaned the wafer using ultrasonic cleaning with Trichloroethylene, Acetone and Methanol for 2 minutes each followed by heating on the hot plate at $200°C$ for 5 minutes.

2. Metal Deposition: In the next step, we have deposited a 200 nm gold layer on top of the wafer using a direct current magnetron sputtering system.

3. Electron beam resists coating: Next, we have coated AR-N 7520.11 new series E-beam resist (negative E-beam resist) on top of the sample using a spin coater with a spinning speed of 4000 rpm for 60 seconds. For the dehydration bake, we have kept our sample on the hot plate at $85°C$ for 60 seconds.

4. Lithography: For the lithography purpose, we have employed standard e-beam lithography with an accelerating voltage of 15 kV.

5. Development: Next, we have dipped the sample in the EBL developer for 60 seconds and in the IPA for another 60 seconds.

6. Etching: Next, the excess metal along with the resist was removed from the sample using reactive ion etching with Ar-O2 plasma. Finally, we got our desired gold metamaterial resonators on top of the milky quartz substrate.

2.3 Characterization of the terahertz metamaterial samples

To measure the transmission spectra of the fabricated samples, we have used Terahertz Time Domain Spectroscopy (THz-TDS) set up which is shown in Figure 2.4. This spectroscopy (THz-TDS) has become a very important tool, which is used in various fields such as in material science, engineering and medicine [118,119]. As compared to the other spectroscopic techniques this technique is superior because TDS provides both amplitude and phase information of the electric field. Our setup is driven using Ti: sapphire femtosecond (fs) laser having a repetition rate of 80 MHz. The pulse width of the employed laser is 50 fs. The central wavelength is 800 nm. Here the incident laser beam is divided into two beams: probe beam and pump beam using a (70:30) beam splitter. The pump beam is used to generate a linearly polarized terahertz beam through LT-GaAs based photoconductive antenna (BATOP GmBH). PCA is one of the most widely used components for the generation of terahertz radiation [120]. The PCA consists of two metal electrodes and semiconducting material such as low-temperature grown GaAs (LT-GaAs) as the substrate here due to its higher carrier mobility and shorter carrier lifetime.

The gap between the electrodes is typical of the order of 5 μm and acts as a capacitor. Femtosecond laser pulse is focussed into the gap. The photon energy of the pulse is taken as greater than the bandgap of the semiconductor used. Due to the excitation of the laser beam, photo carriers will be generated. Further, these photo carriers are driven by the external bias voltage, which gives rise to rapid current flows between the metal contacts. Since holes usually have much lesser mobility than electrons, the contribution of holes can be ignored in most cases. The current density will be proportional to the carrier density, applied bias field and mobility of generated photo carriers in this case. Since the generated photocurrent is time-varying, it will radiate electromagnetic fields in the form of THz radiation.A schematic of terahertz generation using PCA is shown in Figure 2.5. From Maxwell equations, the THz electric field is proportional to the time

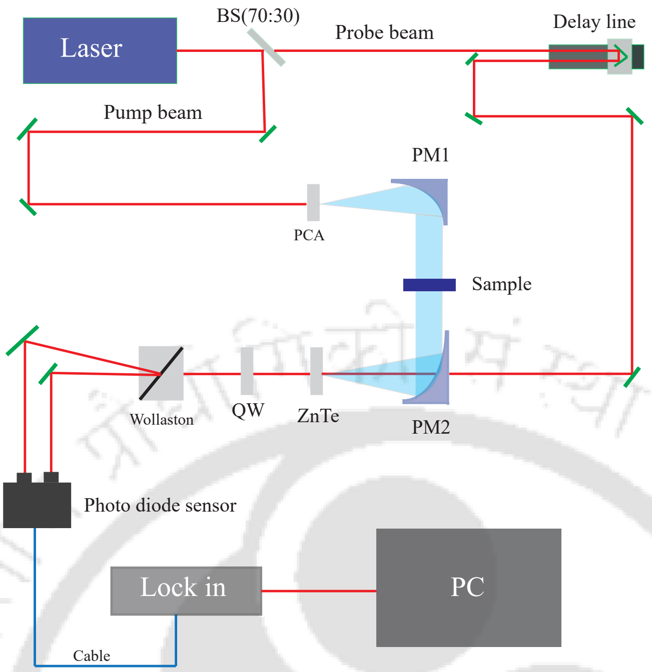

Figure 2.4: Schematic of the THz Time-domain setup. BS-Beam splitter, PM-Parabolic Mirror, PCA-Photo Conductive Antenna, QW-Quarter Waveplate, WP-Wollaston Prism.

derivative of the transient current, which can be expressed as $E(t) \propto \frac{dJ}{dt} \propto \frac{dn}{dt} E_b$.

On the other hand, the THz beam is detected by the probe beam via electro-optical sampling using a ZnTe single crystal of thickness 2 mm and orientation <110>. In this process, the electric field of the THz pulse is detected by changing the polarization of the probe laser beam in an Electro-Optic (EO) crystal [121,122]. When the THz beam propagates with the probe beam inside the EO crystal, the induced birefringence of the crystal by the THz beam causes a change in the polarization of the probe beam. By measuring the birefringence, or the change in the polarization state of the beam, the THz electric field strength can be determined. Without the THz pulse, there will be no birefringence inside the crystal. When a linearly polarized optical probe pulse passes the EO crystal, there will be no change in its polarization. Further, when the beam passes through a quarter-wave plate, it becomes circularly polarized. The circularly polarized beam is then spitted into its two orthogonal components by a Wollaston prism and each component is sent to one of the photodiodes of a balanced detector. The detector connected to a lock-in amplifier, measures the difference signal from the two photodiodes, giving zero reading without the THz pulse. On the other hand, in the presence of the THz pulse, the induced birefringence rotates the polarization of the probe pulse, making it elliptical,

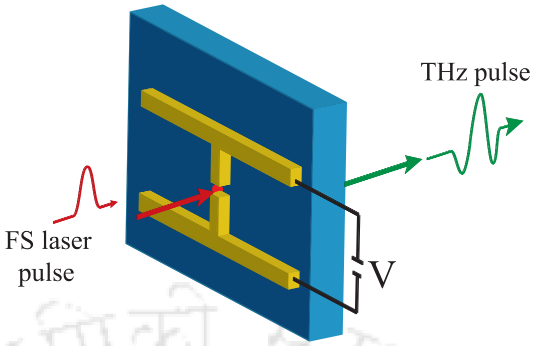

Figure 2.5: Schematic of terahertz generation using a photoconductive antenna. The PCA is comprised of two metal electrodes and is fabricated on an LT-GaAs substrate.

thus introducing a signal imbalance between I_y and I_x, where I_y and I_x are the signals detected by the two ports of the balanced photodetector. This difference between the two signals can directly give the electric field amplitude information of the THz pulse by using the following equations:

$$I_S = I_y - I_x = I_0\phi \tag{2.1}$$

Here

$$I_x = \frac{I_0}{2}(1 - sin\Delta\phi) \propto \frac{I_0}{2}(1 - \Delta\phi) \tag{2.2}$$

and

$$I_y = \frac{I_0}{2}(1 + sin\Delta\phi) \propto \frac{I_0}{2}(1 + \Delta\phi) \tag{2.3}$$

where, I_0 represents the total intensity of the probe beam and $\Delta\phi$ is phase retardation between the two polarization components. Note that in these equations, an approximation $\Delta\phi \ll 1$ is used, and thus a linear relationship between the THz electric field and the signal is seen in equation (2.3).

By varying the time delay of fs laser pulses between the THz source and the ZnTe crystal using a motorized stage, the transient THz electric field is measured. Since here, the amplitude of the electric field is recorded in the form of a time-domain signal, this spectroscopic measurement is termed the THz time-domain spectroscopy. The recorded signal can be converted to the frequency domain by performing the FFT (Fast Fourier Technique). Figures 2.6 (a) and (b) illustrate the recorded signal in the time domain and frequency domain respectively. The normalized transmission spectra $|t(\omega)|$ spectrum of the sample is determined by taking the ratio between the Fourier transform of the

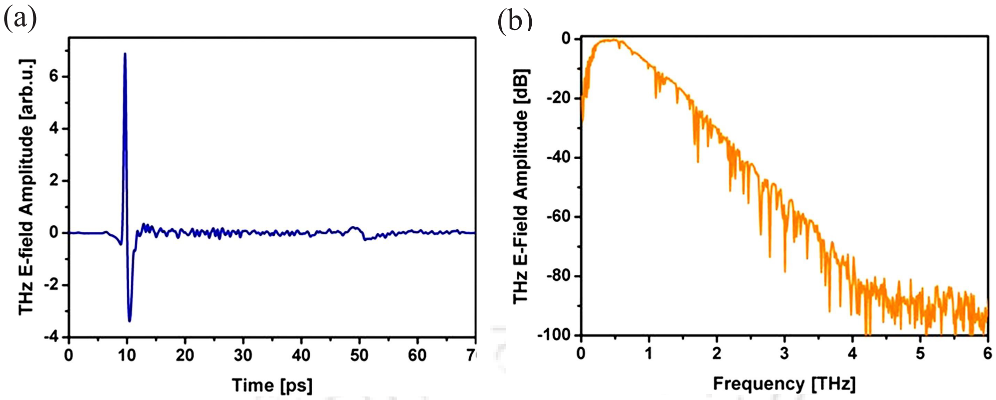

Figure 2.6: Recorded transmission-using TDS in (a) time domain and (b) frequency domain. Reprinted from [123], © 2019, with permission from Elsevier.

measured time-domain terahertz pulses of the sample ($|E_S(\omega)|$) and reference ($|E_R(\omega)|$. In the frequency domain spectra, the spectral resolution of THz-TDS, usually defined as $\Delta\omega$ is determined by the temporal scanning range, say T as the bandwidth of THz-TDS is given by,

$$\Delta\omega = \frac{2\pi}{T} \tag{2.4}$$

The bandwidth ($\Delta\Omega$) of the terahertz time-domain spectroscopy is given by,

$$\Delta\Omega = \frac{2\pi}{\delta T} \tag{2.5}$$

where δT is the temporal sampling interval. This technique provides both phase and amplitude information and hence becomes significant in extracting both the absorption and dispersion properties.

In our research work, we have also used another commercially available terahertz Toptica system (Terahertz frequency-domain spectroscopy) to measure the transmission response of the fabricated samples in some projects. This setup has a high-frequency resolution of 2 MHz. The schematic of the setup is illustrated in Figure 2.7. One of the major components of this setup is the photo-mixer, which is a microscopic metal-semiconductor-metal structure. InGaAs photo-mixer is used in our set-up. Here two near-infrared light beams having adjacent frequencies from the two laser diodes illuminate the photo-mixer. By applying a bias voltage to the metal electrodes, a photocurrent is being generated that oscillates at the beat frequency. An antenna structure surrounding the photo-mixer translates the oscillating photocurrent into the terahertz wave. The

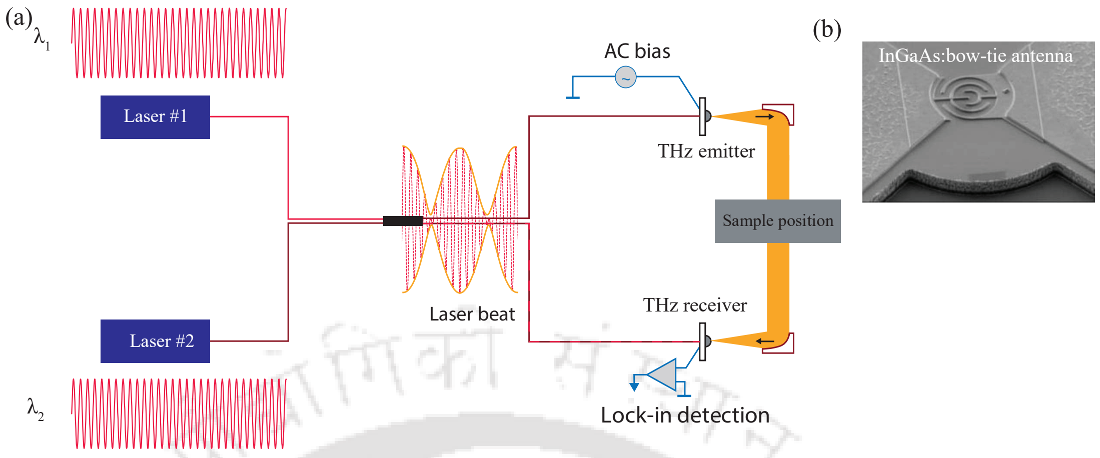

Figure 2.7: (a) Schematic of terahertz frequency-domain spectroscopy setup (Toptica system). (b) Micrograph image of InGaAs: bow-tie antenna.

generated terahertz wave has frequency exactly at the difference frequency of the two laser diodes. Hence, in this setup, only one frequency can be generated at a time. By tuning the lasers, different terahertz frequencies can be generated. For the detection of the generated terahertz wave, another unbiased photo-mixer is employed. The photomixer is illuminated with both the generated terahertz wave and the optical laser beam. The terahertz wave acts as the bias voltage and generates a voltage in the antenna. The generated photocurrent typically lies in the nano ampere range and is proportional to the amplitude of the incident terahertz field, and depends upon the phase difference between the terahertz wave and the optical beam. Hence, by measuring photocurrent at the photoconductive antenna-based detector, terahertz radiation can be detected. To resolve the spectral response of the MM sample, the frequency was swept from 50 GHz to 1220 GHz in 40 MHz step size and integration time was three milliseconds. To reduce the absorption of terahertz radiation by water vapour, the measurement was carried out at room temperature in dry nitrogen atmosphere.

2.4 Theoretical model

To validate our numerical findings we have employed three different analytical models that are based on RLC circuit, coupled harmonic ossilator systems and four level tripod atomic systems (FLT). In RLC circuit approach, a single SRR is modeled with an equivalent RLC circuit which exhibits resonance at a specific frequency depending upon the shape and size of the SRR. The FLT system consists of four different energy levels where transition between these levels leads to the excitation of dual-band EIT effect. In coupled oscillator systems, the masses are connected to each other with springs of different spring constants. Here the mass driven by the external harmonic force drives other masses. The details of these models are discussed in chapter 3, chapter 5 and chapter 6 as per their application in various projects pertaining to different metamaterial concepts.

CHAPTER 3

GRADUAL CROSS POLARIZATION CONVERSION OF TERAHERTZ WAVES IN NEAR FIELD COUPLED METAMATERIALS

As discussed in chapter 1, the polarization manipulation of an electromagnetic wave has applications in different fields such as sensing, imaging and optical communications etc. The artificially engineered MMs, can be used for polarization conversion applications. The focus have been given to examine the simple MM resonator for its potential in polarization conversion. The near field coupling between the resonators can provide an extra degree of freedom and flexibility for converting the polarization of incident electromagnetic wave. In near field coupling, one resonator generally acts as the bright mode and the other one behaves as the dark mode. The bright mode couples strongly with the incident electromagnetic field and excites the dark mode which causes polarization conversion. The near field coupling has been investigated either in broadside or edge coupled MM geometries [124,125]. In broadside coupled MM, bilayer configuration is used for near field coupling. In the edge coupled MMs, the resonators are placed side by side. The edge coupled MM geometries have also been employed to acheive polarization conversion of incident light. In this context, Cong et al. investigated the effect of intra

---

Part of the results of this chapter have been published in the following paper Gradual cross polarization conversion of transmitted waves in near field coupled planar terahertz metamaterials SJM Rao, R Sarkar, G Kumar, DR Chowdhury- OSA Continuum 2(3), 603-614, 2019.

near field coupling on co-and cross-polarization transmission spectrum in a metasurface comprised of two orthogonal SRRs [126]. In a similar study, Cong et al. demonstrated polarization control in a near field inductively coupled metasurface [127]. Recently, Li et al. demonstrated polarization conversion of incident terahertz in a near field coupled MM geometry comprised of edge coupled twisted SRR pairs [69]. These investigations have mainly focused on achieving polarization conversion of linearly polarized light for its perpendicular polarization conversion. Several applications require gradual polarization conversion and its control. In this chapter, we address it with a simple planar MM geometry in the THz frequency regime.

We have proposed a metamaterial unit cell comprising of two near field coupled circular resonators on a silicon substrate with the ability to gradually rotate and control linearly polarized light. We examine the co- and cross-polarization transmission for different rotation angles of one resonator with respect to another resonator. In the next section, the design of MM geometry has been discussed along with the effect of rotation angle on the coupling of fundamental LC resonances. The numerical results are discussed in detail in the subsequent section. We have further discussed the lumped-element RLC circuit model to interpret and validate the numerical findings.

3.1 Metamaterial design

Design of THz metamaterial is very crucial in order to accomplish variable magnitude of the co and cross polarization responses. In our proposed metamaterial configuration, metamolecule (unit cell) is comprised of two circular split ring resonators (SRRs) and separation between two resonators is fixed at 1 μm throughout this study. A schematic of the proposed configuration is shown in Figure 3.1. We have assumed silicon of thickness 50 μm as the substrate with a permittivity of ϵ = 11.9 and negligible loss. Other dimensions of substrate are assumed to be, length x breadth = 100 μm x 60 μm. The unit cell is chosen to be much bigger in size compared to the resonators pair in order to avoid any inter metamolecular coupling. The circular SRRs as depicted in the figure 3.1 (b) are 20 μm and 16 μm in outer and inner radius, respectively, and made of gold layer of 200 nm thickness. The capacitive gap (g) and line width (w) of both the resonators are taken to be, same i.e. 4 μm. The geometrical parameters are kept constant throughout the analysis. In Figure 3.1(b), θ is the angle between the split gaps of left and right SRR and is changed from 0° to 180° during this study. We fix the right side resonator and

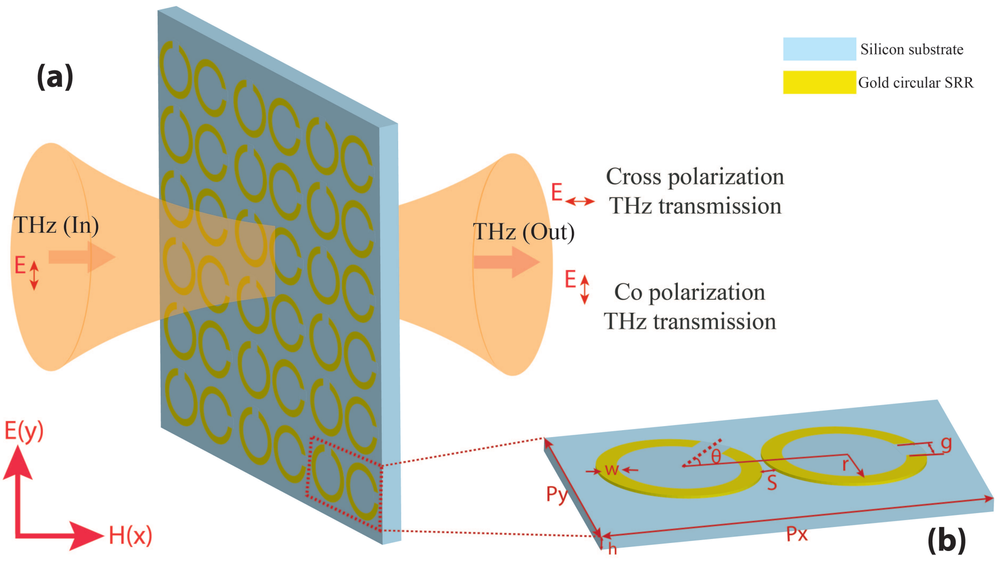

Figure 3.1: Schematic of a planar THz metamaterial geometry consisting of SRRs on silicon substrate. A single unit cell consists of two circular split ring resonators of gold metal. The yellow regions represent the metallic gold areas while gray region represents silicon substrate. Each of circular resonators has outer radius of 20 μm and inner radius r=16 μm. The w = 4 μm and g = 4 μm in the schematic stand for the line width and split gap of the resonators respectively. S (Separation between two resonators) = 1 μm and the parameter θ represents rotation angle, which can be varied from 0° to 180°. Figure 3.1(a) Schematic view of THz transmission through metamaterial sample. Figure 3.1(b) represents unit cell of metamaterial with varying rotation angles.

rotate the left side resonator from 0° to 90° and further 90° to 180°, in an anticlockwise fashion at an interval of 15° and observed co-polarization as well as cross polarization transmissions corresponding to various relative orientations (Figure 3.1).

3.2 Numerical simulation details

For our numerical study, we have employed commercially available numerical software, CST Microwave Studio and used tetrahedral meshing in order to accurately measure the response of geometry. We have used waveguide ports for the source and detector. In all simulations, plane wave excitation is used with normal incidence, containing modes linearly polarized in either x or y direction. Periodic boundary conditions are used to simulate an infinite two-dimensional periodic array, with unit cell and structural dimensions specified in Figure 3.1(b). The transmission results are normalized w.r.t. the transmission from a bare substrate and plotted in Figure 3.2. These plots represent transmissions,

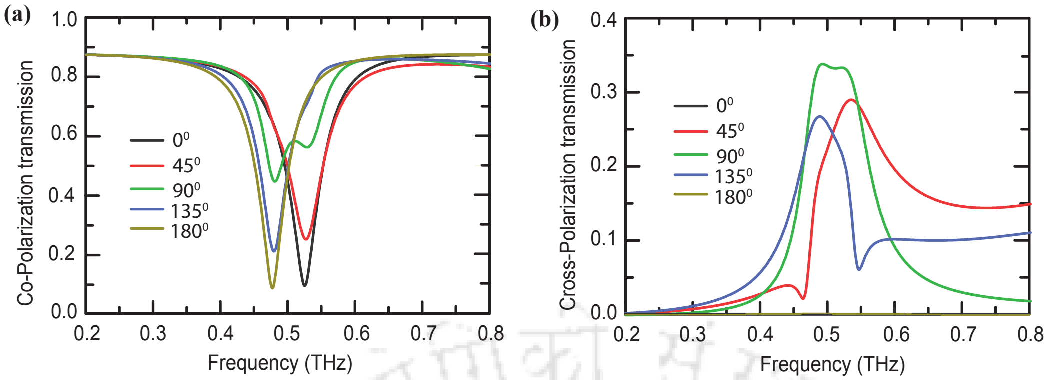

Figure 3.2: Numerically simulated (a) co-polarization and (b) cross-polarization transmission amplitudes of the proposed MM geometry for left SRR rotation from 0° to 180°.

T_{yy} and T_{xy} that contain both y- and x-polarization components, respectively, excited by the incident field linearly polarized in y direction. In this study, the polarization of the incident THz beam is assumed to be along the split gap of the right resonator in order to excite the fundamental LC resonance. The split resonances result from the coupling of right side split ring resonators with the left side resonators through a combination of magnetic and electric flux because of edge coupling of the twisted circular resonators [128,129]. The amplitude transmission shows a resonance split and results in maximum polarization conversion (Figure 3.2) due to a comparatively strong inductive coupling of the fundamental resonances of right and left circular resonators. The results of the terahertz transmission for both polarizations through inductively coupled THz metamaterial systems are discussed elaborately in the next section.

3.3 Results and discussions

In order to examine the terahertz co-and cross-polarization transmission properties of the near field coupled metamaterial responses, we rotate the LHS SRR with respect to the RHS SRR in the anticlockwise direction. The results are shown in Figure 3.2 and in Figure 3.3. In Figure 3.2(a), we plot the THz co- polarization transmission amplitude versus frequency and in Figure 3.2(b), we plot the THz cross-polarization transmission amplitude versus frequency for 0°, 45°, 90°, 135°, and 180°. At $\theta = 0°$, transmission shows single resonance at 0.5246 THz with cross polarization amplitude almost zero. As the relative SRR rotation is changed through the rotation angle from 0° to 15°, 30°, 45°, 60°,

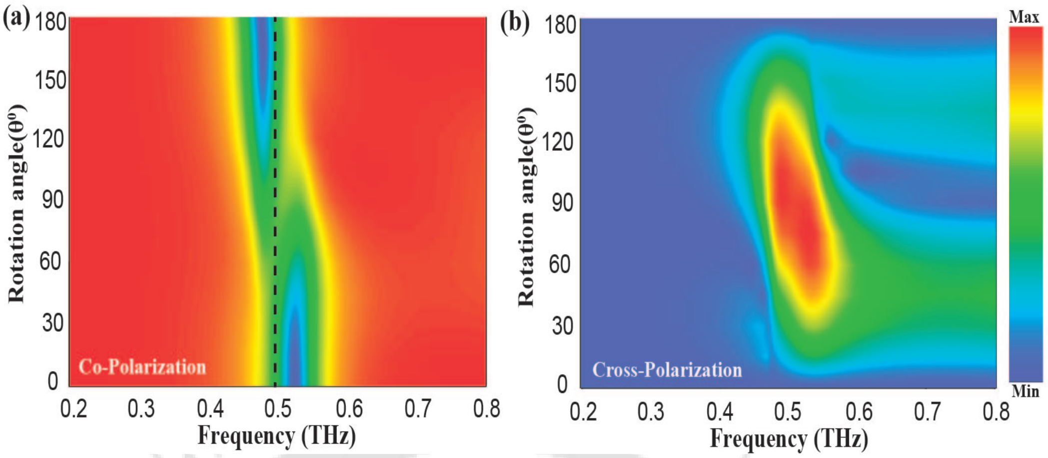

Figure 3.3: Comprehensive numerical simulation transmission amplitudes for θ varying from 0° to 180°. Contour plot for (a) co-polarization and (b) cross-polarization transmission amplitude for left SRR rotation from 0° to 180°.

75°, and 90°, we observed the gradual decrease in co-polarization transmission amplitude accompanied by a gradual increase in cross-polarization transmission amplitude. For θ less than 45°, the single resonance appears nearly at 0.5246 THz in co-polarization transmission and beyond θ = 45° till 90°, resonance split appears in co-polarization transmission with the lower resonance appearing near 0.4802 THz and the higher resonance at 0.5276 THz (see Figure 3.2(a)). At θ= 90°, clear resonance split takes place with resonance dips at 0.4922 THz and 0.5222 THz in cross-polarization transmission. At this configuration maximum polarization conversion is achieved with conversion amplitude as 0.33 (see Figure 3.2(b)). In this case, there is nearly 20% amplitude difference between co-and cross-polarization spectra. We have observed a reflection of nearly 20% from the metamaterial geometry. The rest of the field gets lost due to the scattering and diffraction. Further, LHS SRR is rotated with respect to RHS SRR from θ= 90° to 180°. For the range of θ= 90° till 120°, resonance split in co-polarization transmission amplitude exists with the lower resonance close to 0.4802 THz and higher frequency resonance close to 0.5276 THz. From θ = 135° to 180°, a single resonance dip occur at 0.4802 THz in co-polarization transmission. With the change in rotation angle from θ = 90° to 180°, a gradual increase in co-polarization transmission amplitude is observed along with a gradual decrease in cross-polarization transmission amplitude and finally at θ=180°, linear polarization rotation conversion reaches to zero. Further the intrinsic resonance of the SRR is observed at 0.4964 THz (Figure 3.3(a)). However, the split resonances are observed centering the intrinsic resonance. In order to understand the phenomenon

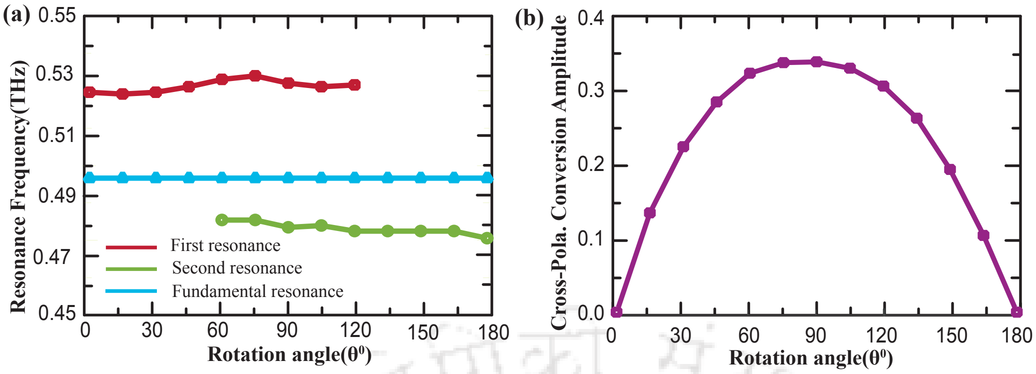

Figure 3.4: Resonance frequency vs rotation angle of left SRR from 0° to 180° for (a) co-polarization and (b) cross-polarization amplitude transmission.

behind the co and cross polarization transmissions elaborately, we have provided the qualitative analysis below. In our studied MMs, two circular split ring resonators are placed side by side to each other on silicon substrate. When the incident electric field is linearly polarized along the y-direction, the fundamental resonance mode of the right side SRR is always directly excited [130,131]. The incident electric field parallel to split gap creates circular current in right SRR with the accumulation of charges at the split gap (Figure 3.5). With $\theta = 0°$ bright mode in both the resonators are excited. However there is a strong inductive coupling changing the effective inductance of the resonators, therefore shifting the resonance from its intrinsic position (Figure 3.2). As the LHS resonator rotates (θ increasing), the LHS resonator slowly moves from bright regime ($\theta = 0°$) to dark regime ($\theta = 90°$). In case of $\theta = 90°$ the LHS is excited indirectly through the RHS bright resonator which is followed by inter resonator coupling to give rise to resonance mode splitting [128]. At this position the radiation of dark resonator is completely orthogonal to the incoming wave, hence we observe maximum magnitude of cross polarization. With further rotation ($\theta > 90°$), the LHS resonator gradually comes out of dark mode regime to bright regime. In the process the orthogonal polarization conversion diminishes and finally at $\theta = 180°$ both the resonators are excited directly through the incident electric field, hence no polarization conversion takes place. However the resonance dip appears at a different frequency than intrinsic case because of the effective inductance of the resonators. The induced circulating currents are in opposite direction resulting in different value of effective inductance.

For an elaborate understanding of co- and cross-polarization amplitudes, comprehensive simulation results are shown through contour plot (Figure 3.3). Figures 3.3(a) and

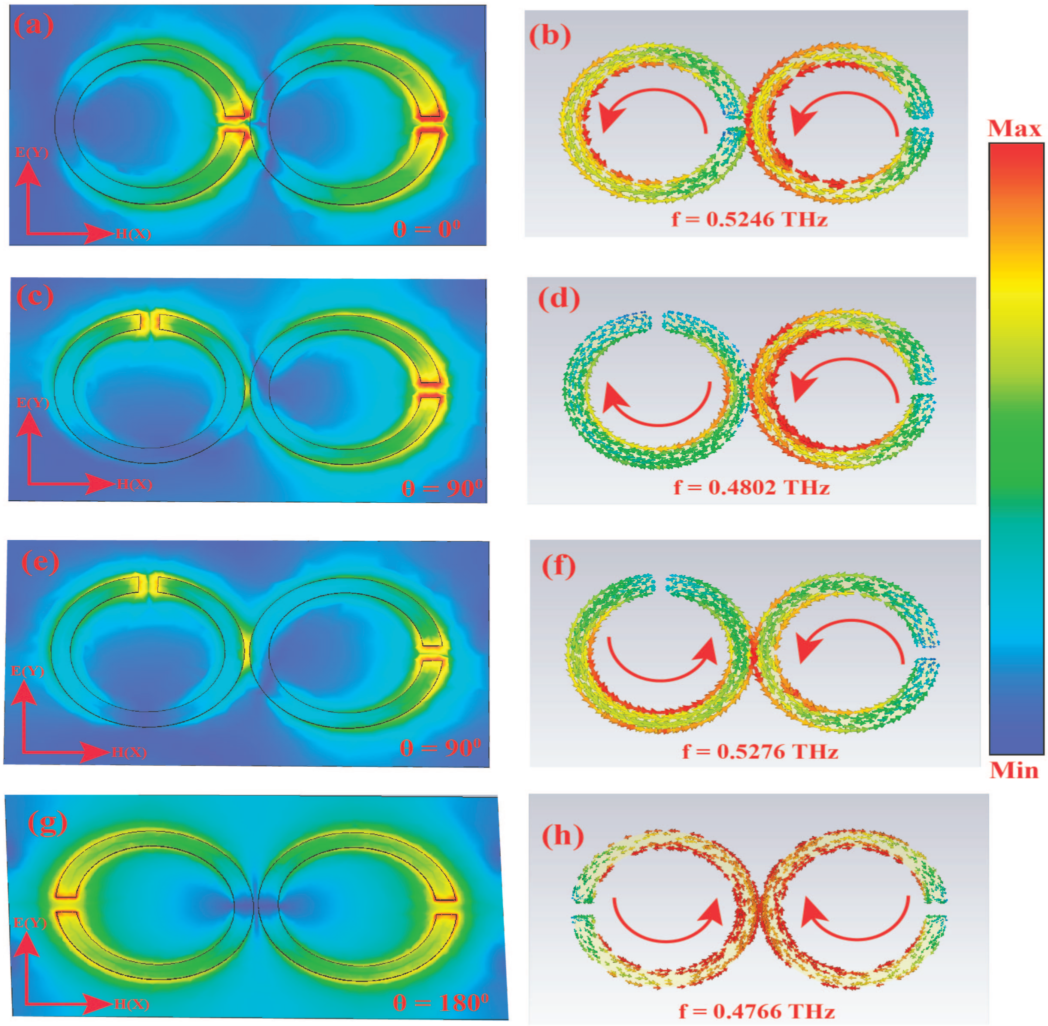

Figure 3.5: Simulated surface current and electric field profiles for 0°, 90°, and 180°. (a) & (b) represents the electric field and surface current profiles for 0° at 0.5246 THz. (c) & (d) represents the electric field and surface current profiles for 90° at the lower resonance frequency 0.4802 THz. (e) & (f) represents electric field and surface current profiles for 90° at the higher resonance frequency 0.5276 THz. (g) & (h) represents electric field and surface current profiles for 180° at resonance frequency 0.4766 THz.

(b) represents contour plots for co- and cross-polarization transmissions, respectively. In Figure 3.4(a), rotation angle is plotted against the resonance frequencies for the co-polarization transmission amplitudes. Blue line represents fundamental resonance of the intrinsic resonator, whereas the red and green lines represent the lower and higher order resonance frequencies for the coupled resonators, respectively. Figure 3.4(b) depicts the polarization conversion amplitude with rotation angle of the LHS resonator. With an increase in the rotation angle, cross polarization amplitude increases gradually till it reaches 90° where the linear polarization conversion attains maximum value. With further increase in θ, cross polarization decreases, and at 180° rotation angle, the cross polarization conversion amplitude reaches to zero. From our study, it is evident that the cross polarization conversion can be tuned from zero to maximum depending upon the relative orientation of the resonators.

We have further studied the electric field profiles and surface current profiles for 0°, 90° and 180° cases. The induced surface current and electric field distributions are shown in Figure 3.5 at the resonance dips. At 0.5246 THz for 0° case, the induced currents are in phase for both the resonators. This is the situation when both the resonators behave like the bright resonators. Electric field distribution depicts the bright mode excitation in both the resonators (Figures 3.5(a) and (b)). Surface current and electric field profiles for $\theta = 90°$ at lower and higher resonance modes are shown in Figure 3.5 (c), (d), (e) and (f), respectively. Figures 3.5(c) and (d) illustrates that the induced currents are out of phase whereas induced currents are in phase as revealed by Figures 3.5(e) and (f). In Figures 3.5(g) and (h), electric field distribution and surface current distribution are shown for 180° situation. However, the nature of induced currents are different in two resonators.

3.4 Theoretical model

In order to validate the co- and cross-polarization transmission results obtained through coupled metamaterials, we have employed a semi-analytical RLC circuit approach (Figure 3.6) [69,132]. This model has the ability to give us insight of the resonant co- and cross-polarization transmission behavior through the proposed coupled metamaterials system. In this semi-analytical approach, a single SRR is modeled with an equivalent RLC circuit which exhibits resonance at a specific frequency depending upon the shape and size of the split ring resonator. For our case, we assumed two RLC circuits with resistances, inductances and capacitances as Ω_1, L_1, C_1 and Ω_2, L_2, C_2 corresponding to the right

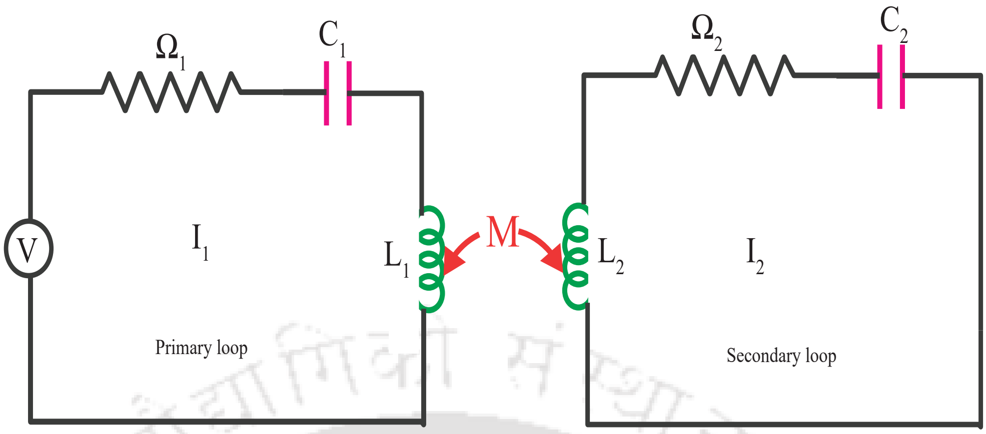

Figure 3.6: Schematic of the RLC circuit model. The electrical components Ω_1, L_1, C_1 represent the resistance, inductance, capacitance describing the fundamental LC resonance of the right meta-resonator and Ω_2, L_2, C_2 describe the resonance for the second left resonator. I_1 and I_2 represent the excited currents in right and left resonators respectively. The parameter M is responsible for the coupling between the resonators.

and left resonators, respectively (Figure 3.6). When incident electric filed ($E_{in} = \frac{V}{g}$, where V is voltage and g is the split gap of SRR) is linearly polarized along y direction, the fundamental resonance mode of only the right SRR is excited (because right SRR capacitive gap oriented along y direction). This is considered as a primary loop where circulating current is I_1. The fundamental mode of left SRR can not be excited due to its different orientation. So, left SRR will be excited because of right SRR through near field inductive coupling and the coupling parameter is mutual inductance (M). This is called a secondary loop and circulating current is I_2. Using Kirchhoffs voltage law, we can write equations for primary loop and secondary loop as below

$$[\Omega_1 + j\omega L_1 + \frac{1}{j\omega C_1}]I_1 + j\omega M I_2 = V \tag{3.1}$$

$$j\omega M I_1 + [\Omega_2 + j\omega L_2 + \frac{1}{j\omega C_2}]I_2 = 0 \tag{3.2}$$

Using Cramer's rule, if you solve $I_1$and I_2

$$I_1 = \frac{V[\Omega_2 + j\omega L_2 + \frac{1}{j\omega C_2}]}{[\Omega_1 + j\omega L_1 + \frac{1}{j\omega C_1}][\Omega_2 + j\omega L_2 + \frac{1}{j\omega C_2}] - \omega^2 M^2 j^2} \tag{3.3}$$

$$I_2 = \frac{V j\omega M}{[\Omega_1 + j\omega L_1 + \frac{1}{j\omega C_1}][\Omega_2 + j\omega L_2 + \frac{1}{j\omega C_2}] - \omega^2 M^2 j^2} \tag{3.4}$$

Where j is the imaginary unit and ω is the angular frequency of the incident electromagnetic waves. The induced electric dipoles are proportional to the charge accumulation at the split gaps, i.e. $P_{1,2}$ is proportional to $\int I_{1,2}dt$. From above analysis, we know I_1 is responsible for co-polarization and I_2 is responsible for cross-polarization transmission. Now from I_1 and I_2, we can derive total impedance for co and cross polarization transmissions. We know $Z = \frac{V}{I}$, then $Z_{co} = \frac{V}{I_1}$ and $Z_{cross} = \frac{V}{I_2}$ now we can write total impedance for co- and cross-polarization transmissions.

$$Z_{cross} = \frac{Z_1Z_2 - (Z_m)^2}{Z_m} \tag{3.5}$$

$$Z_{co} = \frac{Z_1Z_2 - (Z_m)^2}{Z_2} \tag{3.6}$$

where

$$Z_1 = \Omega_1 + j\omega L_1 + \frac{1}{j\omega C_1} \tag{3.7}$$

$$Z_2 = \Omega_2 + j\omega L_2 + \frac{1}{j\omega C_2} \tag{3.8}$$

$$Z_m = j\omega M \tag{3.9}$$

Normalized transmission formula for co and cross polarization is

$$t(\omega) = \frac{Z_{total}(Z_s + Z_0)}{Z_s(Z_{total} + Z_0) + (Z_{total}Z_0)} \tag{3.10}$$

Where, Z_s(impedance of Si substrate) = 103 Ω and Z_0(impedance of free space) = 377 Ω.

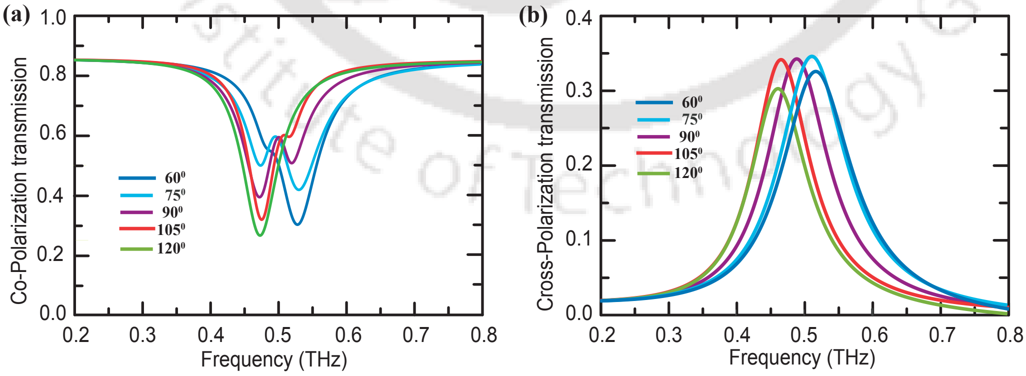

Figure 3.7: Terahertz amplitude transmission through the coupled resonators in planar THz metamaterials obtained from RLC circuit model for various rotations of left split ring resonator w.r.t right SRR. The results affirm numerical observations. (a) Co-polarization transmission. (b) Cross-Polarization transmission.

Rotation angle (θ)	Ω_1 (ohm)	L_1 (pH)	C_1 (fF)	Ω_2 (ohm)	L_2 (pH)	C_2 (fF)	M (pH)
60°	35	245	0.38	34	165	0.64	12
75°	52	245	0.4	32	165	0.63	19
90°	52	282	0.38	32	200	0.5	20
105°	40	342	0.32	32	194	0.5	14
120°	35	282	0.4	32	180	0.2	12

Table 3.1: Ω, L, C and M values for Co-Polarization transmission.

Rotation angle (θ)	Ω_1 (ohm)	L_1 (pH)	C_1 (fF)	Ω_2 (ohm)	L_2 (pH)	C_2 (fF)	M (pH)
60°	250	145	0.4	312	125	0.2	179
75°	250	125	0.4	312	125	0.2	205
90°	250	141	0.4	312	125	0.2	224
105°	250	156	0.4	312	125	0.22	220
120°	250	205	0.4	312	125	0.2	210

Table 3.2: Ω, L, C and M values for Cross-Polarization transmission.

We have used equation 3.10 to get co- and cross-polarization transmission results. For co-polarization transmission results, we have substituted equation 3.6 in place of Z_{tot} into equation 3.10 and varies Ω, L, C and M values. At particular values of Ω, L, C and M, we calculated co-polarization transmission plots (See Table 3.1 for Ω, L, C and M values). The results of amplitude transmission through RLC-circuit model for co-polarization are shown in Figure 3. 7(a). The corresponding values of coupling parameter M are given in table-3.1. We observe increase in M value with an increase in rotation angle of left SRR from 60° to 90° and from 90° to 120° M value got decreased. The calculated amplitude transmission is found in good agreement with the numerical simulations. Next, for cross-polarization transmission results, equation 3.5 is substituted in place of Z_{tot} in equation 3.10. Using final transmission (equation 3.10) expression and at particular Ω, L, C and M values (See Table 3.2), we calculated the cross polarization transmissions. These results too match well with our numerical simulations (shown in Figure 3.7(b)). Mutual inductance (M) values (Table 3.1 and Table 3.2) for both the co- and cross-polarizations cases show a certain trend i.e. till 90° it increases and beyond 90° till 120° it decreases gradually. From this, we can conclude that at 90° mutual inductance attains highest value. Since mutual inductance M represents coupling strength, this indicates that at 90° , the resonators are maximally coupled through mutual inductance. Beyond this point, if left SRR is rotated in anti-clockwise fashion with respect to the right SRR, the coupling strength decreases as can be confirmed from mutual inductance values.

3.5 Discussions

To summarize, we have presented a gradual linear polarization converter with a double split ring resonator based metamaterials system operating in the terahertz regime without changing the metamolecule unit cell size. We have tuned cross-polarization and co-polarization transmissions by changing the relative rotation angle of one resonator with respect to the other from 0° to 180°. We have demonstrated that the cross- polarization transmission amplitude gradually changes from zero to maximum and then back to zero. At the same time, the co-polarization transmission amplitude varies from single resonance dip to split resonance dips and then back to single resonance dip. With the rotation angle at 90°, the maximum cross polarization conversion is achieved. When the left side circular resonator split gap rotation angles are close to θ=0° or 180°, minimum cross polarization conversion is achieved along with a single resonance in co polarization transmission because of the absence of mode hybridization where resonators behave close to the intrinsic resonators. We have monitored electric field and surface current profiles to confirm our observations. Further an RLC theoretical model is employed to validate the coupling mechanisms in details. We considered the circular SRRs as lumped element RLC resonant circuits and calculated the induced currents within the circular SRR loops. Finally, we calculated the co and cross polarization transmissions. Our theoretical outcomes are in good agreement with our numerical results. The present work for our studied near field coupled metamaterials boosts the understanding of near field resonator coupling within the composite metamolecules, which can lead to realization of polarization manipulation devices in terahertz regime.

CHAPTER

4

ULTRA-WIDEBAND EFFICIENT POLARIZATION CONVERSION OF TERAHERTZ WAVE

In the previous chapter, we have demonstrated cross-polarization conversion of incident terahertz radiation by changing the orientation of one resonator with respect to the other in a planar coupled MM geometry. It is observed that the polarization conversion could be achieved in a narrow band of frequencies. However, the terahertz polarization conversion devices over a broader spectrum can be significant for the broadband terahertz photonics applications. Traditional approaches such as birefringence crystals, total internal reflections, Faraday Effect, optically active materials lead to less efficient polarization conversion that also in a narrow band spectrum [133-135]. Recently it had been shown that polarization conversion in these approaches can be enhanced significantly using MM structures [40-42]. Realization of broadband polarization conversion is a challenging task in terahertz and has piqued the curiosity of many researchers working in this domain. Several efforts have been made to achieve broadband polarization conversion of linearly polarized light into the circular one, and the left circularly polarized light to right one and vice-versa using chiral MMs [50-51,136-137]. The anisotropic MMs have been used to study the broadband polarization conversion of a linearly polarized light in the reflection/transmission modes [43-46,138]. Numerous multilayer structures and graphene-based metallic structures were also investigated to achieve passive and

---

Part of the results of this chapter is accepted for publication in Journal of Physics D: Applied Physics dynamic control of broadband cross-polarization conversion [60-62,139]. However, the fabrication process of such multilayered and 3D MM geometries are challenging. Therefore, flexible and simple approaches are required to be investigated to achieve broadband terahertz efficient polarization conversion.

In this chapter, an effort has been made to address this challenge by exploring the broadband polarization conversion possibility using a planar MM configuration. We investigate a planar MM comprised of a C-shaped resonator numerically and experimentally to achieve ultra-wideband efficient cross-polarization conversion of the incident terahertz wave. We have rotated the MM geometry with respect to the incident THz to examine the suggested MM configuration's capacity to convert polarization. The polarization conversion in our proposed geometry occurs due to the excitation of induced electric dipole which radiates fields both in the co- and cross-polarizations. It is observed that the change in dimensions of the resonator causes a shift of the transmission spectrum.The subsequent sections discuss the design, experimental results and shift of the transmission spectrum in detail.

4.1 Metamaterial design for broadband polarization conversion

The suggested MM structure's unit cell, shown in Figure 4.1(a), is a C-shaped resonator with a single split gap. The resonators are designed on a quartz wafer with a permittivity of $\epsilon_r = 4.42$ and a thickness of $t = 500\ \mu m$. The periodicity of the substrate is denoted by the letter P, which is set to $P = 40\ \mu m$. The resonators are composed of gold with a thickness of 200 nm and an electrical conductivity of $\sigma = 4.56 \times 10^7 Sm^{-1}$. The length of the C-shaped resonator is $L = 30\ \mu m$. "w" denotes the width of the C resonator, which is 5 μm in this case. The resonator's split gap is represented by "g" and is equal to 20 μm. Figure 4.1(b) shows the microscopic image of the fabricated sample. The incident electric field is directed along the resonator's split gap, as indicated by the green arrow. The angle of rotation of the geometry with respect to the incident light is indicated by θ. We used CST microwave studio to perform numerical simulations of the MM structures in our research. In the x-y plane, we employed unit cell boundary conditions.

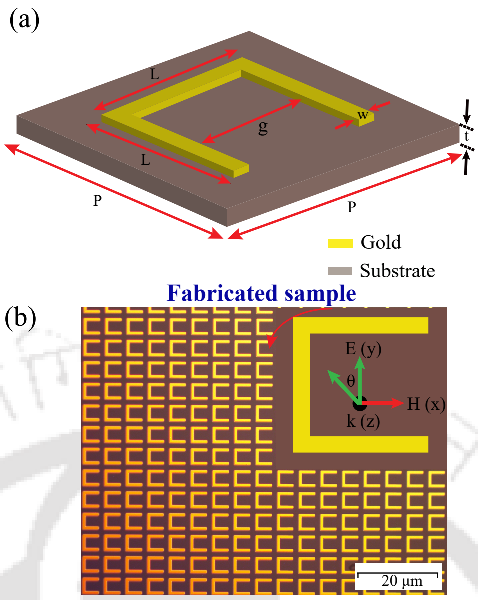

Figure 4.1: (a) The unit cell of the MM geometry consisting of a C shaped resonator. P denotes the periodicity. L is the length, w is the width and g is the split gap. (b) Microscopic image of the fabricated sample.

4.2 Results and discussions

We have studied numerically co- and cross-polarization spectrum of the proposed MM geometry by changing θ from 0° to 45°. The results are shown in Figures 4.2(a) and 4.2(b) respectively. For the y-polarized incident light i.e. θ=0°, in the co-polarization transmission spectrum two distinct resonances: one at 1.17 THz and the other at 2.91 THz can be noticed. The corresponding transmission spectrum is illustrated by the black traces. As θ increases the co-polarization transmission amplitude reduces for the 1st order resonance. The transmission spectrum for θ=15° and θ=30° are depicted by red and green traces respectively in Figure 4.2(a). The co-polarization transmission amplitude reduces to 0.5 for θ=45° for the 1st order resonance and is illustrated by the blue traces. However, the transmission amplitude for the 3rd order resonance almost remains constant for θ=0° to 45°. For θ=0° the cross polarization amplitude is zero which can be observed from the black traces of Figure 4.2(b). The amplitude of cross-polarization transmission increases as θ increases. From the red traces, a cross-polarization amplitude of 0.20 can be observed from 1.22 THz to 2.77 THz with a maximum amplitude of 0.22 at 1.39 THz for θ=15°. For θ=30°, a cross-polarization amplitude of 0.34 is obtained from 1.22 THz to 2.81 THz with a maximum amplitude of 0.39 at 1.22 THz. The corresponding spectrum is shown by the green traces. Further, when the rotation angle increases to θ=45° an amplitude of 0.4 is achieved from 1.22 THz to 2.76 THz THz with a maximum amplitude of 0.45 at 1.39 THz as shown by the blue traces.

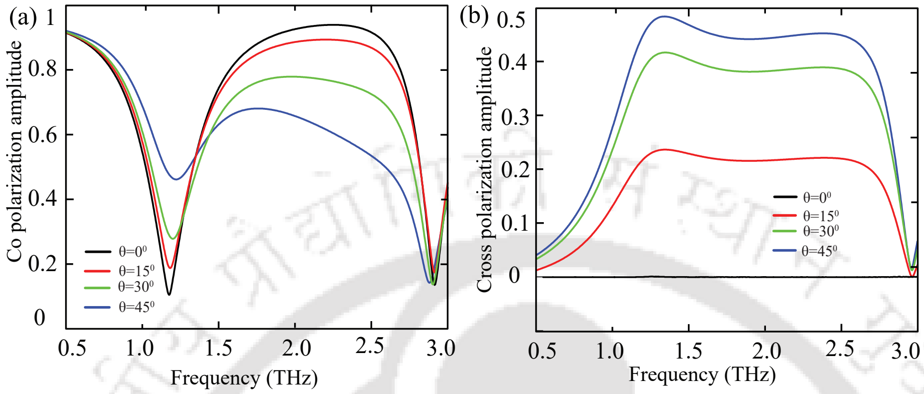

Figure 4.2: Numerically simulated (a) co- and (b) cross-polarization transmission spectra of the proposed geometry for θ=0° to 45°.

To get a comprehensive understanding of change of co- and cross-polarization transmission amplitudes with the rotation angle, we have illustrated contour plots for different angles of rotation for θ=0° to 90°. We have shown the contour plots in Figures 4.3(a) and 4.3(b) respectively. The rotation angles are represented on the y-axis, while the frequency is plotted on the x-axis. The strength of transmission amplitudes is shown by the color bar. The change of transmission amplitude of 1st order resonance is apparent from Figure 4.3(a). While the amplitude of 3rd order resonance almost remains constant and the resonance gets slightly red shifted with increase in θ. Cross- polarization conversion for rotation angles θ=15°, 30° and 45° in a wide frequency range are also visible in figure 4.3(b). Further, it can be noted that for $\theta > 45°$, the strength of both co-and cross-polarization amplitudes reduces and become zero for θ=90°. Because the incident electric field is perpendicular to the split-gap of the C-resonator in this scenario, it is unable to excite the resonator and hence it behaves as a dark mode. Figure 4.4 shows the induced electric field and surface current profiles at the 1st transmission dip for various rotation angles of incident light to better understand the polarization conversion mechanism in our suggested MM design. For θ=0°, strength of the electric field at the split gap is maximum and circular current flows in the clockwise direction which is clear from Figures 4.4(a) and 4.4(d). This clearly indicates that the 1st order resonance is the LC resonance. In this case, due to the charge separations, an electric dipole will be induced

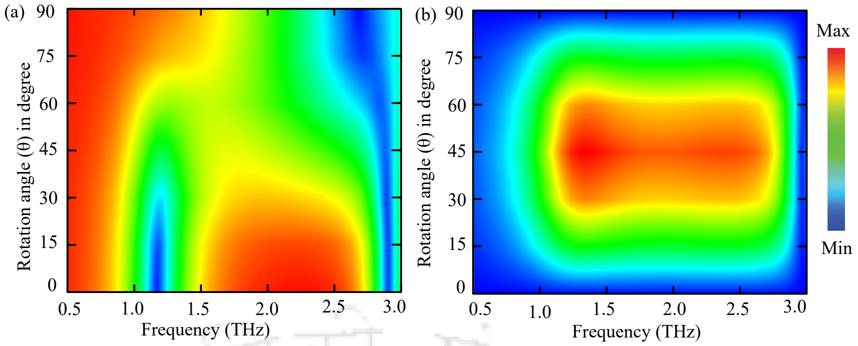

Figure 4.3: Numerically simulated contour profiles for (a) co- and (b) cross-polarization transmission amplitude for different rotation angles θ=0° to 90°. Here the color bar indicates the strength of the amplitude.

along the split gap, which will radiate field only along the y-direction. As a result, co-polarization transmission strength will be maximum and cross-polarization amplitude will be zero. For $\theta > 0°$, an induced electric dipole will have both x-and y-components. This x-component of induced dipole results in non-zero cross-polarization conversion. Further, when θ increases to 45°, the confinement of electric field and strength of the flow of circular current reduces which can be understood from Figures 4.4(b) and 4.4(e). Here,

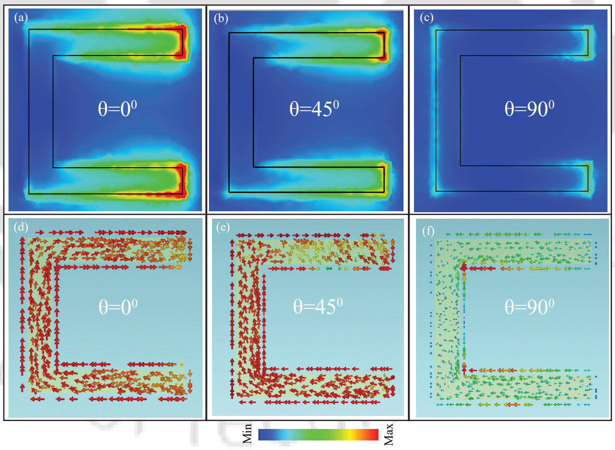

Figure 4.4: (a)-(c) Induced electric field profiles and (d)-(f) surface current distributions for rotation angles θ=0°, 45° and 90°.

the x-component of induced electric dipole causes a maximum cross-polarization conversion. It may be noted that beyond 45° although the projection of induced dipole along the x-direction increases but strength of the resonance reduces. This causes reduction of amplitudes of both co-and cross-polarization transmission spectra. From Figures 4.4(c) and 4.4(f) it can be visualized that, for θ=90°, the electric field confinement at the gap of resonator almost becomes zero and the circular flow of current vanishes completely. This results in zero co-and cross-polarization amplitudes.

4.3 Experimental details and results

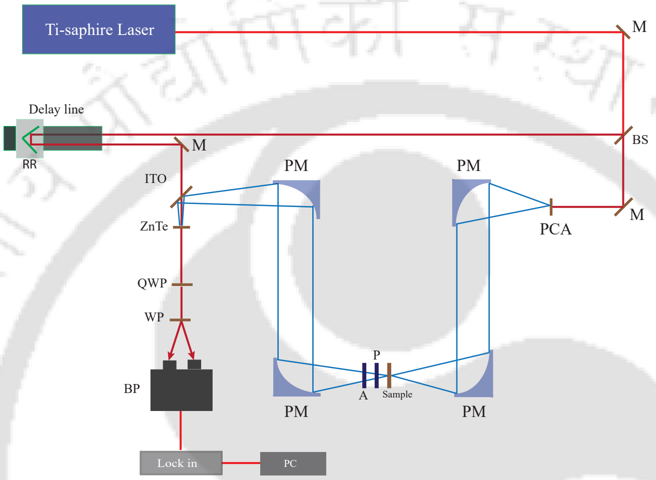

Figure 4.5: Schematic diagram of Terahertz Time Domain State of Polarization Measurement setup. M-Mirror, BS-Beam Splitter, PCA-Photoconducting Antenna, PM-Parabolic Mirror, RR-Retro Reflector, ITO-Indium Tin Oxide, ZnTe-Zinc Telluride, QWP-Quarter Wave Plate, WP-Wollaston Prism, BP-Balanced Photodetector, P-Polarizer, A-Analyzer.

We have fabricated the MM samples using the standard EBL technique. We have shown the micrographic photographs of the sample in Figure 4.1(b). We employed a THz-TDS setup (shown in Figure 4.5) to measure the transmission spectra of the prepared samples. Here in one part of the beam, we have generated linearly polarized THz using LT-GaAs based Photoconductive Antenna (BATOP GmBH), and another part of the beam is used for the detection of the THz by electro-optical sampling using a ZnTe single crystal of thickness 2 mm and orientation 110.

The MM is aligned at the focus of the parabolic mirror with polarizer (P) and analyzer (A) in the path. The entire THz setup is purged with nitrogen to suppress water absorption artefacts present in the ambient air. To measure the State of Polarization (SoP) of the sample, the analyzer (A) is aligned to the incident THz electric field and the MM is positioned at an angle where the SoP is to be measured and say β is the angle subtended by the polarizer (P) w.r.t analyzer (A). The resulting projection of electric field

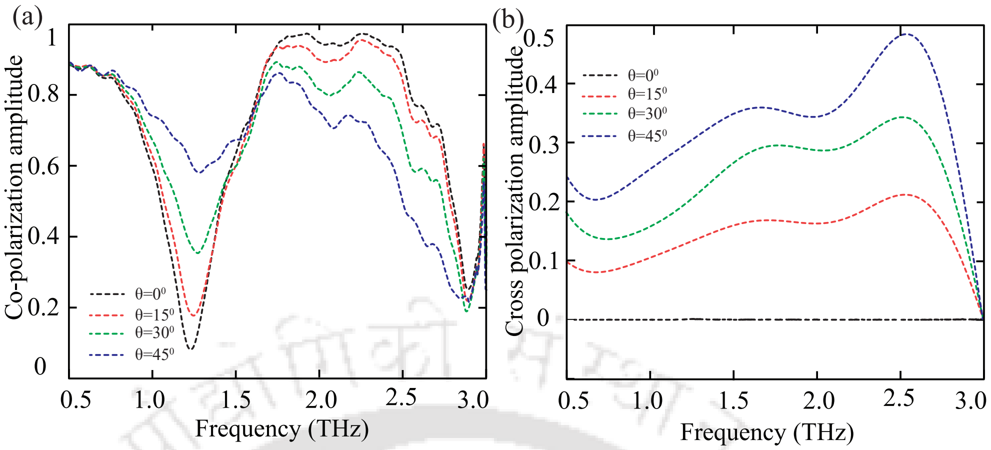

Figure 4.6: Experimentally measured (a) co-and (b) cross-polarization transmission spectrum for different angles of rotation.

amplitude on the detector can be obtained as [140]

$$S(\beta) = \cos\beta[(a_1 cos\beta + a_2 sin\beta cos\delta)^2 + (a_2 sin\beta sin\delta)^2]^{\frac{1}{2}} \tag{4.1}$$

where a_1 and a_2 are the amplitudes of co- and cross-polarization transmissions, δ is the phase lag between these two components where δ=0° is the linear polarization and δ=90° is the circular polarization. THz spectra are recorded at every position of polarizer (P), which is rotated from 0° to 360° with a step size of 10°. The frequency-domain data of the 36 scans are fitted to the above equation for every single frequency to obtain frequency-dependent co- and cross-polarization of the MM. The fitting is done in python using the SciPy curve fitting library. We have illustrated the experimentally measured co- and cross-polarization transmission spectrum for θ=0° to 45° in Figures 4.6(a) and 4.6(b) respectively. From the black dotted line of Figure 4.6(a), it can be seen that for θ=0° there are two resonance dips. In this case, cross-polarization transmission amplitude is zero throughout the entire spectrum. Here incident electric field couples with the C resonator and 1st order LC and 3rd order dipolar resonances are excited in it. In addition, an electric dipole in parallel to the incident E-filed i.e. along the y-axis will be induced. As a result, there is no component of electric dipole in the horizontal direction that can radiate field, which results in a zero cross-polarization transmission amplitude. For θ=15°, the amplitude of LC resonance reduces. As θ further increases to 30° and 45° the amplitude of 1st order transmission dips reduces more. The co-polarization transmission spectrum for θ=30° and θ=45° are illustrated by blue and magenta traces. From Figure 4.6(b) it can be noted that a broadband cross polarization conversion occurs for θ=15°, θ=30° and θ=45°.

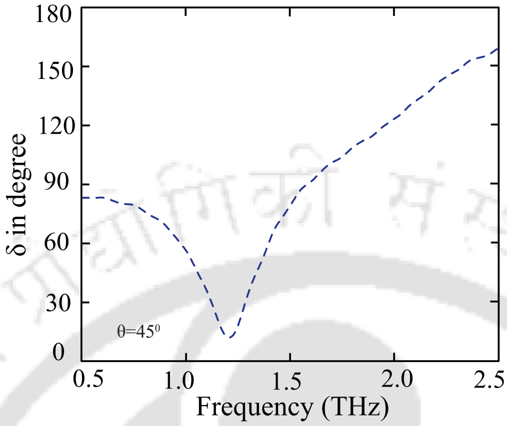

Figure 4.7: Experimentally measured phase lag between the co-and cross-polarization components of the transmitted light for 45° angle of rotation.

We experimentally analyzed the phase difference (δ) between the two orthogonal components for θ=45° of the transmitted wave in order to learn more about its polarization state. The result is shown by the blue traces in Figure 4.7.

Further, we have calculated polarization rotation azimuth angle ϕ and ellipticity η using the following equations [141].

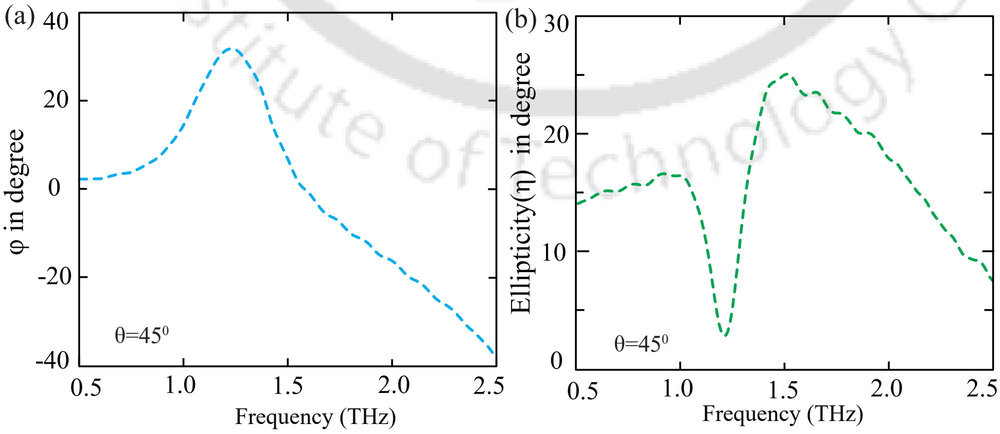

Figure 4.8: (a) Angle of polarization rotation azimuth (ϕ) in degree and (b) ellipticity (η) for rotation angle of θ=45°.

$$\begin{aligned} \phi &= \frac{1}{2}arctan(\frac{2Rcos\delta}{1-R^2}) \\ \eta &= \frac{1}{2}arcsin(\frac{2Rsin\delta}{1+R^2}) \end{aligned} \tag{4.2}$$

The ratio of cross- and co-polarization amplitudes is R in this case. The polarization rotation azimuth angle denotes the angle at which transmitted light rotates in relation to incident light. Figures 4.8(a) and 4.8(b) show the experimentally measured ϕ and η, respectively. The polarization state of the transmitted light is described in terms of ellipticity. $\eta = 0°$ corresponds to linearly polarized light. $\eta = 45°$ corresponds to right-handed circularly polarized light and $\eta = -45°$ represents left-handed circularly polarized light. On the other hand $-45° < \eta < 0°$ indicates left-handed elliptically polarized light and $0° < \eta < 45°$ gives right-handed elliptically polarized light. From figure 9(b), it can be noted that the ellipticity value is always positive. This indicates that the light transmitted from our proposed geometry is always right-handed elliptically polarized. At the 1st order resonance, $\eta = 5°$ and $\phi = 25°$, indicate that the transmitted light is right-handed elliptical and rotated by 25° after transmitting through the MM geometry at 1.17 THz. In our case, the highest value of ϕ is $-39°$ at 2.50 THz. Therefore, our design rotates the incident light by a maximum of $-39°$ at 2.50 THz.

4.4 Frequency shift of the transmission spectrum

Further, the shift of the co-polarization transmission spectrum for θ=45° is investigated by varying the length of the C-resonator. Experimentally measured and numerically simulated transmission spectrum for various lengths are depicted by dash and solid traces in Figures 4.9(a) and 4.9(b) respectively. However, there is little mismatch between the simulated and experimental results. The disagreement may occur due to the fabrication error and due to the lower spectral resolution of the measurement, which is limited by the Fabry-Perot reflection pulse from the rear surface of the substrate. Further experimental optimizations may improve the results. The black traces illustrates that for $L = 30\ \mu m$ the resonance dip occurs at 1.29 THz. It can be noticed that when the length of the C-resonator is reduced to 26 μm and 20 μm, the reonace dip gets blue shifted to 1.5 THz and 2.0 THz respectively. The results are shown by red and green traces. As the length of the C-resonator decreases the effective inducance and capacitance reduces

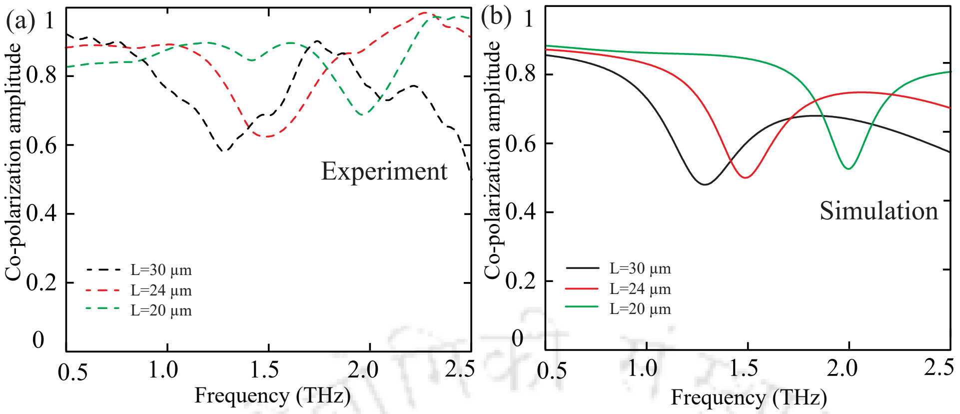

Figure 4.9: Experimentally measured and numerically simulated co-polarization transmission spectra of the MM geometry for $L = 30\ \mu m$, $L = 24\ \mu m$ and $L = 20\ \mu m$ with θ=45°.

which causes blue shift of the transmission spectrum. These results clearly demonstrate that our proposed design can be used as a polarization converter in the terahertz as well as it can be scaled and used in other frequency regimes.

4.5 Discussions

A planar MM geometry comprised of C-shaped resonator is used to illustrate an ultra-wideband efficient polarization converter numerically and experimentally. For varied rotation angles of the geometry w.r.t. the incident broadband THz, we investigated co- and cross-polarization amplitudes of the suggested MM configuration. In a frequency spectrum ranging from 1.22 THz to 2.75 THz, the polarization converter shows a 40% cross-polarization conversion. The induced electric field profiles and surface current distributions have been used to further investigate the polarization conversion mechanism. This indicates that the gradual decrease of the electric field confinement at the split gap of the C-resonator causes weaker co-polarization transmission associated with the maximum cross-polarization transmission for a rotation angle of 45°. Furthermore, modifying the length of the C-resonator we have shown the blue shift of the transmission spectrum. Unlike previously used multilayered structures, our proposed design can easily be fabricated which eliminates complicated manufacturing processes. The proposed design could be highly useful in the development of broadband THz photonic devices.

CHAPTER 5

POLARIZATION INDEPENDENT DUAL-BAND EIT EFFECT

As discussed in chapter one electromagnetically induced transparency in metamaterials has garnered a lot of attraction in the scientific community over the past decade owing to its numerous applications in the field of sensing, slow light, filters and modulators [77-86]. One advantage of studying EIT in metamaterials is the fact that the effect can occur even at room temperature. This led to considerable interest in exploring the dual-band EIT effect through careful optimization of structural parameters of MMs. In this effect, two transparency windows are induced due to the coupling between bright-dark-dark or bright-bright-dark modes of the constituent MM structures. In the microwave frequency regime, the dual-band EIT effect has been reported in a planar MM composed of two metal wires and a double SRR [142]. In the terahertz frequency regime, three meta-atoms acting as the bright, dark and quasi dark modes have been shown to exhibit the dual-band EIT effect [114]. Devi et al. have investigated the dual-band EIT effect in a terahertz MM composed of inner circular and outer asymmetric two-gap circular split-ring resonators [143]. Amin et al. demonstrated electromagnetically induced transparency and slow-wave application in the multi-band spectrum in a guided wave resonator based on microstrip lines in the gigahertz frequency regime [144]. Further, Tang et al. reported modulation of dual-band EIT effect in a planar terahertz MM comprising of a closed ring resonator

---

Part of the results of this chapter have been published in the following paper: Polarization independent double-band electromagnetically induced transparency effect in terahertz metamaterials R Sarkar, KM Devi, D Ghindani, SS Prabhu, D R Chowdhury, G Kumar - Journal of Optics 22(3), 035105, 2020.

and a square patch [146]. The dual-band EIT effect has potential applications in the field of ultrasensitive sensing [142,146], spectral filtering applications [145], slow-light systems [115,147] and communications. It has been noticed that the dual-band EIT effect reported so far, is sensitive to a particular polarization of the incident light. As the excitation of the bright mode strongly depends upon the polarization of the incident light, therefore a change in the polarization of the incident light would significantly affect the excitation of the bright mode and hence the dual-band EIT effect will either diminish or completely vanish. To make practical devices for applications in ultra-sensitive sensing and slow light effect, it is very important to design the dual-band EIT MMs that have a polarization-independent response. Although polarization-independent dual-band EIT MM has been reported very recently in the gigahertz frequency regime, [148] however none of the studies on dual-band EIT phenomenon in terahertz metamaterials has reported polarization-independent effect to the best of our knowledge.

In this chapter, we have experimentally and numerically examined a MM structure composed of a strip and two asymmetric SRRs for their ability to exhibit a dual-band EIT effect in the terahertz frequency regime. The dual-band EIT effect that occurs in our meta-molecule is achieved because of the near field coupling between the bright mode of the strip and dark modes resulting from two SRRs. Further, we have also examined the polarization-independent response with respect to the two orthogonal polarizations of the incident light, by augmenting the metamolecule with two more asymmetric SRRs in the perpendicular orientation. The transmission response has also been investigated for different angles of incidence of the two orthogonal polarizations of incident light. Further, sensing application of the dual-band transparency windows has been reported. A theoretical model based upon a four-level tripod (FLT)- system is employed to explain the mechanism of the dual-band EIT effect of the proposed MM configuration. The design and experimental details of the MM structure, polarization-insensitive response, refractive index sensing application and analytical modeling are discussed in different sections followed by a brief summary and discussion.

5.1 Metamaterial design and experimental details

The schematic illustration along with the unit cell of the MM structure comprising of the strip and two SRRs are depicted in Figure 5.1(a). The strip and two SRRs are made up of $t = 200\ nm$ thick gold. The strip placed at the center has length, $L = 88\ \mu m$ and width,

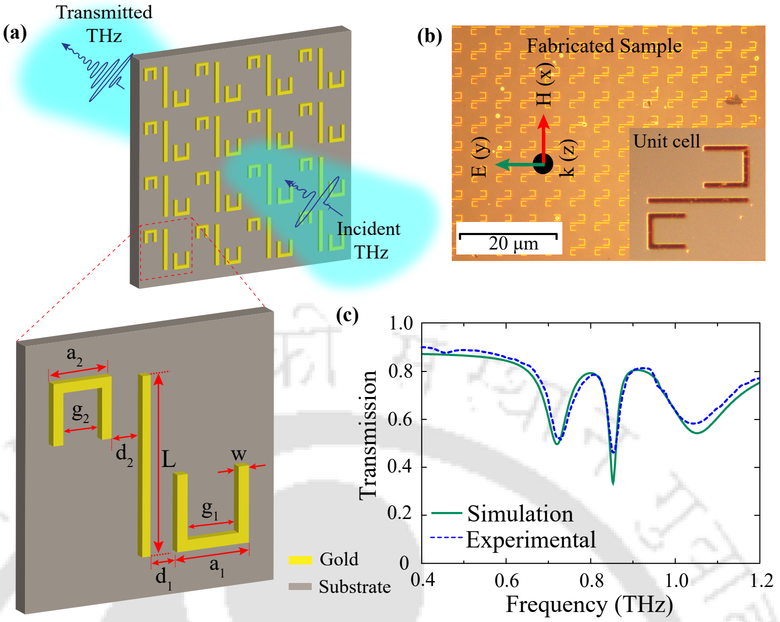

Figure 5.1: (a) The unit cell of the proposed metamaterial structure composed of a strip and two asymmetric SRRs and schematic illustrating transmission of terahertz light through the proposed metamaterial geometry. (b) Shows optical micrograph image of the fabricated sample along with the unit cell. (c) Depicts plot of the experimentally and numerically calculated terahertz transmission spectra of the proposed MM configuration for the y-polarized incident light. Solid lines represent the simulated, while dotted line corresponds to the measured transmission spectra.

$w = 4\ \mu m$. Both the two SRRs have same width, $w = 4\ \mu m$ but different dimensions to exhibit the dual-band EIT response. The left SRR has dimensions, $a_2 = 34\ \mu m$ and gap $g_2 = 26\ \mu m$. On the other hand, the right SRR has dimensions, $a_1 = 40\ \mu m$ and gap $g_1 = 32\ \mu m$. The MM structures are designed on a substrate having dielectric permittivity of 4.686 and periodicity, $P = 144\ \mu m$ and thickness, $h = 500\ \mu m$. We have used standard electron beam lithography technique for the fabrication of the gold SRRS on top of the milky quartz substrate having permittivity of 4.686 in the clean room environment. Optical micrograph image of the fabricated sample along with the unit cell is depicted in Figure 5.1(b). In order to measure the spectral response of the MM samples, we have used commercially available terahertz Toptica system (Terahertz frequency domain spectroscopy) that has high frequency resolution of 2 MHz. Detail description of the setup is already given in chapter 2. In order to numerically investigate the transmission response of the MM structures we have used commercially available simulation software named CST Microwave Studio. To figure out the evolution of the

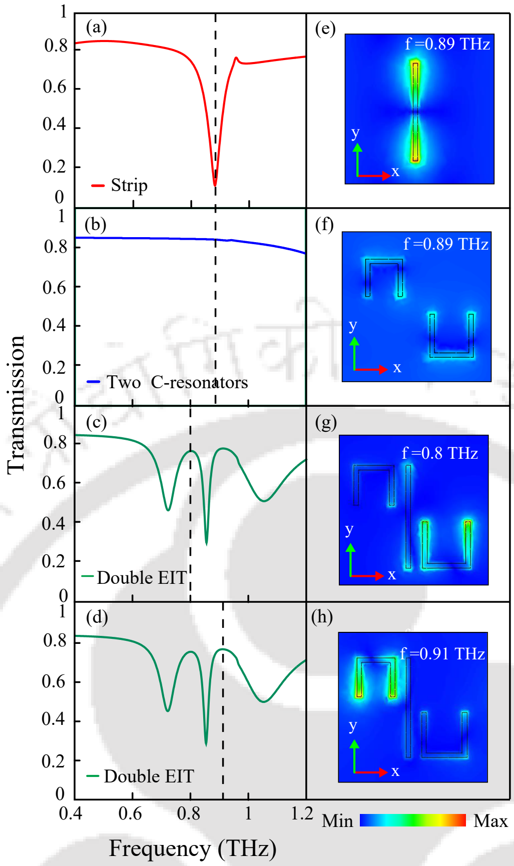

Figure 5.2: Terahertz transmission through the strip (a), the two asymmetric DCRs (b), the proposed MM configuration ((c) and (d)). (e) and (h) Shows electric field profiles for the strip (at 0.89 THz), two asymmetric SRRs (at 0.89 THz), transmission peak 1 (at 0.8 THz) and peak 2 (at 0.91 THz), respectively. (Polarization direction of the incident electric field is represented by green arrow).

dual-band EIT effect and the coupling mechanism involved in it, we have independently examined the transmission spectrum of the strip, two SRRs and the combined structure. We have also examined the induced electric field profiles for the corresponding geometries. The numerically simulated transmission profiles and the induced electric field profiles are depicted in Figure 5.2. The green arrow in the figure indicates the direction of the electric field of the incident light. The strip exhibits a dipole resonance at 0.89 THz which is indicated by the red traces in Figure 5.2(a). It is evident from the figure that the strip couples strongly with the electric field of the incident terahertz light and hence acts as a bright mode. The corresponding induced electric field profile of the strip at the resonance frequency, shown in Figure 5.2(e), indicates a strongly confined electric field at the edges of the strip signifying the dipolar behavior of the strip. In contrast, due to the perpendicular orientation of the split gaps with respect to the incident electric field, the left and right SRRs couple very weakly with the incident electric field and thus, behave as dark modes.

The blue traces in Figure 5.2(b) represent the transmission spectrum of the two asymmetric SRRs. In the combined structure, the near field coupling between the strip and two SRRs urges to the excitation of the two dark SRRs. Due to the asymmetry of sizes between the two SRRs, two distinct transparency peaks are observed at 0.8 THz and 0.91 THz which are shown by dotted lines in Figures 5.2(c) and 5.2(d) respectively. The electric field profiles of the combined structure at the 1^{st} and 2^{nd} transparency peak frequencies are shown in Figures 5.2(g) and 5.2(h) respectively. It is apparent from the figures that the electric field is confined at the right SRR for 0.8 THz and at left SRR for 0.91 THz. The destructive interference between the strip and the two SRRs leads to dual transparency windows as well as the suppression of the dipolar excitation of the strip.

5.2 Polarization independent dual-band EIT effect

The MM structure (shown in Figure 5.1) exhibits the dual-band EIT effect only when the electric field of the incident terahertz light is along the y-direction. If we switch the polarization of the incident light, the dual-band EIT effect either diminishes or vanishes completely. Due to this polarization dependency, the proposed structure has limited applications in the development of devices, for example, sensing. In order to overcome this limitation and to make the structure polarization independent, we modify our existing structure by adding two more SRRs that are asymmetric and a strip in the perpendicular orientation. Figure 5.3 illustrates the newly modified structure comprising of a cross and four SRRs. In order to examine the polarization independent response of this new MM structure, we have numerically and experimentally investigated the transmission characteristics for two orthogonal polarizations of the incident terahertz light i.e., x- and y-polarized light. It is found that the new MM structure has similar dual-band EIT effect for both the orthogonal incident polarizations which confirms its polarization insensitive response. The simulated transmission response of the cross, four SRRs and the experimentally measured one for the coupled MM structure for x- and y-polarized incident light are shown in Figure 5.3 by the green and red traces respectively. The green arrow depicts the polarization of the incident light. Numerically simulated

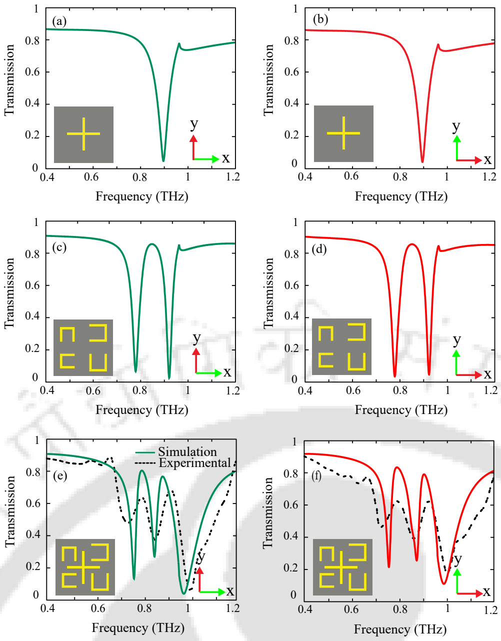

Figure 5.3: Terahertz transmission spectra for x-polarized incident light of cross (a), four SRRs (c), combined structure (e). Transmission of the cross (b), four SRRs (d), the combined structure (f) for y-polarized incident light. The polarization of the incident light is depicted by the green arrow. The dashed traces signify the measured transmission spectra of the combined structure. The corresponding MM structures are shown in the inset of figures.

transmission spectrum of the cross structure is shown in Figures 5.3(a) and 5.3(b) for the two orthogonal polarizations. The cross structure exhibits a dipole resonance at 0.89 THz for both the polarizations of the incident light. For x-polarized incident light, the horizontal strip plays the role of bright mode because the incident light couples strongly with it. On the other hand, for y-polarized incident light the vertical strip behaves as the bright mode since it is being excited directly by the incident light. Figures 5.3(c) and 5.3(d) illustrate the EIT effect of the four SRRs for incident x-and y-polarized terahertz light. One can note from the figures that the four SRRs have identical EIT effect for both the polarizations. For the x-polarized incident light, the SRRs in the second and fourth quadrants act as bright modes and the resonators in the first and third quadrants act as dark modes. The coupling between these bright modes of the second and fourth quadrants gives rise to a transparency window. However, due to the dark modes of first and third quadrants, the EIT window is slightly shifted. Similarly, we can conclude that due to the coupling between the bright modes resulting from the SRRs in the first and third quadrants for the y-polarized incident light, the four SRRs exhibits

EIT effects. In the combined structure, the coupling between the dipolar resonance of the cross and the EIT effect of four SRRs gives rise to a dual-band EIT effect (see insets of Figures 5.3(e) and 5.3(f). The green traces signify that for x-polarized incident light, the first transparency window ranges from 0.77 THz to 0.84 THz and second transparency window ranges from 0.87 THz to 0.94 THz (see Figure 5.3(e)). The red traces in Figure 5.3(f) represent the dual-band EIT effect of the proposed meta-molecule with y-polarized incident light and here the first and second transparency windows range from 0.76 THz to 0.84 THz and 0.88 THz THz to 0.94 THz THz respectively. Dotted lines in Figures 5.3(e) and 5.3(f) illustrate the measured transmission spectra of the coupled structure for x-and y-polarized incident light. The identical transmission spectrum of the combined structure for both the polarizations confirms the polarization independent behaviour of the structure.

Figures 5.4(a) and 5.4(b) depict the transmission response of the proposed MM structure for different angular incidences of the x-and y-polarized incident light. Here the black traces illustrate the transmission response for the normal incidence $\theta = 0^0$ and the red and green traces depict transmission responses for $\theta = 30^0$ and $\theta = 60^0$. From the Figure 5.4, one can observe that the proposed MM structure exhibits identical transmission response for different angle of incidences for both the orthogonal polarizations.

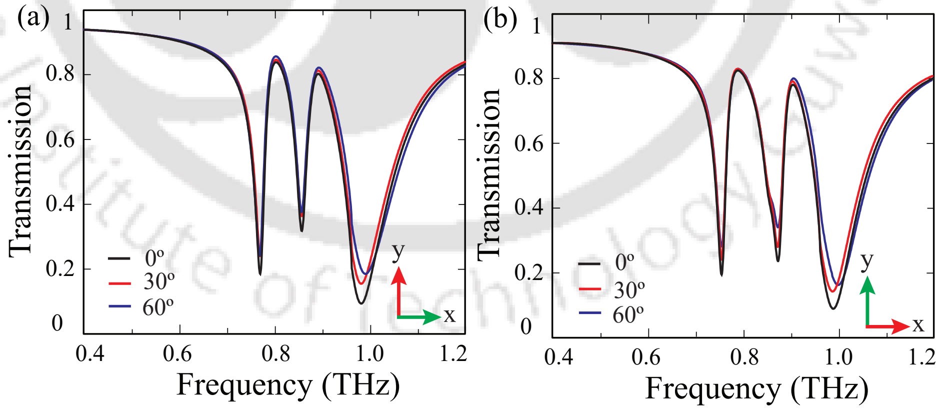

Figure 5.4: Simulated transmission response of the proposed MM structure for different incident angles from $\theta = 0^0$ to 60^0 for (a) x-polarized and (b) y-polarized incident light respectively.

Further, we discuss the modulation of the dual-band EIT effect in the proposed MM structure. The modulation has been achieved by changing diagonal distance of the four SRRs from the cross. Figures 5.5(a) and (b) depict the transmission of the proposed MM configuration for different diagonal distance (d) for incident x- and y-polarized light respectively. The red traces signify the widest transparency windows for $d = 10\ \mu m$ and blue traces represent narrowest windows for $d = 20\ \mu m$. The reduced coupling between the cross and four SRRs with increasing d leads to the narrowing of two transparency windows.

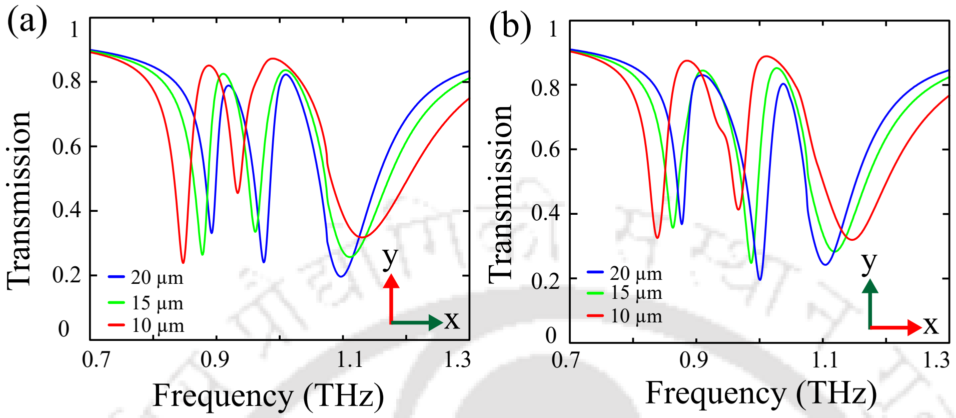

Figure 5.5: Numerically simulated transmission response of the combined structure for (a) x-polarized (b) y-polarized incident terahertz light for different diagonal distances between the cross and four SRRs.

5.3 Thin film sensing application

In order to show the practical use of our study, we examine sensing capability of the proposed MM structure. We have studied the transmission response for y-polarized incident light by varying the refractive index of the analyte of thickness 10 μm coated on the top of the MM sample. The results are shown in Figure 5.6. The results indicate that the 1^{st} transparency peak gets red shifted from 0.78 THz to 0.68 THz as the refractive index changes from 1.0 to 1.6. Similarly, the 2^{nd} transparency peak gets red shifted from 0.89 THz to 0.79 THz with the increase in refractive index. Here we have taken these values of refractive indices for theoretical convenience. To present the relationship between the frequency shift and refractive index, we have calculated the frequency shift of the 2^{nd} and 3^{rd} transmission dips with the change of refractive index of the analyte. The shifts are plotted in Figure 5.7. Here, the yellow traces illustrate the frequency shift of the 2^{nd} dip and the corresponding shift of the 3^{rd} dip is depicted by the blue traces. The results indicate a linear shift with increase in refractive index. Further, we have

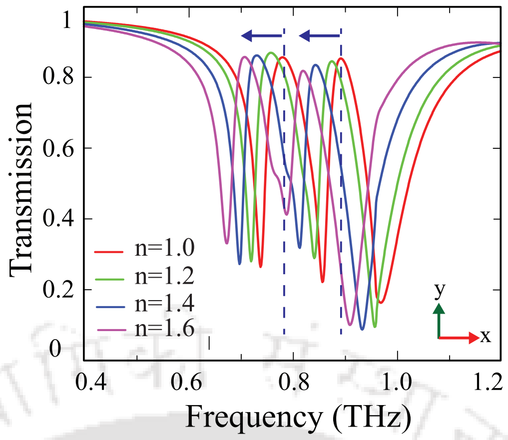

Figure 5.6: Numerically calculated transmission for the different refractive index of the analyte of thickness 10 μm coated on the top of the MM sample for y-polarized incident light.

calculated the sensitivity (S) of the transmission dips by taking derivative of frequency shift versus refractive index plot. The calculated sensitivities for the 1^{st}, 2^{nd} and 3^{rd} dips are 121 GHz/RIU, 138 GHz/RIU and 135 GHz/RIU (RIU, Refractive Index Unit) respectively. The results clearly reflect the potential use of the proposed MM structure and the dual-band EIT effect in refractive index sensing.

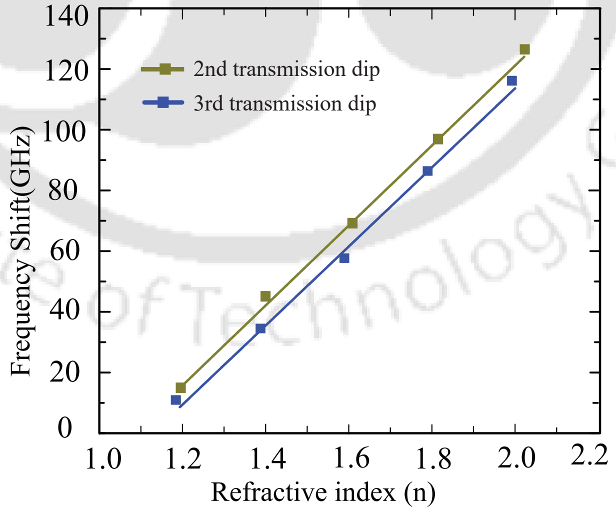

Figure 5.7: The frequency shift of the 2^{nd} and 3^{rd} transmission dips with refractive index of the analyte.

5.4 Analytical model based on four level tripod atomic system

To figure out the modulation mecchanism of the dual-band transparency windows in the MM structure and also to justify our numerical findings, we have used a four level tripod (FLT) system [149-152]. Figure 5.8 represents the energy level diagram for the tripod system. The levels $|0\rangle$, $|1\rangle$ and $|3\rangle$ construct a Λ system and exhibits an EIT effect. Here the transitions between $|0\rangle \rightarrow |3\rangle$ and $|1\rangle \rightarrow |3\rangle$ are driven by Rabi frequencies Ω_p and Ω_c, which are termed as probe and control transitions. δ_p and δ_c are the corresponding frequency detunings. In the presence of another control field $|2\rangle$ this Λ-system develops into tripod system and gives rise to dual-band EIT effect. In the tripod system, the Rabi frequency $\Omega_{c'}$ which is marked as the control field drives the transition between $|2\rangle \rightarrow |3\rangle$. Here the corresponding frequency detuning is $\delta_{c'}$. In analogy we can conclude that the four SRRs behaves like Λ-system and hence exhibits EIT effect. Finally the Λ-system develops into tripod system with the addition of cross structure that behaves as another control state and hence dual-band EIT effect can be achieved.

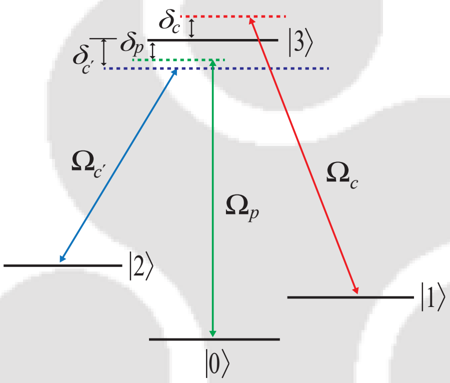

Figure 5.8: Energy level diagram of the tripod atomic-system. Here Ω_p, Ω_c and $\Omega_{c'}$ are probe and control fields and δ_p, δ_c and $\delta_{c'}$ are the corresponding frequency detunings.

One can write the equation of the tripod system as follows

$$\dot{\rho_{10}} = -[\gamma_{10} - i(\delta_p - \delta_c)]\rho_{10} + \frac{i}{2}\Omega_c{}^*\rho_{30} \tag{5.1a}$$

$$\dot{\rho_{20}} = -[\gamma_{20} - i(\delta_p - \delta'_c)]\rho_{20} + \frac{i}{2}\Omega'_c{}^*\rho_{30} \tag{5.1b}$$

$$\dot{\rho_{30}} = -[\gamma_{30} - i\delta_p]\rho_{30} + \frac{i}{2}(\Omega_p + \Omega_c\rho_{10} + \Omega_{c'}\rho_{20}) \tag{5.1c}$$

where, ρ_{i0} is the off-diagonal density matrix elements for the transition $|i\rangle \rightarrow |0\rangle$ ($|i\rangle = |1\rangle$, $|2\rangle$, $|3\rangle$) and γ_{i0} ($i = 1, 2, 3$) is the decay rates from $|i\rangle \rightarrow |0\rangle$. The exact solution for ρ_{30} can be derived from Eq. (5.1 c) as

$$\rho_{30} = \frac{-\Omega_p}{\left[2iA - \frac{|\Omega_c|^2}{2iB} - \frac{|\Omega_{c'}|^2}{2iC}\right]} \tag{5.2a}$$

$$A = \gamma_{30} - i\delta_p, \tag{5.2b}$$

$$B = \gamma_{10} - i(\delta_p - \delta_c) \tag{5.2c}$$

$$C = \gamma_{20} - i(\delta_p - \delta_{c'}) \tag{5.2d}$$

The transmission amplitude for the FLT-system is given by the expression, $t(\omega) = 1 - Im(\rho_{30})$ as

$$t(\omega) = 1 - Im\left(\frac{-2\Omega_p BC}{4iABC + iC|\Omega_c|^2 + iB|\Omega_{c'}|^2}\right) \tag{5.3}$$

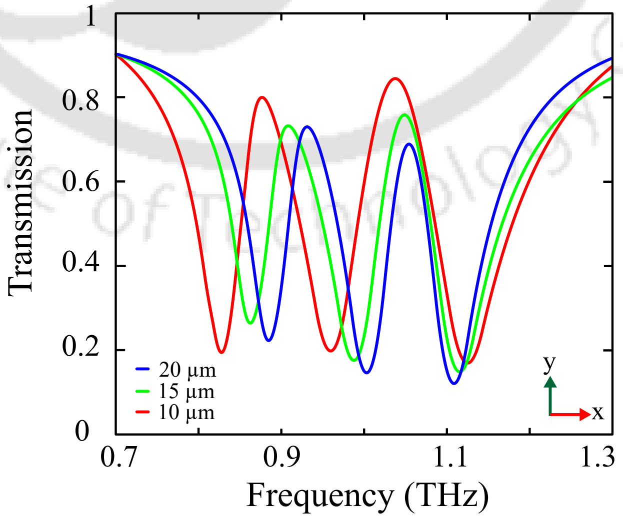

Figure 5.9: Depicts theoretically fitted transmission response for the coupled MM configuration for the y-polarized incident light.

We have used Eq. 5.3 and also carefully tuned the Rabi frequencies and the decay rates of each transition to obtain the theoretical fitted transmission spectrum. Figure 5.9. depicts the theoretically fitted transmission results which shows reasonable agreement with the corresponding simulated results depicted in Figure 5.5. In Figure 5.9 the red and blue traces illustrate the transmission spectra for $d = 10\ \mu m$ and $d = 20\ \mu m$ respectively. Here the cross and four SRRs are behaving as control state and Λ-system respectively. An increase in d reduces the coupling between the control state and Λ-system and hence the dual-band transparency windows get narrower.

5.5 Discussions

We have numerically and experimentally analyzed a coupled metamaterial comprising of a strip and two asymmetric SRRs that exhibits the dual-band EIT effect in the terahertz frequency regime. The dual-band EIT effect in the MM structure is achieved due to the near field coupling between the strip and the two asymmetric SRRs. Further, in order to obtain polarization independent response, we propose and experimentally analyzed another terahertz metamaterial comprising of a cross-wire and four SRRs. The transmission spectra of the coupled MM structure is analyzed for two orthogonal polarization directions of the incident light. The structure exhibits identical dual-band EIT response for both the orthogonal polarizations. The structure also exhibits identical transmission response for different angles of incidence for two orthogonal polarizations. Numerically, we have showed that the transmission peaks of both the transparency windows get red shifted from $0.78\ THz$ to $0.68\ THz$ and from $0.89\ THz$ to $0.79\ THz$ with the change of refractive index of $10\ \mu m$ placed on the top of the resonators. The theoretical sensitivity of the 1^{st}, 2^{nd} and 3^{rd} transmission dips are calculated as 121 GHz/RIU, 138 GHz/RIU and 135 GHz/RIU (RIU, Refractive Index Unit) respectively. In order to clarify the mechanism of modulation in the dual-band EIT effect and to validate our numerical findings, we have employed a four level tripod (FLT) system. It is observed that for specific values of the Rabi frequencies and the decay rates of each transition, our theoretically fitted results match well with the corresponding numerically simulated results. This study could also play an important role in the advancement of slow light devices, filters and modulators.

CHAPTER 6

INDEPENDENTLY TUNABLE MULTIBAND ELECTROMAGNETICALLY INDUCED TRANSPARENCY EFFECT AND DISPERSION

As discussed in last chapter, the electromagnetically induced transparency effect in the multi frequency bands has several interesting applications in photonics. As compared to the EIT effect in the single band, multiband provides the flexibility to manipulate light-matter interactions at multiple frequency points. The independent and controlled manipulation of the individual transparency window of the multiband spectrum has potential in slow light and filters. Further, the modulation of these independent frequency windows can be useful in frequency-selective devices. Recently several efforts have been made to modulate transparency windows both passively and actively. In the passive approach, the structural parameters are tuned to achieve modulation [114,143-146,153]. However, in active approach the modulation response is controlled through an external stimulation. In the multiband EIT studies made so far, simultaneous modulation of all the transparency windows and the associated dispersion properties have been achieved. In this chapter, we demonstrate the ability to independently modulate the desired transparency window in the multiband spectrum at the terahertz frequency regime.

Part of the results of this chapter have been published in the following paper: Independently tunable electromagnetically induced transparency effect and dispersion in a multi-band terahertz metamaterial R Sarkar, D Ghindani, KM Devi, SS Prabhu, A Ahmad, G Kumar – Scientific Reports 9(1), 1-10, 2019.

We experimentally examine a MM structure comprising a CW and two asymmetric double C resonators (DCRs) that exhibits multi-band EIT in the terahertz frequency regime. Each of the DCR is comprised of a pair of identical C resonators. The MM structure exhibits a multi-band EIT effect due to the coupling between bright CW and two pairs of asymmetric dark resonators i.e. left DCR and right DCR. Independent modulation of the desired transparency window is achieved by displacing the one resonator w.r.t the CW while keeping the other one fixed at its position. A strong linear dispersion within the two transparency windows results in a higher group refractive index and slow group velocity of terahertz in the proposed MM geometry. The design, evolution of multi-band EIT windows in the proposed MM geometry, the independent modulation of EIT windows are discussed in the different sections of the chapter.

6.1 Design and experimental details

The schematic illustration for the investigation of the multi-band EIT effect in the proposed planar metamaterial structure is shown in Figure 6.1. The unit cell of the proposed MM structure comprises of a pair of asymmetric DCRs and the CW, made up of gold having a thickness of $t = 200\ nm$, placed on a milky quartz substrate having dielectric permittivity of 4.68, periodicity, $P_x = P_y = 144\ \mu m$ and thickness, $h = 500\ \mu m$, is shown Figure 6.1(a). The CW has length, $L = 88\ \mu m$ and width, $w = 4\ \mu m$. The asymmetric DCRs, placed symmetrically on both side of the CW have same width, $w = 4\ \mu m$. The left DCR has length, $L_2 = 88\ \mu m$ and width, $a_2 = 34\ \mu m$ while the right DCR has length, $L_1 = 100\ \mu m$ and width, $a_1 = 40\ \mu m$. The vertical gap between the pair of C resonators in both the DCRs are kept fixed at $g = 20\ \mu m$. The distance between the CW and right DCR is termed as d_1 while the distance between the CW and left DCR is termed as d_2. Figure 6.1(b) represents the experimental schematic of the proposed MM structure. The optical micrograph image of the fabricated sample is shown in Figure 6.1(c). For the fabrication of the samples, electron beam lithography has been used in the clean room environment. The samples were fabricated on a milky quartz substrate having permittivity of 4.68 and thickness of 500 μm. For measurement commercially available terahertz Toptica system (Terahertz frequency domain spectroscopy) has been used. To resolve the spectral response of the MM sample, the frequency was swept from 50 GHz to 1220 GHz in 40MHz step size and integration time was three miliseconds. To reduce absorption of terahertz radiation by water vapour, the measurement was carried

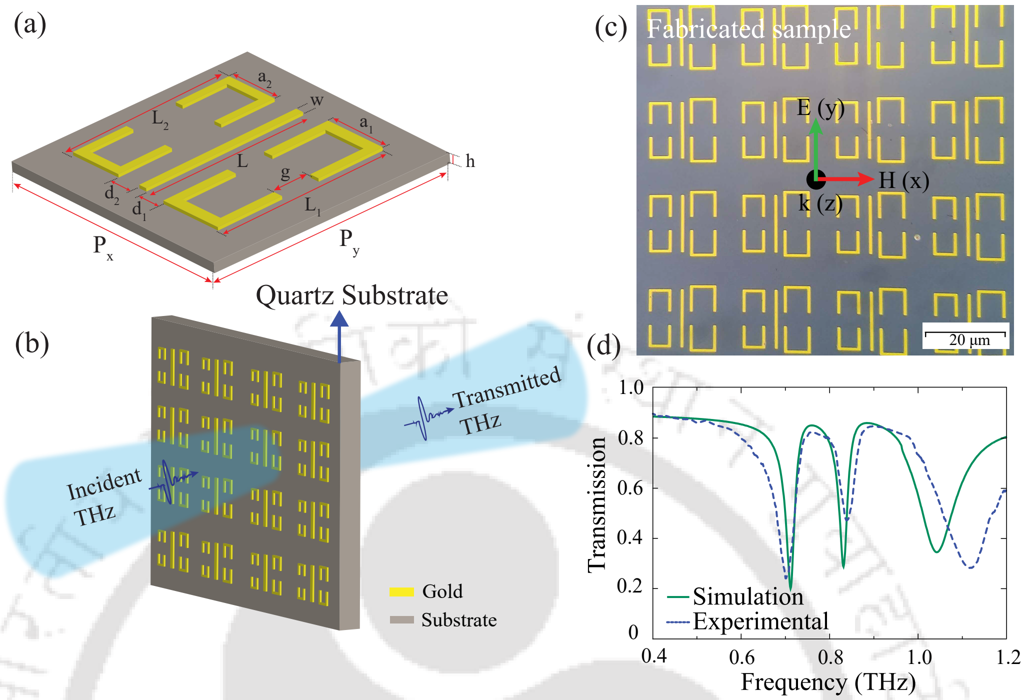

Figure 6.1: (a) The unit cell of the proposed metamaterial structure comprising of a CW and two asymmetric DCRs. The geometrical parameters are: $P_x = P_y = 144$, $h = 500$, $L = 88$, $w = 4$, $L_1 = 100$, $L_2 = 88$, $a_1 = 40$, $a_2 = 34$, $d_1 = d_2 = 10\ \mu m$. (b) Schematic depicting terahertz transmission through the proposed metamaterials geometry. (c) Shows optical micrograph image of the fabricated sample. (d) Depicts plot of the experimentally and numerically calculated terahertz transmission spectra of the proposed MM structure for the y-polarized incident light. Solid lines represent the simulated, while dotted line corresponds to the measured transmission spectra.

at room temperature in dry nitrogen atmosphere. In order to initially have an idea about the design of metamaterials samples and further elucidate the experimental results, we used commercially available simulation software called CST Microwave Studio. The numerically simulated and the experimentally measured transmission spectra of the MM structure are represented by the solid and the dotted lines, respectively, in Figure 6.1(d). From the figure, it is evident that the experimentally measured transmission spectra through the samples matches well with the numerically simulated one for lower frequencies. However, there is a slight mismatch at higher frequencies. At higher frequencies, the dimension of the unit cell of the MM geometry becomes comparable with the wavelength of the incident radiation. Hence, there will be more losses which results in a difference in broadness between the simulated and experimentally measured spetrum. A slight mismatch of the size between the fabricated and simulated geometries causes a difference in the frequencies. Further experimental optimizations may improve the results.

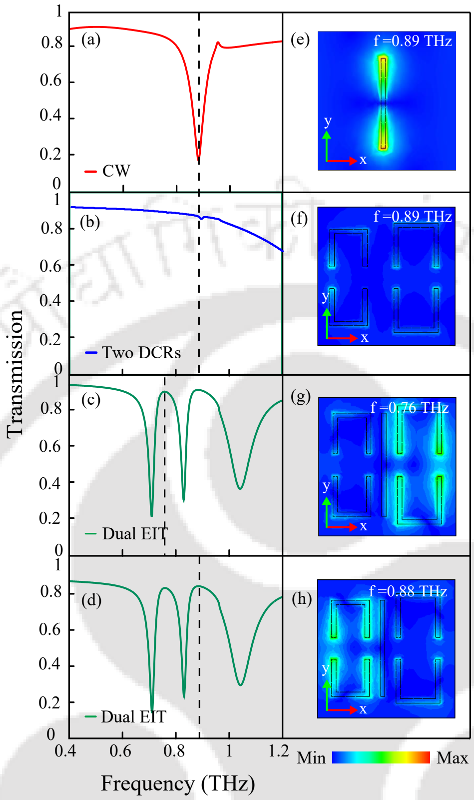

Figure 6.2: Terahertz transmission through the CW (a), the two asymmetric DCRs (b), the proposed MM configuration ((c) and (d)). (e)- (h) show electric field profiles for the cut wire (at 0.89 THz), two asymmetric DCRs (at 0.89 THz), transmission peak 1 (at 0.76 THz) and transmission peak 2 at (0.88 THz), respectively. (Polarization direction of incident electric field is represented by green arrow).

In order to understand the evolution of the multi-band EIT effect in the MM structure, we have examined the terahertz transmission response as well as induced electric field profiles in the CW, two DCRs and combined MM structure (see Figure 6.2). The incident terahertz light is polarized along the y-direction which is represented by the green arrow in the figure. The red traces in Figure 6.2(a) signify the transmission response of the CW. It can be seen that the CW is excited directly by the incident electric field and exhibits a dipolar resonance at 0.89 THz. This is also apparent from the induced electric field profile of the CW at the resonance frequency shown in Figure 6.2(e). Thus, the CW behaves as a bright mode. The transmission spectrum corresponding to the pair of DCRs is shown in Figure 6.2(b) (blue traces) and corresponding field profile is shown in

Figure 6.2(f). In contrast to the CW, the left and right DCRs are not directly excited by the incident electric field. This is because of the orientation of the two DCRs and their gaps which are perpendicular w.r.t. the incident electric field. Therefore, DCRs act as the dark modes. In the case of the combined structure shown in Figure 6.2(c), the near field coupling between the CW and DCRs excites the pair of dark DCRs on both sides of the CW. Then, the destructive interference between the bright dipolar and dark DCRs excitations leads to the multi-band EIT effect in the proposed metamaterial structure. Because of asymmetry in the sizes of DCR pairs, we get two distinct transparency peaks at frequencies at 0.76 THz and 0.89 THz marked by dotted lines in Figure 6.2(c) and Figure 6.2(d), respectively. The electric field profiles at the first and the second peak of the two transparency windows are shown in Figures 6.2(g) and 6.2(h), respectively. It may be observed in Figure 6.2(g) that the electric field is confined at the right DCR 0.76 THz , whereas, it is confined in the left DCR at 0.89 THz.

6.2 Independent modulation of multi-band transparency windows

The independent modulation of transparency windows in the multi-band EIT effect has significance in making slow light devices in the selected frequency range. Next we examine the independently tunable modulation characteristics of the transparency windows in our proposed asymmetric metamaterial configuration. The independent modulation of the EIT transparency windows will provide us the flexibility to choose the desired frequency for device designing and construction. In Figure 6.3, we show experimentally and numerically, the independent modulation of the transparency windows by varying the near field coupling between the CW and DCRs. The red traces represent simulated transmission spectra and corresponding experimentally measured spectra is indicated by the dashed traces. For the modulation of the 1^{st} window, distance, d_1 is varied from 10 μm to 25 μm to vary near field coupling between CW and right DCR (as shown in Figure 6.3(a)-(c)). For $d_1 = 10$ μm, the 1^{st} EIT window varies from 0.71 THz to 0.83 THz. As d_1 increases to $d_1 = 25$ μm, the window narrows down to 0.75 THz to 0.80 THz. In this modulation process, the left DCR is kept fixed at its position. Similarly, the independent modulation of 2^{nd} transparency window is investigated by changing the distance of the left DCR w.r.t. the CW (as shown in Figure 6.3(d)-(f)). In the figure,

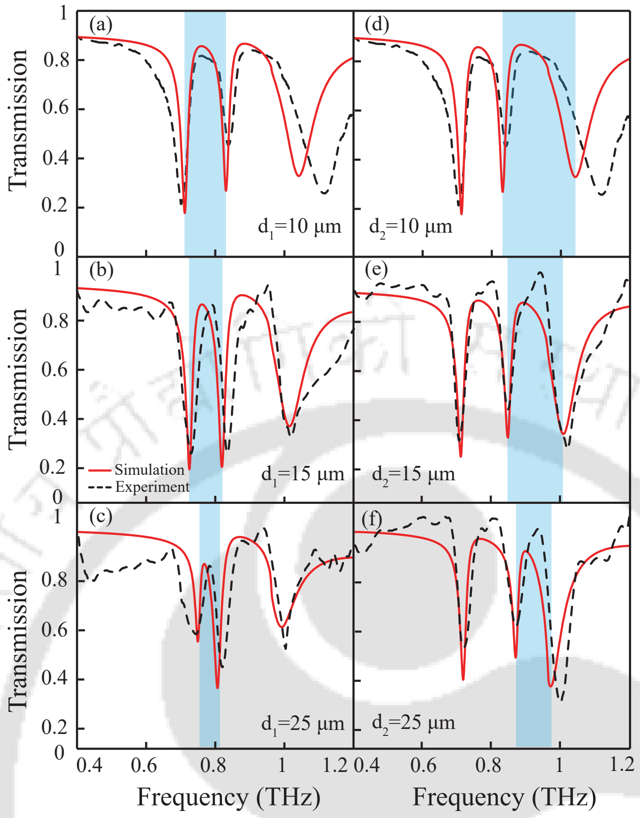

Figure 6.3: Simulated and experimentally measured terahertz transmission for various separation values 'd_1' and 'd_2' between the CW and the pair of DCRs. (a), (b) and (c) represents transmission for d_1= 10 μm, 15 μm and 25 μm respectively, whereas (d), (e), (f) corresponds to d_2= 10 μm, 15 μm and 25 μm respectively. The modulation in the transparency windows is reflected by the blue shaded color.

the red traces for $d_2 = 10$ μm corresponds to the most widest 2^{nd} EIT window ranging from 0.83 THz to 1.0 THz (shown by blue shaded area). The window narrows down to 0.87 THz to 0.97 THz for $d_2 = 25$ μm. It is worth mentioning that the peak frequencies of the transparency windows remain almost constant during the modulation process. Also our experimentally measured transmission spectra are in good agreement with the simulations.

In order to present a comprehensive picture of the independent modulation of the multi-band EIT effect, we have also plotted the contour and color plots for various displacements of right DCRs (d_1) and left DCRs (d_2) w.r.t. the CW. The contour plots are shown in Figures 6.4(a) and (b), respectively. In the figures, the frequency and displacement are drawn along x and y-axis and the strength of the signal is indicated through the color bar. The modulation of 1^{st} transparency window is apparent in Figure

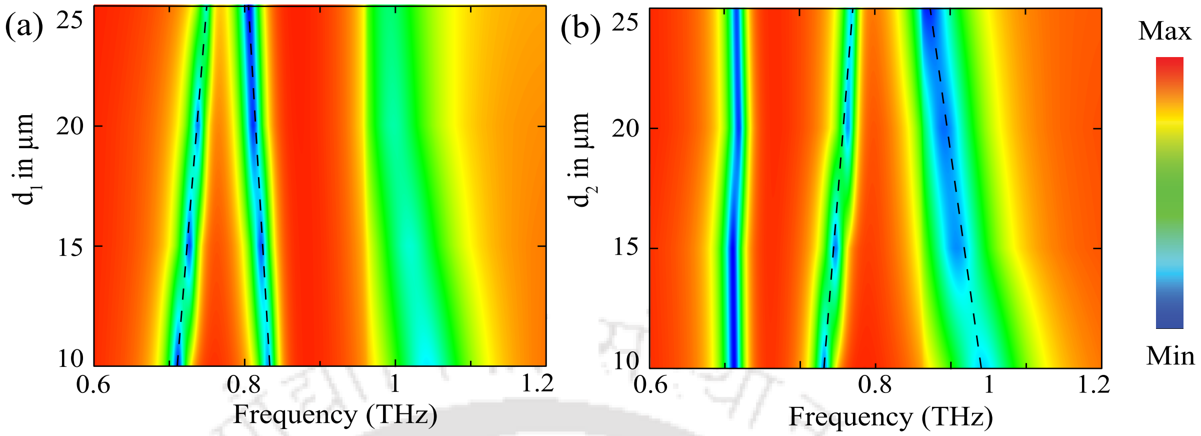

Figure 6.4: Contour plot of numerically simulated THz transmission for different distances between CW and DCRs. Color bar shows the magnitude of transmission intensity. (a) Represents contour plot for the variation of 1^{st} transparency window with distance between CW and right DCR. (b) Represents contour plot for the variation of 2^{nd} transparency window with distance between CW and left DCR respectively.

6.4(a) while the 2^{nd} transparency window remains almost unchanged. Again in Figure 6.4(b), the modulation of 2^{nd} EIT window is quite evident. Therefore, one can modulate the desired transparency window by keeping one DCR resonator fixed and displacing the other w.r.t. the CW in our proposed configuration. The feature could be useful in achieving selectively tunable response of the multi-band EIT effect.

6.3 Slow light effect

In EIT, we get transparency region in an otherwise absorptive region which is accompanied by the steep dispersion within the transparency window. A strongly dispersive media can cause the group velocity of light to slow down which has applications in enhanced nonlinear effects, pulse delay, optical buffers, etc [153-156]. The stronger phase dispersion occurs in the vicinity of the transparency windows and results in a larger group index (n_g) which is expressed as

$$n_g = \frac{c}{h}\frac{d\phi}{d\omega} \tag{6.1}$$

where, c is the velocity of light in free space, h is the substrate thickness and ϕ is the transmission phase of the MM structure. In Figure 6.5(a), we have plotted group index value as a function of frequency to have a quantitative appreciation of the group index values within the transparency windows. It is evident from the figure that the normal dispersion of the group index is accompanied by anomalous dispersion around the transparency windows. In order to understand the slow light property of the light passing through the proposed MM structure, we plot normalized group velocity (v_g/c) versus frequency in normally dispersive regions. The results are shown in Figures 6.5(b) and 6.5(c). Figure 6.5(b) depicts the variation of the group velocity versus frequency in the range of 0.78 THz to 0.81 THz falling within the 1^{st} transparency window. One may notice that group velocity decreases with an increase in frequency and ultimately becomes zero at 0.81 THz. Similarly, we see a reduction in the group velocity within the frequency range of 0.89 THz to 1.0 THz of the 2^{nd} transparency window as shown by the green traces in Figure 6.5(c). We observe more steep group velocity reduction in 2^{nd} window compared to the 1^{st} window. The results clearly indicate a slow light phenomenon at the multi-band regimes of the proposed MM configuration. One can also control the slow light behaviors at a specific frequency based upon the structural parameters of the MM configuration.

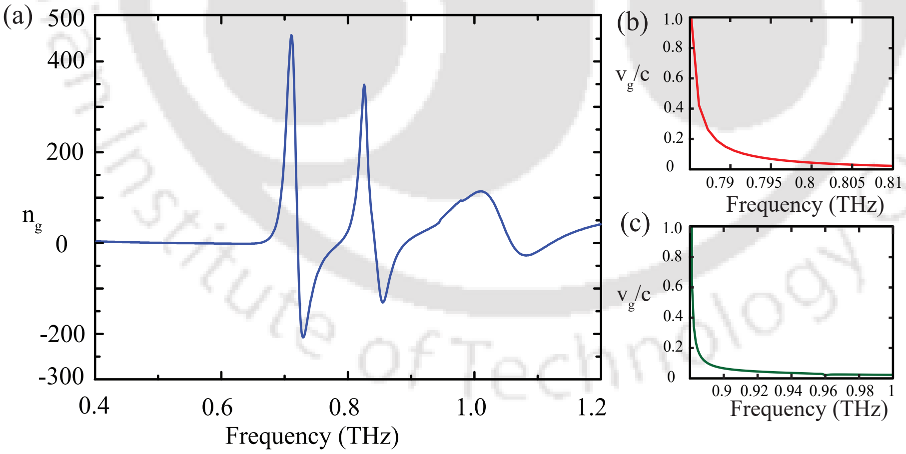

Figure 6.5: (a) Numerically calculated group refractive index versus frequency. (b) and (c) Depicts variation of group velocity versus frequency in the normally dispersive regimes of the 1^{st} and 2^{nd} transparency windows, respectively.

6.4 Theoretical modeling based on coupled harmonic oscillator systems

In order to further understand and validate numerical and experimental findings on multi-band transparency effect and independent modulation of transparency windows, we employ a theoretical model based on coupled harmonic oscillator systems. One can write equations of motion for the system as [157]

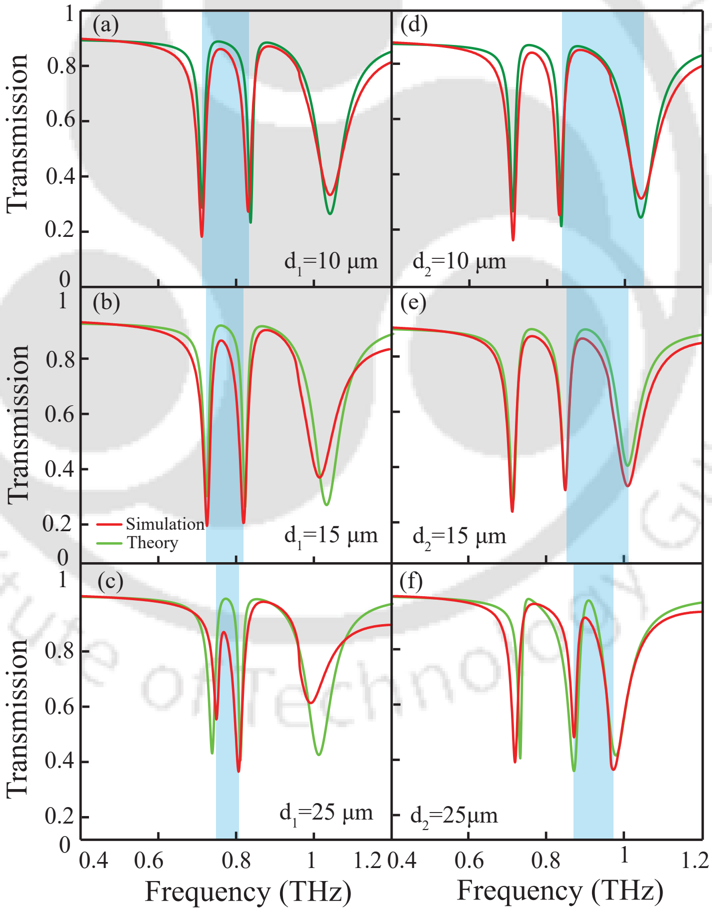

Figure 6.6: Simulated and theoretically fitted transmission spectra (a), (b), (c) for various distance (d_1) between the CW and right DCR for the modulation of 1^{st} transparency window and (d), (e), (f) for various distance (d_2) between CW and left DCR for the modulation of the 2^{nd} transparency window of the proposed multi-band EIT metamaterial.

$$\begin{aligned} x_1''(t)+\gamma_1 x_1'(t)+\omega_1^2 x_1(t)-\Omega_1^2 x_2(t)-\Omega_2^2 x_3(t) &= \frac{F_0}{m_1}e^{-i\omega t} \\ x_2''(t)+\gamma_2 x_2'(t)+\omega_2^2 x_2(t)-\Omega_1^2 x_1(t) &= 0 \\ x_3''(t)+\gamma_3 x_3'(t)+\omega_3^2 x_3(t)-\Omega_2^2 x_1(t) &= 0 \end{aligned} \tag{6.2}$$

where γ_1, γ_2, γ_3 and ω_1, ω_2, ω_3 are the damping factors and resonance frequencies of the CW, right DCR and left DCR and ω is the frequency of the incident terahertz light. Ω_1 and Ω_2 represents coupling coefficient between CW and two DCRs. Assuming the solution of equation (6.2) as

$$x_j = N_j e^{-i\omega t} + c.c \tag{6.3}$$

the energy dissipated by the MM structure exhibiting multi-band EIT effect is given as

$$P(\omega) = \frac{D_2 D_3 - \Omega_1^4}{D_1(D_2 D_3 - \Omega_1^4) - D_2\Omega_2^4} \tag{6.4}$$

where $D_1 = \omega_1^2 - \omega^2 - i\omega\gamma_1$, $D_2 = \omega_2^2 - \omega^2 - i\omega\gamma_2$, $D_3 = \omega_3^2 - \omega^2 - i\omega\gamma_3$.

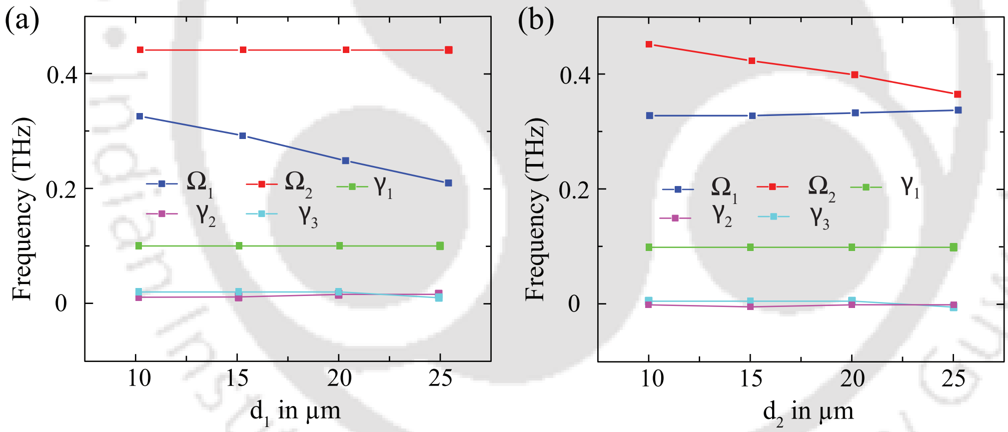

Figure 6.7: The variations of the fitting parameters γ_1, γ_2, γ_3, Ω_1 and Ω_2 as the function of (a) (d_1) for the modulation of 1^{st} transparency window and (b) (d_2) for the modulation of the 2^{nd} transparency window of the multi-band EIT spectrum.

The transmission amplitude for the system is given by the expression

$$t(\omega) = 1 - ImP(\omega) \tag{6.5}$$

One can use Eq. (6.5) to theoretical fit the numerically obtained transmission response. In Figure 6.6, we have shown theoretically fitted transmission spectrum which indicates reasonably good agreement with the numerical simulations. The solid red traces represent numerical simulations for various d_1 and d_2, while the solid green traces represent the corresponding theoretically fitted transmission spectrum. In order to understand the mechanism involved in modulation, we plot fitting parameters γ_1, γ_2, γ_3, Ω_1 and Ω_2 versus displacements 'd_1' and 'd_2' responsible for the coupling strength. The results are shown in Figure 6.7. The variations of the fitting parameters versus displacement d_1 are shown in Figure 6.7 (a). One may note that the coupling coefficient Ω_2 remains almost constant. This is due to the fact that coupling strength between the CW and left DCR do not change since d_2 remains constant in this case. On the other hand, coupling term Ω_1 decreases from 0.32 THz to 0.2 THz because of decrease in coupling strength with an increase in d_1. The damping parameters γ_1, γ_2, γ_3 do not vary with displacement as they are solely responsible for the loss associated with the modes. Similarly, we study the variation of the fitting parameters with displacement d_2 and results are shown in Figure 6.7(b). In this case, coupling term Ω_1 remains almost constant, however Ω_2 decreases from 0.45 THz to 0.36 THz. In this case, d_1 remains unchanged resulting in same coupling strength, however a change in Ω_2 reflects a change in coupling strength because of variation in d_2. Again the fitting parameters for damping coefficients remains unchanged in this case also. Therefore, one can control the coupling strength by varying the displacement between CW and resonators to achieve a desirable modulation response.

6.5 Discussions

A coupled terahertz metamaterial comprising of a CW and two pair of asymmetric DCRs exhibiting multi-band EIT effect is numerically and experimentally investigated. The evolution of multi-band EIT effect in the MM structure is achieved via near field coupling between the CW and DCRs. An independent modulation of the EIT transparency windows is achieved by displacing one DCR w.r.t the CW while keeping the other fixed. As the separation of one DCR from the CW increases, the coupling between them decreases, leading to the narrowing of one transparency window, however other remains unchanged. We analyzed strongly dispersion characteristics of the transparency windows as well as the associated slow light effect. It is observed that the group velocity reduces by a factor of $0.2c$ at 0.79 THz in the 1^{st} transparency region. In order to understand the mechanism of independent modulation as well as validate our numerical and experimental findings, we employed a mechanical model based on coupled harmonic oscillator system. The model shows that the modulation of the 1^{st} and 2^{nd} transparency windows are achieved due to the variation of the coupling terms Ω_1 and Ω_2 respectively. The model predicts terahertz transmission spectrum in a good agreement with experiments and simulations. Our study is vital in the development of multi-band slow light devices, buffers, modulators, etc.

CHAPTER 7

SUMMARY AND FUTURE SCOPE

7.1 Summary

In the thesis work, we have numerically and experimentally investigated polarization conversion and several related aspects in planar terahertz metamaterials. This includes polarization insensitive dual band electromagnetically induced transparency (EIT) effect, independent control of multiband transparency windows, steep linear dispersion and slow light properties of tearahertz radiation. We have divided thesis into seven chapters and a brief summary of results and new findings is given below.

In chapter 1, we presented a comprehensive literature review of terahertz metamaterials and introduction to polarization conversion devices and potentials of EIT effect in sensing and the slow light phenomenon.

In chapter 2, we discuss the design, fabrication and characterization of terahertz metamaterials. To interpret and validate the numerical findings and experimental observations, we have discussed different theoretical models briefly in this chapter.

In chapter 3, we discuss gradual polarization conversion of incident terahertz in a planar MM geometry whose unit cell comprises of two circular split ring resonators having a single split gap. We have investigated co-and cross-polarization transmission spectra of the proposed geometry by changing the rotation angles of one resonator concerning the other from 0° to 180° in steps of 15°. The cross polarization amplitude is found to increase with the rotation angle and becomes maximum for rotation angle of 90°. In this case, the near field coupling between the resonators becomes maximum. Further, the cross polarization amplitude tends to decrease with the rotation angle and again becomes zero for rotation angle of 180°. Hence based upon the rotation angle between the resonators we have been able to tune the cross polarization from minimum to maximum and then back to the minimum which is quite significant terahertz polarization conversion devices. We have employed RLC circuit model to understand the polarization conversion in our proposed geometry.

In chapter 4, we discuss ultra-wideband efficient polarization conversion both numerically and experimentally. The unit cell of the proposed MM geometry is comprised of a C-resonator. We have rotated the MM geometry from 0° to 90° in steps of 15° w.r.t. the incident terahertz. For different rotation angles, the co-and cross-polarization transmission spectra are obtained. The geometry shows 40% cross polarization conversion in the frequency range from 1.22 THz to 2.75 THz with a maximum of 45% conversion for rotation angle of 45°. Further, we have computed induced electric field profiles and surface current distributions for rotation angles of 0°, 45° and 90° to understand the broadband polarization conversion. It is observed that the change of rotation angle induces an electric dipole which radiates field in the orthogonal direction of the incident terahertz, resulting in the cross polarization conversion. Furthermore, the transmission spectrum is found to shifted to higher frequency side with respect to a change in the dimension of the C-resonator. This gives us the flexibility to design and construct broadband polarization conversion devices over a selective frequency band.

In chapter 5, we discuss dual band EIT effect in a coupled terahertz metamaterial whose unit cell comprises of two asymmetric C-shaped resonators placed alternately on both sides of the cut-wire (CW) structure. The proposed structure exhibits dual band EIT effect due to the near field coupling between the CW and the pair of C-resonators. We further discuss polarization insensitive dual-band EIT effect in another MM configuration comprised of a cross and four C-resonators. Simulation and experimental results show identical transmission profile for different angles of incidence for two orthogonal polarizations of the incident terahertz beam. The transparency window is modulated by displacing the C-resonators diagonally with respect to the cross-wire. Further we have explored thin film sensing capability of our proposed geometry by studying the terahertz transmission through it by changing refractive index of an analyte of thickness 10 µm on top of the resonators. We have calculated the sensitivities for the 1st, 2nd and 3rd transmission dips as 121 GHz/RIU, 138 GHz/RIU and 135 GHz/RIU (RIU, Refractive

Index Unit). The study promises polarization insensitive sensing characteristics.

In chapter 6, we discuss independent tuning of multiband transparency windows in a planar terahertz metamaterial whose metamolecule unit comprises of a pair of double C-resonators (DCRs) placed symmetrically on both sides of the middle vertical cut-wire (CW). Each DCR is comprised of two identical C-resonators. Here the multiband EIT effect occurs due to the near field coupling between the CW and left and right DCRs. Independent control of each transparency window is demonstrated both numerically and experimentally by changing the horizontal separation between the CW and one DCR, keeping the other DCR fixed at its position. Further, we examined the dispersion and slow light properties of transmitted terahertz in our proposed geometry within the transparency windows. The numerical and experimental results have been interpreted and validated using a coupled harmonic oscillator model in this chapter.

7.2 Future scope of work

Polarization conversion of terahertz using metamaterials has emerged as one of the promising areas of research owing to its potential in terahertz device development [63, 64, 68]. Polarization control and conversion have significance in optical setups, communications devices, and display systems. Our study of gradual polarization control using near-field coupled metamaterials can open new avenues for the realization of polarization conversion and hence the construction of devices in the terahertz frequency regime. The broadband polarization conversion is another important aspect in designing broadband terahertz photonic components [60, 61, 65, 70]. We have demonstrated a simple and effective approach for broadband polarization control. We have shown that our approach is capable of providing nearly 45% conversion of incident linearly polarized light. This can be further improved to enhance the efficiency with more optimized designs of the metamaterials. In our study, we have demonstrated polarization conversion using planar metamaterials. Polarization conversion efficiency can be enhanced using stacked configurations. The stacked metamaterials can result in enhance free space couplings of incident THz power, thereby improving the polarization conversion efficiency.

The MM structures with careful design can result in electromagnetically induced transparency effect (EIT) which has potential in slow light devices, sensors, and modulation in the broadband as well as narrow frequency band. The narrow transparency window is accompanied by a steep linear dispersion, which can be exploited for slow light applications [153,154]. Further, the narrow transparency peak with a high Q factor has potential in sensing applications. For practical applications, the EIT effect is desirable to be polarization insensitive. In this context, our study of the polarization-insensitive dual-band EIT effect can be crucial to developing polarization-independent sensors and slow light devices. Independent control of multiband transparency windows can be significant to the development of buffers, modulators, and filtering devices in selective frequency regions.

In this thesis work, we have broadly focused upon investigating passive control of MM transmission response and conversion of terahertz polarization using metamaterial structures. With the advancement of fabrication techniques and simulation tools, dynamic control of these effects can be examined in the metamaterials. Numerous 2D materials such as graphene, MOS2, Boron nitride, etc. can be integrated with our designs to actively control polarization conversion [62,158]. This can further help in modulating the terahertz transmission response actively, including the EIT effect, useful for terahertz photonic devices development. Our study on the dual-band EIT effect can be extended to examine the triple-band EIT effect by carefully designing MM structures in planar and stacked multilayer configurations. In our study, we have shown the thin-film sensing capability of our proposed geometry. This study can be extended to design more novel designs and configurations with optimized parameters for developing ultrasensitive biosensors for the detection of cancer cells and virus-like Covid-19. In this context, meta-waveguide designs can be investigated to increase the interaction of incident terahertz with the analyte attached to resonators.

BIBLIOGRAPHY

[1] Zhang, X.-C. and J. Xu, Introduction to THz wave photonics. Vol. 29. 2010: Springer.

[2] Tonouchi, M., Cutting-edge terahertz technology. Nature Photonics, 2007. 1(2): p. 97-105.

[3] Yu, C., et al., The potential of terahertz imaging for cancer diagnosis: A review of investigations to date. Quantitative imaging in medicine and surgery, 2012. 2(1): p. 33.

[4] Siegel, P.H., Terahertz technology in biology and medicine. IEEE transactions on microwave theory and techniques, 2004. 52(10): p. 2438-2447.

[5] Smye, S., et al., The interaction between terahertz radiation and biological tissue. Physics in Medicine and Biology, 2001. 46(9): p. R101.

[6] Wietzke, S., et al., Determination of additive content in polymeric compounds with terahertz time-domain spectroscopy. Polymer Testing, 2007. 26(5): p. 614-618.

[7] Wietzke, S., et al., Terahertz imaging: a new non-destructive technique for the quality control of plastic weld joints. Journal of the European Optical Society-Rapid Publications, 2007. 2.

[8] Jördens, C. and M. Koch, Detection of foreign bodies in chocolate with pulsed terahertz spectroscopy. Optical Engineering, 2008. 47(3): p. 037003.

[9] Shen, Y., et al., Detection and identification of explosives using terahertz pulsed spectroscopic imaging. Applied physics letters, 2005. 86(24): p. 241116.

[10] Song, Q., et al., Fast continuous terahertz wave imaging system for security. Optics Communications, 2009. 282(10): p. 2019-2022.

[11] Kemp, M.C., et al. Security applications of terahertz technology. in Terahertz for Military and Security Applications. 2003. International Society for Optics and Photonics.

[12] Woodward, R., et al., Terahertz pulsed imaging of skin cancer in the time and frequency domain. Journal of Biological Physics, 2003. 29(2): p. 257-259.

[13] D'Arco, A., et al., THz pulsed imaging in biomedical applications. Condensed Matter, 2020. 5(2): p. 25.

[14] Peter, B.S., et al., Development and testing of a single frequency terahertz imaging system for breast cancer detection. IEEE Transactions on Terahertz Science and Technology, 2013. 3(4): p. 374-386.

[15] Globus, T., et al., THz-frequency spectroscopic sensing of DNA and related biological materials. International Journal of High-Speed Electronics and Systems, 2003. 13(04): p. 903-936.

[16] Veselago, V.G., The electrodynamics of substances with simultaneously negative values of ϵ and μ. Soviet physics uspekhi, 1968. 10(4): p. 509.

[17] Pendry, J.B., et al., Extremely low-frequency plasmons in metallic mesostructures. Physical review letters, 1996. 76(25): p. 4773.

[18] Pendry, J.B., et al., Magnetism from conductors and enhanced nonlinear phenomena. IEEE transactions on microwave theory and techniques, 1999. 47(11): p. 2075-2084.

[19] Shelby, R.A., D.R. Smith, and S. Schultz, Experimental verification of a negative index of refraction. science, 2001. 292(5514): p. 77-79.

[20] Landy, N.I., et al., Perfect metamaterial absorber. Physical review letters, 2008. 100(20): p. 207402.

[21] Chen, H.-T., et al., A metamaterial solid-state terahertz phase modulator. Nature Photonics, 2009. 3(3): p. 148-151.

[22] Drezet, A., C. Genet, and T.W. Ebbesen, Miniature plasmonic wave plates. Physical review letters, 2008. 101(4): p. 043902.

[23] Bai, B., et al., Optical activity in planar chiral metamaterials: Theoretical study. Physical Review A, 2007. 76(2): p. 023811.

[24] Drezet, A., et al., Optical chirality without optical activity: How surface plasmons give a twist to light. Optics express, 2008. 16(17): p. 12559-12570.

[25] Landy, N. and Smith, D.R., 2013. A full-parameter unidirectional metamaterial cloak for microwaves. Nature materials, 12(1), pp.25-28.

[26] Zhang, X. and Z. Liu, Superlenses to overcome the diffraction limit. Nature materials, 2008. 7(6): p. 435-441.

[27] Pendry, J.B., Negative refraction makes a perfect lens. Physical review letters, 2000. 85(18): p. 3966.

[28] Oh, J.H., Min Seung, H. and Young Kim, Y., 2014. A truly hyperbolic elastic metamaterial lens. Applied Physics Letters, 104(7), p.073503.

[29] Al-Naib, I.A.I., C. Jansen, and M. Koch, Thin-film sensing with planar asymmetric metamaterial resonators. Applied Physics Letters, 2008. 93(8): p. 083507.

[30] Chen, T., S. Li, and H. Sun, Metamaterials application in sensing. Sensors, 2012. 12(3): p. 2742-2765.

[31] Tao, H., et al., Highly flexible wide angle of incidence terahertz metamaterial absorber: Design, fabrication, and characterization. physical review B, 2008. 78(24): p. 241103.

[32] Chiang, Y.-J., et al., An ultrabroad terahertz bandpass filter based on multiple-resonance excitation of a composite metamaterial. Applied Physics Letters, 2011. 99(19): p. 191909.

[33] Chiam, S.-Y., et al., Analogue of electromagnetically induced transparency in a terahertz metamaterial. Physical Review B, 2009. 80(15): p. 153103.

[34] Wang, B., et al., Wavelength de-multiplexing metasurface hologram. Scientific Reports, 2016. 6(1): p. 1-6.

[35] Seo, M., et al., Active terahertz nanoantennas based on VO2 phase transition. Nano letters, 2010. 10(6): p. 2064-2068.

[36] Chen, H.-T., et al., Tuning the resonance in high-temperature superconducting terahertz metamaterials. Physical review letters, 2010. 105(24): p. 247402.

[37] He, X., et al., Implementation of selective controlling electromagnetically induced transparency in terahertz graphene metamaterial. Carbon, 2017. 123: p. 668-675.

[38] Quader, S., et al., Graphene-based high-efficiency broadband tunable linear-to-circular polarization converter for terahertz waves. IEEE Journal of Selected Topics in Quantum Electronics, 2020. 26(5): p. 1-8.

[39] Shen, N.-H., et al., Optically implemented broadband blueshift switch in the terahertz regime. Physical Review Letters, 2011. 106(3): p. 037403.

[40] Plum, E., V. Fedotov, and N. Zheludev, Optical activity in the extrinsically chiral metamaterial. Applied physics letters, 2008. 93(19): p. 191911.

[41] Chin, J.Y., et al., Nonreciprocal plasmonics enables giant enhancement of thin-film Faraday rotation. Nature communications, 2013. 4(1): p. 1-6.

[42] Cheng, Y., et al., Giant circular dichroism and negative refractive index of chiral metamaterial based on split-ring resonators. Progress In Electromagnetics Research, 2013. 138: p. 421-432.

[43] Kenanakis, G., et al., Three-dimensional infrared metamaterial with the asymmetric transmission. ACS Photonics, 2015. 2(2): p. 287-294.

[44] Xu, J., et al., Ultra-broadband linear polarization converter based on anisotropic metasurface. Optics express, 2018. 26(20): p. 26235-26241.

[45] Zhao, J. and Y. Cheng, A high-efficiency and broadband reflective 90° linear polarization rotator based on anisotropic metamaterial. Applied Physics B, 2016. 122(10): p. 1-7.

[46] Pfeiffer, C., et al., Polarization rotation with ultra-thin bianisotropic metasurfaces. Optica, 2016. 3(4): p. 427-432.

[47] Cheng, Y., et al., Ultra-compact multi-band chiral metamaterial circular polarizer based on the triple twisted split-ring resonator. Progress In Electromagnetics Research, 2016. 155: p. 105-113.

[48] Kan, T., et al., Enantiomeric switching of chiral metamaterial for terahertz polarization modulation employing vertically deformable MEMS spirals. Nature communications, 2015. 6(1): p. 1-7.

[49] Kwon, D.-H., P.L. Werner, and D.H. Werner, Optical planar chiral metamaterial designs for strong circular dichroism and polarization rotation. Optics express, 2008. 16(16): p. 11802-11807.

[50] Song, K., et al., A frequency-tunable 90-polarization rotation device using composite chiral metamaterials. Applied Physics Letters, 2013. 103(10): p. 101908.

[51] Zhang, W., et al., Intensity modulation and polarization rotation of visible light by dielectric planar chiral metamaterials. Applied Physics Letters, 2005. 86(23): p. 231905.

[52] Huang, C., et al., Asymmetric electromagnetic wave transmission of linear polarization via polarization conversion through chiral metamaterial structures. Physical Review B, 2012. 85(19): p. 195131.

[53] Menzel, C., et al., Asymmetric transmission of linearly polarized light at optical metamaterials. Physical review letters, 2010. 104(25): p. 253902.

[54] Wei, Z., et al., Broadband polarization transformation via enhanced asymmetric transmission through arrays of twisted complementary split-ring resonators. Applied Physics Letters, 2011. 99(22): p. 221907.

[55] Singh, R., et al., Terahertz metamaterial with the asymmetric transmission. Physical Review B, 2009. 80(15): p. 153104.

[56] Wu, L., et al., Giant asymmetric transmission of circular polarization in layer-by-layer chiral metamaterials. Applied Physics Letters, 2013. 103(2): p. 021903.

[57] Wu, L., et al., Circular polarization converters based on bi-layered asymmetrical split ring metamaterials. Applied Physics A, 2014. 116(2): p. 643-648.

[58] Chiang, Y.-J. and T.-J. Yen, A composite-metamaterial-based terahertz-wave polarization rotator with an ultrathin thickness, an excellent conversion ratio, and enhanced transmission. Applied Physics Letters, 2013. 102(1): p. 011129.

[59] Peralta, X.G., et al., Metamaterials for THz polarimetric devices. Optics express, 2009. 17(2): p. 773-783.

[60] Grady, N.K., et al., Terahertz metamaterials for linear polarization conversion and anomalous refraction. Science, 2013. 340(6138): p. 1304-1307.

[61] Cheng, Y.Z., et al., Ultrabroadband reflective polarization convertor for terahertz waves. Applied Physics Letters, 2014. 105(18): p. 181111.

[62] Zhang, Y., et al., Tunable broadband polarization rotator in terahertz frequency based on graphene metamaterial. Carbon, 2018. 133: p. 170-175.

[63] Cong, L., et al., Polarization control in terahertz metasurfaces with the lowest order rotational symmetry. Advanced Optical Materials, 2015. 3(9): p. 1176-1183.

[64] Cong, L., et al., Highly flexible broadband terahertz metamaterial quarterwave plate. Laser and Photonics Reviews, 2014. 8(4): p. 626-632.

[65] Zheng, X.-x., Z.-y. Xiao, and X.-y. Ling, Broadband and efficient reflective polarization converter based on a three-dimensional metamaterial. Optical and Quantum Electronics, 2016. 48(10): p. 1-9.

[66] Xu, Z., et al., Terahertz broadband polarization converter based on the double-split ring resonator metasurface. SN Applied Sciences, 2021. 3(9): p. 1-7.

[67] Gao, X., et al., Bandwidth broadening of a linear polarization converter by near-field metasurface coupling. Scientific reports, 2017. 7(1): p. 1-8.

[68] Cong, L., et al., A perfect metamaterial polarization rotator. Applied Physics Letters, 2013. 103(17): p. 171107.

[69] Li, C., et al., Resonance coupling and polarization conversion in terahertz metasurfaces with twisted split-ring resonator pairs. Optics Express, 2017. 25(21): p. 25842-25852.

[70] Ma, S., et al., Ultra-wideband reflective metamaterial wave plates for terahertz waves. EPL (Europhysics Letters), 2017. 117(3): p. 37007.

[71] Singh, R., et al., The impact of nearest neighbour interaction on the resonances in terahertz metamaterials. Applied Physics Letters, 2009. 94(2): p. 021116.

[72] Singh, R., et al., Coupling between a dark and a bright eigenmode in a terahertz metamaterial. Physical Review B, 2009. 79(8): p. 085111.

[73] Singh, R., et al., Observing metamaterial induced transparency in individual Fano resonators with broken symmetry. Applied Physics Letters, 2011. 99(20): p. 201107.

[74] Rao, S.J.M., et al., Modulating fundamental resonance in capacitive coupled asymmetric terahertz metamaterials. Scientific reports, 2018. 8(1): p. 1-8.

[75] Shen, S., et al., Tunable electromagnetically induced reflection with a high Q factor in complementary Dirac semimetal metamaterials. Materials Research Express, 2018. 5(12): p. 125804.

[76] Zhang, S., et al., Plasmon-induced transparency in metamaterials. Physical review letters, 2008. 101(4): p. 047401.

[77] Hebin Li, Vladimir A Sautenkov, Yuri V Rostovtsev, George R Welch, Philip R Hemmer, and Marlan O Scully. Physical Review A, 80(2):023820, 2009.

[78] Zhengyang Bai, Guoxiang Huang, Lixiang Liu, and Shuang Zhang. Scientic reports, 5:13780, 2015.

[79] Jingjing Zhang, Sanshui Xiao, Claus Jeppesen, Anders Kristensen, and Niels Asger Mortensen. Optics express, 18(16):17187–17192, 2010.

[80] Jinyan Diao, Bingxin Han, Jie Yin, Xiangjun Li, Tingting Lang, and Zhi Hong. IEEE Photonics Journal, 2019.

[81] Muhammad Amin and Adnan D Khan. The Journal of Physical Chemistry C, 119(37):21633– 21638, 2015.

[82] Manukumara Manjappa, Sher-Yi Chiam, Longqing Cong, Andrew A Bettiol, Weili Zhang, and Ranjan Singh. Applied Physics Letters, 106(18):181101, 2015.

[83] Koijam Monika Devi, Amarendra K Sarma, Dibakar Roy Chowdhury, and Gagan Kumar. Optics express, 25(9):10484–10493, 2017.

[84] Tingting Liu, Chaobiao Zhou, Le Cheng, Xiaoyun Jiang, Guangzhao Wang, Chen Xu, and Shuyuan Xiao. Actively tunable slow light in a terahertz hybrid metal-graphene metamaterial. Journal of Optics, 21(3):035101, 2019.

[85] FY Meng, JH Fu, K Zhang, Q Wu, JY Kim, JJ Choi, B Lee, and JC Lee. Journal of Physics D: Applied Physics, 44(26):265402, 2011.

[86] Renxia Ning, Jie Bao, Yunji Meng, and Zhenhai Chen. Wideband reciprocity tunable electromagnetically induced transparency in complementary graphene metasurface. Journal of Optics, 21(4):045106, 2019.

[87] Grant, J., et al., Polarization insensitive terahertz metamaterial absorber. Optics Letters, 2011. 36(8): p. 1524-1526.

[88] Ma, Y., et al., A terahertz polarization insensitive dual-band metamaterial absorber. Optics Letters, 2011. 36(6): p. 945-947.

[89] Duan, X., et al., Polarization-insensitive and wide-angle plasmonically induced transparency by planar metamaterials. Applied Physics Letters, 2012. 101(14): p. 143105.

[90] Zhang, X., et al., Polarization-independent plasmon-induced transparency in a fourfold symmetric terahertz metamaterial. IEEE Journal of Selected Topics in Quantum Electronics, 2012. 19(1): p. 8400707-8400707.

[91] Driscoll, T., et al., Tuned permeability in terahertz split-ring resonators for devices and sensors. Applied Physics Letters, 2007. 91(6): p. 062511.

[92] O'Hara, J.F., et al., Thin-film sensing with planar terahertz metamaterials: sensitivity and limitations. Optics Express, 2008. 16(3): p. 1786-1795.

[93] Tao, H., et al., Performance enhancement of terahertz metamaterials on ultrathin substrates for sensing applications. Applied Physics Letters, 2010. 97(26): p. 261909.

[94] Han, B., et al., A sensitive and selective terahertz sensor for the fingerprint detection of lactose. Talanta, 2019. 192: p. 1-5.

[95] Debus, C. and P.H. Bolivar, Frequency selective surfaces for high sensitivity terahertz sensing. Applied Physics Letters, 2007. 91(18): p. 184102.

[96] Singh, R., et al., Ultrasensitive terahertz sensing with high-Q Fano resonances in metasurfaces. Applied Physics Letters, 2014. 105(17): p. 171101.

[97] Srivastava, Y.K., L. Cong, and R. Singh, Dual-surface flexible THz Fano metasensor. Applied Physics Letters, 2017. 111(20): p. 201101.

[98] Li, W., et al., High-Q multiple Fano resonances sensor in single dark mode metamaterial waveguide structure. IEEE Photonics Technology Letters, 2018. 30(23): p. 2068-2071.

[99] Kong, Y., et al., Multiple Fano resonance-based optical refractive index sensor composed of micro-cavity and micro-structure. IEEE Photonics Journal, 2018. 10(6): p. 1-10.

[100] Saadeldin, A.S., et al., Highly sensitive terahertz metamaterial sensor. IEEE Sensors Journal, 2019. 19(18): p. 7993-7999.

[101] He, X., et al., Tunable ultrasensitive terahertz sensor based on complementary graphene metamaterials. RSC Advances, 2016. 6(57): p. 52212-52218.

[102] Gupta, M., et al., Sensing with toroidal metamaterial. Applied Physics Letters, 2017. 110(12): p. 121108.

[103] Li, S.-X., H.-W. Zhao, and J.-G. Han, Terahertz metamaterial sensor based on electromagnetically induced transparency effect. J. Electron. Sci. Technol., 2019. 431(2): p. 115-119.

[104] Wei, Z., et al., Analogue electromagnetically induced transparency based on low-loss metamaterial and its application in nanosensor and slow-light device. Plasmonics, 2017. 12(3): p. 641-647.

[105] Pan, W., et al., A terahertz metamaterial based on electromagnetically induced transparency effect and its sensing performance. Optics Communications, 2019. 431: p. 115-119.

[106] Yan, X., et al., The terahertz electromagnetically induced transparency-like metamaterials for sensitive biosensors in the detection of cancer cells. Biosensors and Bioelectronics, 2019. 126: p. 485-492.

[107] Cai, W., et al., A compact graphene metamaterial based on electromagnetically induced transparency effect. Optics Communications, 2020. 475: p. 126266.

[108] Zhu, L., et al., Dual-band electromagnetically induced transparency (EIT) terahertz metamaterial sensor. Optical Materials Express, 2021. 11(7): p. 2109-2121.

[109] Shen, Z.-Y., et al., Electromagnetically induced transparency in novel dual-band metamaterial excited by the toroidal dipolar response. Frontiers of Physics, 2020. 15(1): p. 1-7.

[110] Wang, J., et al., A novel planar metamaterial design for electromagnetically induced transparency and slow light. Optics Express, 2013. 21(21): p. 25159-25166.

[111] Zhu, L., et al., Multi-band slow light metamaterial. Optics express, 2012. 20(4): p. 4494-4502.

[112] Gu, J., et al., Active control of electromagnetically induced transparency analogue in terahertz metamaterials. Nature communications, 2012. 3(1): p. 1-6.

[113] Bai, Q., et al., Tunable slow light in semiconductor metamaterial in a broad terahertz regime. Journal of Applied Physics, 2010. 107(9): p. 093104.

[114] Zhang, K., et al., Dual-mode electromagnetically induced transparency and slow light in a terahertz metamaterial. Optics Letters, 2014. 39(12): p. 3539-3542.

[115] Xu, H., et al., Dual plasmon-induced transparency and slow light effect in monolayer graphene structure with rectangular defects. Journal of Physics D: Applied Physics, 2018. 52(2): p. 025104.

[116] Bisht, S., et al., Study the various feeding techniques of microstrip antenna using design and simulation using CST microwave studio. International Journal of Emerging Technology and Advanced Engineering, 2014. 4(9): p. 318-324.

[117] X. Shen and T. J. Cui, “Photoexcited broadband redshift switch and strength modulation of terahertz metamaterial absorber,” Journal of Optics, vol. 14, no. 11, p. 114012, 2012.

[118] Hangyo, M., M. Tani, and T. Nagashima, Terahertz time-domain spectroscopy of solids: a review. International journal of infrared and millimetre waves, 2005. 26(12): p. 1661-1690.

[119] Fischer, B., et al., Chemical recognition in terahertz time-domain spectroscopy and imaging. Semiconductor Science and Technology, 2005. 20(7): p. S246.

[120] Shen, Y., et al., Generation and detection of ultra-broadband terahertz radiation using photoconductive emitters and receivers. Applied Physics Letters, 2004. 85(2): p. 164-166.

[121] Wu, Q. and X.C. Zhang, Freespace electrooptic sampling of terahertz beams. Applied Physics Letters, 1995. 67(24): p. 3523-3525.

[122] Gallot, G. and D. Grischkowsky, Electro-optic detection of terahertz radiation. JOSA B, 1999. 16(8): p. 1204-1212.

[123] Wu, D., et al., Application of terahertz time domain spectroscopy for NDT of oxide-oxide ceramic matrix composites. Infrared Physics and Technology, 2019. 102: p. 102995.

[124] R. Marqués, F. Medina, and R. Rafii-El-Idrissi, “Role of bianisotropy in negative permeability and left-handed metamaterials,” Phys. Rev. B 65(14), 144440 (2002).

[125] R. Marqués, F. Mesa, J. Martel, and F. Medina, “Comparative analysis of edge- and broadside-coupled split ring resonators for metamaterial design–theory and experiments,” IEEE Trans. Antennas Propag. 51(10), 2572–2581 (2003).

[126] L. Cong, Y. K. Srivastava, and R. Singh, “Inter and intra-metamolecular interaction enabled broadband high-efficiency polarization control in metasurfaces,” Appl. Phys. Lett. 108, 011110 (2016).

[127] L. Cong, Y. K. Srivastava, and R. Singh, “Near-field inductive coupling induced polarization control in metasurfaces,” Adv. Opt. Mater. 4, 848–852 (2016).

[128] D. Roy Chowdhury, R. Singh, A. J. Taylor, H.-T. Chen, and A. K. Azad, “Ultrafast manipulation of near field coupling between bright and dark modes in terahertz metamaterial,” Appl. Phys. Lett. 102, 011122 (2013).

[129] D. R. Chowdhury, A. K. Azad, W. Zhang, and R. Singh, “Near field coupling in passive and active terahertz metamaterial devices,” IEEE Transactions on Terahertz Sci. Technol. 3, 783–790 (2013).

[130] D. Roy Chowdhury, R. Singh, J. F. O’Hara, H.-T. Chen, A. J. Taylor, and A. K. Azad, “Dynamically reconfigurable terahertz metamaterial through photo-doped semiconductor,” Appl. Phys. Lett. 99, 231101 (2011).

[131] D. R. Chowdhury, J. F. O'Hara, A. J. Taylor, and A. K. Azad, "Orthogonally twisted planar concentric split ring resonators towards strong near field coupled terahertz metamaterials," Appl. Phys. Lett. 104, 101105 (2014).

[132] X. Zhao, K. Fan, J. Zhang, G. R. Keiser, G. Duan, R. D. Averitt, and X. Zhang, "Voltage-tunable dual-layer terahertz metamaterials," Microsystems and Nanoeng. 2, 16025 (2016).

[133] Imbert, C., Calculation and experimental proof of the transverse shift induced by total internal reflection of a circularly polarized light beam. Physical Review D, 1972. 5(4): p. 787.

[134] Jullien, A., et al., Nonlinear polarization rotation of elliptical light in cubic crystals, with application to cross-polarized wave generation. JOSA B, 2005. 22(12): p. 2635-2641.

[135] García-Martín, A., G. Armelles, and S. Pereira, Light transport in photonic crystals composed of magneto-optically active materials. Physical Review B, 2005. 71(20): p. 205116.

[136] Zhou, Z. and H. Yang, Triple-band asymmetric transmission of linear polarization with deformed S-shape bilayer chiral metamaterial. Applied Physics A, 2015. 119(1): p. 115-119.

[137] Xiao, Z.-y., et al., Multi-band transmissions of chiral metamaterials based on Fabry-Perot like resonators. Optics express, 2015. 23(6): p. 7053-7061.

[138] Xia, R., et al., Broadband terahertz half-wave plate based on anisotropic polarization conversion metamaterials. Optical Materials Express, 2017. 7(3): p. 977-988.

[139] Kindness, S.J., et al., Graphene-integrated metamaterial device for all-electrical polarization control of terahertz quantum cascade lasers. ACS Photonics, 2019. 6(6): p. 1547-1555.

[140] J.-B. Masson and G. Gallot, "Terahertz achromatic quarter-wave plate," Optics letters, vol. 31, no. 2, pp. 265–267, 2006.

[141] Y. Cheng, R. Gong, and L. Wu, "Ultra-broadband linear polarization conversion via diode-like asymmetric transmission with composite metamaterial for terahertz waves," Plasmonics, vol. 12, no. 4, pp. 1113–1120, 2017.

[142] Sen Hu, Helin Yang, Song Han, Xiaojun Huang, and Boxun Xiao. Journal of Applied Physics, 117(4):043107, 2015.

[143] Koijam Monika Devi, Dibakar Roy Chowdhury, Gagan Kumar, and Amarendra K Sarma. Journal of Applied Physics, 124(6):063106, 2018.

[144] Muhammad Amin, Rashad Ramzan, and Omar Siddiqui. Slow wave applications of electromagnetically induced transparency in microstrip resonator. Scientific reports, 8(1):2357, 2018.

[145] Chao Tang, Qingshan Niu, Ben-Xin Wang, and Wei-Qing Huang. Plasmonics, pages 1-6, 2018.

[146] XJ He, L Wang, JM Wang, XH Tian, JX Jiang, and ZX Geng. Journal of physics D: Applied Physics, 46(36):365302, 2013.

[147] Tingting Liu, Huaixing Wang, Yong Liu, Longsheng Xiao, Chaobiao Zhou, Yuebo Liu, Chen Xu, and Shuyuan Xiao. Journal of Physics D: Applied Physics, 51(41):415105, 2018.

[148] Ozgur Demirkap, Fulya Bagci, A Egemen Yilmaz, and Baris Akaoglu. Advanced Electromagnetics, 8(2):63-70, 2019.

[149] Zhengyang Bai, Chao Hang, and Guoxiang Huang. Optics Communications, 291:25-258, 2013.

[150] Kejian Chen, Yiqi Wang, Jingjing Liu, Yang Bai, Ting Bu, Bin Cai, Yiming Zhu, and Songlin Zhuang. Optics Communications, 363:69-73, 2016.

[151] Xun-jun He, Jian-min Wang, Xiao-hua Tian, Jiu-xing Jiang, and Zhao-xin Geng. Optics Communications, 291:371-375, 2013.

[152] Ningning Xu, Manukumara Manjappa, Ranjan Singh, and Weili Zhang. Advanced Optical Materials, 4(8):1179-1185, 2016.

[153] Papasimakis N, Zheludev NI. Metamaterial-induced transparency: sharp Fano resonances and slow light. Optics and Photonics News 2009;20:22-7.

[154] Wu C, Khanikaev AB, Shvets G. Broadband slow light metamaterial based on a double-continuum Fano resonance. Physical review letters 2011;106:107403.

[155] Zhu L, Meng F-Y, Fu J-H, Wu Q, Hua J. Multi-band slow light metamaterial. Optics express 2012;20:4494-502.

[156] Wang J, Yuan B, Fan C, He J, Ding P, Xue Q, et al. A novel planar metamaterial design for electromagnetically induced transparency and slow light. Optics express 2013;21:25159-66.

[157] Bai. et al. Classical analogs of double electromagnetically induced transparency. Optics Communications 291, 253–258 (2013).

[158] Zhang, Y., et al., Graphene based tunable metamaterial absorber and polarization modulation in terahertz frequency. Optics express, 2014. 22(19): p. 22743-22752.